

Springer Handbook of Metrology and Testing

Horst Czichos, Tetsuya Saito, Leslie Smith (Eds.)

2nd edition
1017 Figures and 177 Tables

 Springer

7.3	Hardness	366
7.4	Strength	388
7.5	Fracture Mechanics.....	408
7.6	Permeation and Diffusion	426
	References	442
8	Thermal Properties	
	<i>Wolfgang Buck, Steffen Rudtsch</i>	453
8.1	Thermal Conductivity and Specific Heat Capacity	454
8.2	Enthalpy of Phase Transition, Adsorption and Mixing.....	462
8.3	Thermal Expansion and Thermomechanical Analysis	469
8.4	Thermogravimetry	471
8.5	Temperature Sensors	471
	References	482
9	Electrical Properties	
	<i>Bernd Schumacher, Heinz-Gunter Bach, Petra Spitzer, Jan Obrzut, Steffen Seitz</i>	485
9.1	Electrical Materials	486
9.2	Electrical Conductivity of Metallic Materials.....	493
9.3	Electrolytic Conductivity	498
9.4	Semiconductors.....	507
9.5	Measurement of Dielectric Materials Properties	526
	References	537
10	Magnetic Properties	
	<i>Joachim Wecker, Günther Bayreuther, Gunnar Ross, Roland Grössinger</i>	541
10.1	Magnetic Materials	542
10.2	Soft and Hard Magnetic Materials: (Standard) Measurement Techniques for Properties Related to the $B(H)$ Loop	546
10.3	Magnetic Characterization in a Pulsed Field Magnetometer (PFM)	567
10.4	Properties of Magnetic Thin Films.....	579
	References	585
11	Optical Properties	
	<i>Tadashi Itoh, Tsutomu Araki, Masaaki Ashida, Tetsuo Iwata, Kiyofumi Muro, Noboru Yamada</i>	587
11.1	Fundamentals of Optical Spectroscopy	588
11.2	Microspectroscopy	605
11.3	Magneto-optical Measurement.....	609
11.4	Nonlinear Optics and Ultrashort Pulsed Laser Application	614
11.5	Fiber Optics	626
11.6	Evaluation Technologies for Optical Disk Memory Materials.....	641
11.7	Optical Sensing	649
	References	656

9. Electrical Properties

Electronic materials – conductors, insulators, semiconductors – play an important role in today's technology. They constitute *electrical and electronic devices*, such as radio, television, telephone, electric light, electromotors, computers, etc. From a materials science point of view, the electrical properties of materials characterize two basic processes: electrical energy conduction (and dissipation) and electrical energy storage.

- Electrical conductivity describes the ability of a material to transport charge through the process of conduction, normalized by geometry. Electrical dissipation comes as the result of charge transport or conduction. Dissipation or energy loss results from the conversion of electrical energy to thermal energy (Joule heating) through momentum transfer during collisions as the charges move.
- Electrical storage is the result of charge storing energy. This process is dielectric polarization, normalized by geometry to be the material property called dielectric permittivity. As polarization occurs and causes charges to move, the charge motion is also dissipative.

In this chapter, the main methods to characterize the electrical properties of materials are compiled. Sections 9.2 to 9.5 describe the measuring methods under the following headings

- Electrical conductivity of metallic materials
- Electrolytical conductivity
- Semiconductors
- Dielectrics.

As an introductory overview, in Sect. 9.1 the basic categories of electrical materials are outlined in adopting the classification and terminology of the chapter *Electronic Properties of Materials of Understanding Materials Science* by Hummel [9.1].

9.1	Electrical Materials	486
9.1.1	Conductivity and Resistivity of Metals	486
9.1.2	Superconductivity	487
9.1.3	Semiconductors	488
9.1.4	Conduction in Polymers	490
9.1.5	Ionic Conductors	490
9.1.6	Dielectricity	491
9.1.7	Ferroelectricity and Piezoelectricity	492
9.2	Electrical Conductivity of Metallic Materials	493
9.2.1	Scale of Electrical Conductivity; Reference Materials	493
9.2.2	Principal Methods	494
9.2.3	DC Conductivity, Calibration of Reference Materials	496
9.2.4	AC Conductivity, Calibration of Reference Materials	496
9.2.5	Superconductivity	497
9.3	Electrolytic Conductivity	498
9.3.1	Scale of Conductivity	498
9.3.2	Basic Principles	499
9.3.3	The Measurement of the Electrolytic Conductivity	501
9.4	Semiconductors	507
9.4.1	Conductivity Measurements	507
9.4.2	Mobility Measurements	510
9.4.3	Dopant and Carrier Concentration Measurements	513
9.4.4	I–V Breakdown Mechanisms	518
9.4.5	Deep Level Characterization and Minority Carrier Lifetime	519
9.4.6	Contact Resistances of Metal–Semiconductor Contacts ...	523
9.5	Measurement of Dielectric Materials Properties	526
9.5.1	Dielectric Permittivity	527
9.5.2	Measurement of Permittivity	529
9.5.3	Measurement of Permittivity Using Microwave Network Analysis ..	532
9.5.4	Uncertainty Considerations	536
9.5.5	Conclusion	537
	References	537

9.1 Electrical Materials

One of the principal characteristics of materials is their ability (or lack of ability) to conduct electrical current. According to their conductivity σ they are divided into conductors, semiconductors, and insulators (dielectrics). The inverse of the conductivity is called resistivity ρ that is $\rho = 1/\sigma$. The resistance R of a piece of conducting material is proportional to its resistivity and to its length L and is inversely proportional to its cross-sectional area A : $R = L\rho/A$. To measure the electrical resistance, a direct current is applied to a slab of the material. The current I through the sample (in ampere), as well as the voltage drop V on two potential probes (in volt) is recorded as depicted in Fig. 9.1.

The resistance (in ohm) can then be calculated by making use of Ohm's law $V = RI$. Another form of Ohm's law $j = \sigma E$ links current density $j = I/A$, that is, the current per unit area (A/cm^2), with the conductivity σ ($\Omega^{-1}cm^{-1}$ or siemens per centimeter) and the electric field strength $E = V/L$ (V/cm).

The conductivity σ of different materials at room temperature spans more than 25 orders of magnitude as depicted in Fig. 9.2. Moreover, if one takes the conductivity of superconductors, measured at low temperatures, into consideration, this span extends to 40 orders of magnitude (using an estimated conductivity for superconductors of about $10^{20} \Omega^{-1}cm^{-1}$). This is the largest known variation in a physical property.

9.1.1 Conductivity and Resistivity of Metals

For metallic materials it is postulated that they contain *free electrons* which are accelerated under the influence of an electric field maintained, for example, by a battery. The drifting electrons can be considered, in a preliminary, classical description, to occasionally collide (that is, electrostatically interact) with certain lattice atoms, thus losing some of their energy. This constitutes the electrical resistance.

Semiconductors or insulators which have only a small number of free electrons (or often none at all) display only very small conductivities. The small number of electrons results from the strong binding forces between electrons and atoms that are common for insulators and semiconductors. Conversely, metals which contain a large number of free electrons have a large conductivity. Further, the conductivity is large when the average time between two collisions τ is large. Obviously, the number of collisions decreases (i. e.,

τ increases) with decreasing temperature and decreasing number of imperfections. The simple *free electron model* describes the electrical behavior of many materials reasonably well.

Electron Band Model

Electrons of isolated atoms (for example in a gas) can be considered to orbit at various distances about their nuclei. These orbits constitute different energies. Specifically, the larger the radius of an orbit, the larger the excitation energy of the electron. This fact is often represented in a somewhat different fashion by stating that the electrons are distributed on different energy levels, as schematically shown in Fig. 9.3.

These distinct energy levels, which are characteristic for isolated atoms, widen into energy bands when atoms approach each other and eventually form a solid as depicted on the left-hand side of Fig. 9.3. Quantum mechanics postulates that the electrons can only reside within these bands, but not in the areas outside of them. The allowed energy bands may be noticeably separated from each other. In other cases, depending on the material and the energy, they may partially or completely overlap. In short, each material has its distinct electron energy band structure. Characteristic band structures for the main classes of materials are schematically depicted in Fig. 9.4.

The band structures shown in Fig. 9.4 are somewhat simplified. Specifically, band schemes actually possess a fine structure, that is, the individual energy states

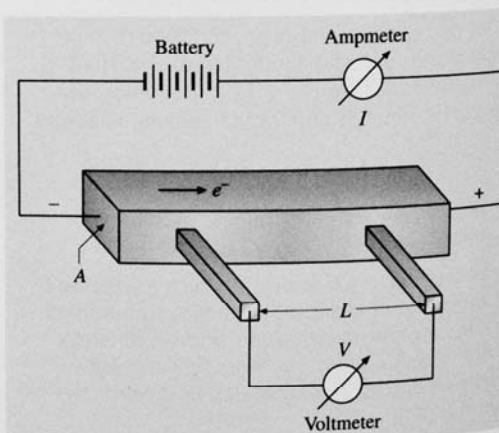


Fig. 9.1 Principle of the measurement of the resistance of a conductor

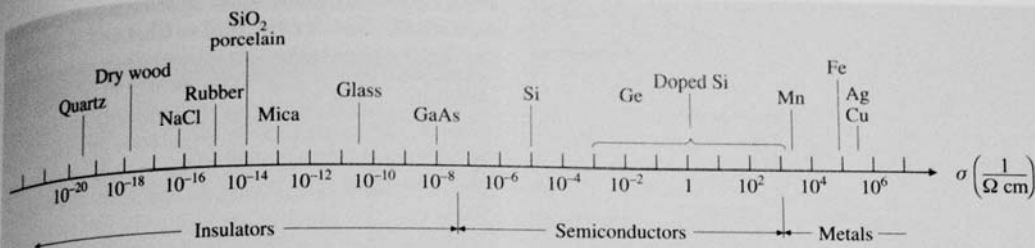


Fig. 9.2 Conductivity scale of materials

(i.e., the possibilities for electron occupation) are often denser in the center of a band (Fig. 9.5).

Some of the bands are occupied by electrons while others remain partially or completely unfilled. The degree to which an electron band is filled by electrons is indicated in Fig. 9.4 by shading. The highest level of electron filling within a band is called the Fermi energy E_F . Some materials, such as insulators and semiconductors, have completely filled electron bands. (They differ, however, in their distance to the next higher band.) Metals, on the other hand, are characterized by partially filled electron bands. The amount of filling depends on the material, that is, on the electron concentration and the amount of band overlap.

According to quantum theory, first only those materials that possess partially filled electron bands are capable of conducting an electric current. Electrons can then be lifted slightly above the Fermi energy into an allowed and unfilled energy state. This permits them to be accelerated by an electric field, thus producing a current. Second, only those electrons that are close to the Fermi energy participate in the electric conduction. Third, the number of electrons near the Fermi energy depends on the density of available electron states (Fig. 9.5). The conductivity in quantum mechanical terms yields the following equation: $\sigma = 1/3 e^2 v_F^2 \tau N(E_F)$, where v_F is the velocity of the electrons at the Fermi energy (called the Fermi velocity) and $\tau N(E_F)$ is the density of filled electron states (called the population density) at the Fermi energy. Monovalent metals (such as copper, silver, and gold) have partially filled bands, as shown in Fig. 9.4. Their electron population density near the Fermi energy is high which results in a large conductivity. Bivalent metals, on the other hand, are distinguished by overlapping upper bands and by a small electron concentration near the bottom of the valence band. As a consequence, the electron population near the Fermi energy is small which leads to a comparatively low conductivity. For alloys, the residual resistivity increases with increasing amount of

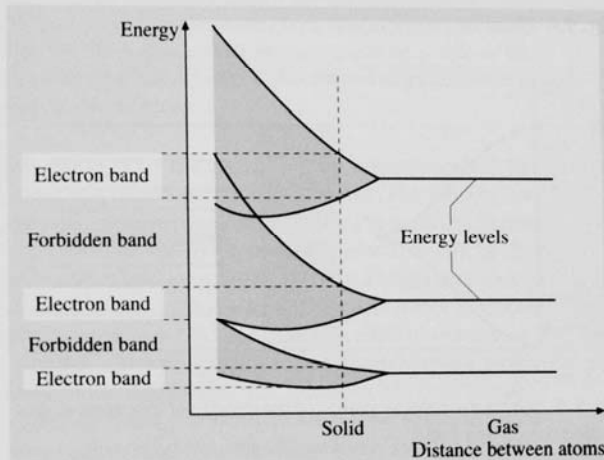


Fig. 9.3 Schematic representation of electron energy levels in materials

solute content. Finally, insulators have completely filled (and completely empty) electron bands which results in a virtually zero population density as shown in Fig. 9.4. Thus, the conductivity in insulators is virtually zero.

9.1.2 Superconductivity

The resistivity in superconductors becomes immeasurably small or virtually zero below a critical temperature T_c . About 27 elements, numerous alloys, ceramic materials (containing copper oxide), and organic compounds (based, e.g., on selenium or sulfur) have been found to possess this property (Table 9.1).

It is estimated that the conductivity of superconductors below T_c is about $10^{20} \Omega^{-1} \text{cm}^{-1}$. The transition temperatures where superconductivity starts range from 0.01 K (for tungsten) up to about 125 K (for ceramic superconductors). Of particular interest are materials with T_c above 77 K, that is, the boiling point of liquid nitro-

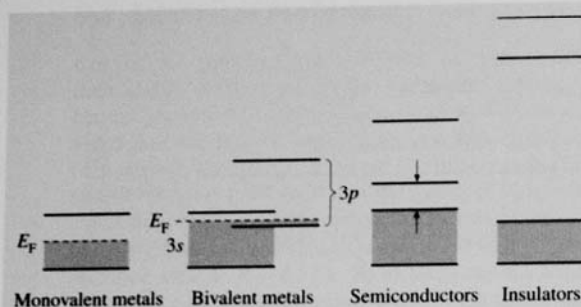


Fig. 9.4 Electronic energy-band representation

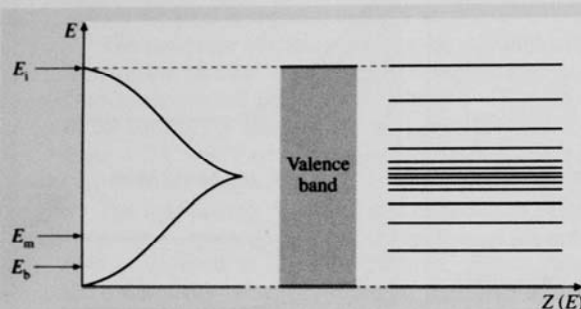


Fig. 9.5 Schematic representation of the density of electrons within an electron energy band

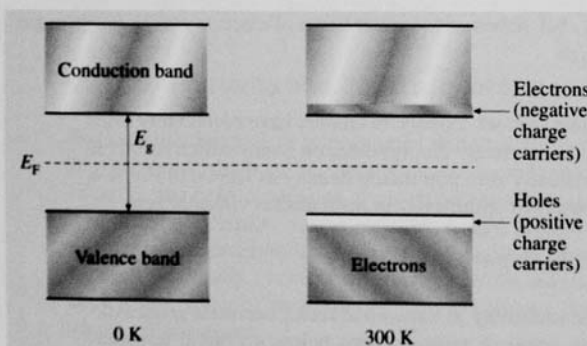


Fig. 9.6 Simplified band diagrams for an intrinsic semiconductor

gen which is more readily available than other coolants. Among the so-called high- T_c superconductors are the 1-2-3 compounds such as $\text{YBa}_2\text{Cu}_3\text{O}_{7-x}$, where molar ratios of rare earth to alkaline earth to copper relate as 1 : 2 : 3. Their transition temperatures range from 40 to 134 K. Ceramic superconductors have an orthorhombic, layered, perovskite crystal structure which contains

Table 9.1 Critical temperatures of some superconducting materials (R = Gd, Dy, Ho, Er, Tm, Yb, Lu)

Materials	T_c (K)
Tungsten	0.01
Mercury	4.15
Sulfur-based organic superconductor	8
Nb_3Sn and Nb-Ti	9
V_3Si	17.1
Nb_3Ge	23.2
La-Ba-Cu-O	40
$\text{YBa}_2\text{Cu}_3\text{O}_{7-x}$	≈ 92
$\text{RBa}_2\text{Cu}_3\text{O}_{7-x}$	≈ 92
$\text{Bi}_2\text{Sr}_2\text{Ca}_2\text{Cu}_3\text{O}_{10+\delta}$	113
$\text{Ti}_2\text{CaBa}_2\text{Cu}_2\text{O}_{10+\delta}$	125
$\text{HgBa}_2\text{Ca}_2\text{Cu}_3\text{O}_{8+\delta}$	134

two-dimensional sheets and periodic oxygen vacancies. (The superconductivity exists only parallel to these layers, that is, it is anisotropic.) The first superconducting material was found by Kammerlingh Onnes in 1911 in mercury which has a T_c of 4.15 K. Methods to measure superconductivity are described in Sect. 9.2.5.

9.1.3 Semiconductors

The electrical properties of semiconductors are commonly explained by making use of the electron band structure model which is the result of quantum-mechanical considerations. In simple terms, the electrons are depicted to reside in certain allowed energy regions.

Figure 9.6 depicts two electron bands, the lower of which, at 0 K, is completely filled with valence electrons. This band is appropriately called the valence band. It is separated by a small gap (about 1.1 eV for Si) from the conduction band which contains no electrons at 0 K. Further, quantum mechanics stipulates that electrons essentially are not allowed to reside in the gap between these bands (called the forbidden band). Since the filled valence band possesses no allowed empty energy states in which the electrons can be thermally excited (and then accelerated in an electric field), and since the conduction band contains no electrons at all, silicon is an insulator at 0 K. The situation changes decisively once the temperature is raised. In this case, some electrons may be thermally excited across the band gap and thus populate the conduction band (Fig. 9.6). The number of these electrons is extremely small for statistical reasons. Specifically, about one out of every 10^{13} atoms contributes an electron at room temperature. Nev-

ertheless, this number is large enough to cause some conduction. The number of electrons in the conduction band N_e increases exponentially with temperature T but also depends, of course, on the size of the gap energy. The conductivity depends naturally on the number of these electrons but also on their mobility. The latter is defined to be the velocity v per unit electric field E that is $\mu = v/E$. All taken, the conductivity is $\sigma = N_e \mu e$, where e is the charge of an electron. The mobility of electrons is substantially impaired by interactions with impurity atoms and other lattice imperfections (as well as with vibrating lattice atoms). It is for this reason that silicon has to be extremely pure and free of grain boundaries which requires sophisticated and expensive manufacturing processes called zone refining or Czochralski crucible pulling.

The conductivity for semiconductors increases with rising temperature. This is in marked contrast to metals and alloys, for which the conductivity decreases with temperature. The thermal excitation of some electrons across the band gap has another important consequence. The electrons that have left the valence band leave behind some empty spaces which allow additional conduction to take place in the valence band. The empty spaces are called defect electrons or electron holes. These holes may be considered to be positively charged carriers similarly as electrons are defined to be negatively charged carriers. In essence, at elevated temperatures, the thermal energy causes some electrons to be excited from the valence band into the conduction band. They provide there some conduction. The electron holes which have been left behind in the valence band cause a hole current which is directed in the opposite direction compared to the electron current. The total conductivity, therefore, is a sum of both contributions $\sigma = N_e \mu_e e + N_h \mu_h e$, where the subscripts e and h refer to electrons and holes, respectively. The process is called intrinsic conduction and the material involved is termed an intrinsic semiconductor since no foreign elements are involved. The Fermi energy of intrinsic semiconductors can be considered to be the average of the electron and the hole Fermi energies and is therefore situated near the center of the gap as depicted in Fig. 9.6.

The number of electrons in the conduction band can be considerably increased by adding, for example, to silicon small amounts of group-V elements called donor atoms. Dopants such as phosphorous or arsenic are commonly utilized which are added in amounts of, for example, 0.0001%. These dopants replace some regular lattice atoms in a substitutional manner (Fig. 9.7). Since phosphorous has five valence electrons, that is,

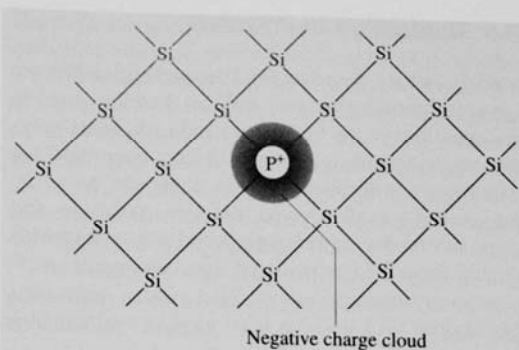


Fig. 9.7 Two-dimensional representation of a silicon lattice (covalent bonds) with a phosphorus atom substituting a regular lattice atom

one more than silicon, the extra electron called the donor electron is only loosely bound. The binding energy of phosphorous donor electrons in a silicon matrix is about 0.045 eV. Thus, the donor electrons can be dissociated from their nuclei by only a slight increase in thermal energy. At room temperature all donor electrons have already been excited into the conduction band.

Near room temperature, only the majority carriers need to be considered. For example, at room temperature, all donor electrons in an n-type semiconductor have been excited from the donor levels into the conduction band. At higher temperatures, however, intrinsic effects may considerably contribute to the conduction. Compounds made of group-III and group-V elements, such as gallium arsenide, have similar semiconducting properties as the group-IV materials silicon or germanium. GaAs is of some technical interest because of its above-mentioned wider band gap and because of its larger electron mobility which aids in high-speed applications. Further, the ionization energies of donor and acceptor impurities in GaAs are one order of magnitude smaller than in silicon which ensures complete electron (and hole) transfer from the donor (acceptor) levels into the conduction (valence) bands even at relatively low temperatures. However, GaAs is about ten times more expensive than Si and its heat conduction is smaller. Other compound semiconductors include II-VI combinations such as ZnO, ZnS, ZnSe, or CdTe, and IV-VI materials such as PbS, PbSe, or PbTe. Silicon carbide, a IV-IV compound, has a band gap of 3 eV and can thus be used up to 700 °C before intrinsic effects set in. The most important application of compound semiconductors is, however, for optoelectronic purposes (e.g. for light-emitting diodes and lasers).

9.1.4 Conduction in Polymers

Materials that are electrical (and thermal) insulators are of great technical importance and are, therefore, used in large quantities in the electronics industry. Most polymeric materials are insulating and have been used for this purpose for decades. It came, therefore, as a surprise when it was discovered that some polymers and organic substances may have electrical properties which resemble those of conventional semiconductors, metals, or even superconductors. Historically, transoidal polyacetylene (Fig. 9.8) has been used as a conducting polymer.

It represents what is called a conjugated organic polymer, that is, it has alternating single and double bonds between the carbon atoms. It is obtained as a silvery, flexible, and lightweight film which has a conductivity comparable to that of silicon. Its conductivity increases with increasing temperature similarly as in semiconductors. The conductivity of trans-polyacetylene can be made to increase by up to seven orders of magnitude by doping it with arsenic pentafluoride, iodine, or bromine, which yields a p-type semiconductor. Thus, σ approaches the lower end of the conductivity of metals as shown in Fig. 9.9.

Among other dopants are *n*-dodecyl sulfonate (soap). However, the stability of this material is very poor; it deteriorates in hours or days. This very drawback which it shares with many other conducting polymers nevertheless can be profitably utilized in special devices such as remote gas sensors, biosensors, and other remotely readable indicators which detect changes in humidity, radiation dosage, mechanical abuse, or chemical release. Other conducting polymers include polypyrrole and polyaniline. The latter has a reasonably good conductivity and a high environmental stability. It has been used for electronic devices such as field-effect transistors, electrochromic displays, as well as for rechargeable batteries.

In order to better understand the electronic properties of polymers by means of the electron theory

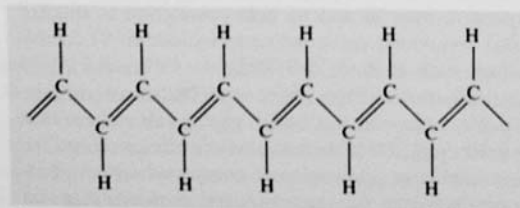


Fig. 9.8 Transoidal isomer of polyacetylene

and the band structure concept, one needs to know the degree of order or the degree of periodicity of the atoms because only ordered and strongly interacting atoms or molecules lead to distinct and wide electron bands. It has been observed that the degree of order in polymers depends on the regularity of the molecular structure. One of the electrons in the double bond of a conjugated polymer can be considered to be only loosely bound to the neighboring carbon atoms. Thus, this electron can be easily disassociated from its carbon atom by a relatively small energy which may be provided by thermal energy. The delocalized electrons behave like free electrons and may be accelerated as usual in an electric field. It should be noted in closing that the interpretation of conducting polymers is still in flux and future research needs to clarify certain points.

9.1.5 Ionic Conductors

Electrical conduction in ionically bonded materials, such as the alkali-halides, is extremely small. The reason for this is that the atoms in these chemical com-

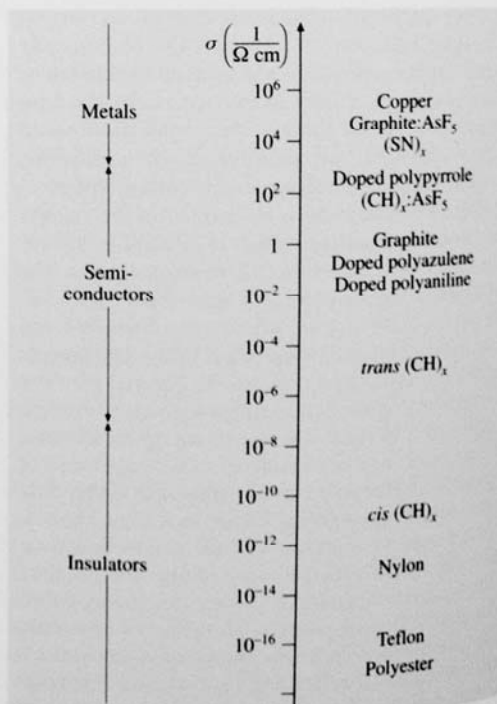


Fig. 9.9 Conductivity of various polymeric materials

pounds strive to assume the noble gas configuration for maximal stability and thus transfer electrons between each other to form positively charged cations and negatively charged anions. The binding forces between the ions are electrostatic in nature, that is, they are very strong. Essentially no free electrons are therefore formed. As a consequence, the room temperature conductivity in ionic crystals is about 22 orders of magnitude smaller than that of typical metallic conductors (Fig. 9.2). The wide band gap in insulators allows only extremely few electrons to become excited from the valence into the conduction band (Fig. 9.4 right).

The main contribution to the electrical conduction in ionic crystals (as little as it may be) is due to ionic conduction. Ionic conduction is caused by the movement of some negatively (or positively) charged ions which hop from lattice site to lattice site under the influence of an electric field. The ionic conductivity $\sigma_{\text{ion}} = N_{\text{ion}} e \mu_{\text{ion}}$ is the product of three quantities. In the present case, N_{ion} is the number of ions per unit volume which can change their position under the influence of an electric field whereas μ_{ion} is the mobility of these ions. In order for ions to move through a crystalline solid they must have sufficient energy to pass over an energy barrier. Further, an equivalent lattice site next to a given ion must be empty in order for an ion to be able to change its position. Thus, N_{ion} depends on the vacancy concentration in the crystal (i.e., on the number of Schottky defects).

In short, the theory of ionic conduction contains essential elements of diffusion theory. Diffusion theory links the mobility of the ions with the diffusion coefficient D through the Einstein relation $\mu_{\text{ion}} = De/(k_B T)$.

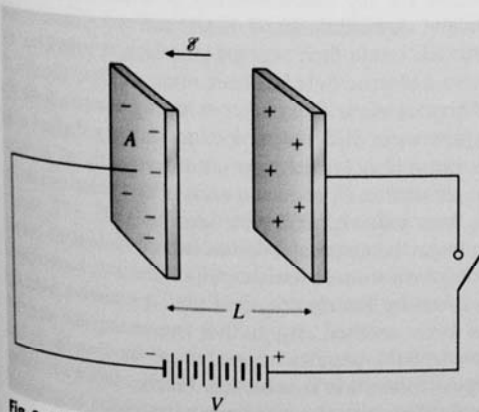


Fig. 9.10 Principle of storing electric energy in a dielectric capacitor

The diffusion coefficient varies with temperature by an Arrhenius equation $D = D_0 \exp[-Q/(k_B T)]$, where Q is the activation energy for the process under consideration and D_0 is a preexponential factor which depends on the vibrational frequency of the atoms and some structural parameters. Combining the equations yields $\sigma_{\text{ion}} = [N_{\text{ion}} e^2 D_0 / (k_B T)] \exp[Q/(k_B T)]$. This equation is shortened by combining the preexponential constants into σ_0 : $\sigma_{\text{ion}} = \sigma_0 \exp[Q/(k_B T)]$.

In summary, the ionic conduction increases exponentially with increasing temperature (as in semiconductors). Further, σ_{ion} depends on a few other parameters such as the number of ions that can change their position, the vacancy concentration, as well as on an activation energy.

9.1.6 Dielectricity

Dielectric materials, that is, insulators, possess a number of important electrical properties which make them useful in the electronics industry.

When a voltage is momentarily applied to two parallel metal plates which are separated by a distance L as shown in Fig. 9.10, the resulting electric charge essentially remains on these plates even after the voltage has been removed (at least as long as the air is dry).

This ability to store an electric charge is called the capacitance C which is defined to be the charge q per applied voltage V that is $C = q/V$, where C is given in coulombs per volt or farad. The capacitance is higher, the larger the area A of the plates and the smaller the dis-

Table 9.2 DC dielectric constants of some materials

Barium titanate	4000	Ferroelectric
Water	81.1	Dielectric
Acetone	20	
Silicon	11.8	
GaAs	10.9	
Marble	8.5	
Soda-lime-glass	6.9	
Porcelain	6.0	
Epoxy	4.0	
Fused silica	4.0	
Nylon 6.6	4.0	
PVC	3.5	
Ice	3.0	
Amber	2.8	
Polyethylene	2.3	
Paraffin	2.0	
Air	1.000576	

tance L between them. Further, the capacitance depends on the material that may have been inserted between the plates. The experimental observations lead to $C = \epsilon \epsilon_0 (A/L)$, where $\epsilon = C/C_{\text{vac}}$ determines the magnitude of the added storage capability. It is called the (unitless) dielectric constant (or occasionally the relative permittivity ϵ_r). ϵ_0 is a universal constant having the value of $8.85 \times 10^{-12} \text{ F/m}$ (farad per meter) or As/(Vm) and is known by the name permittivity of empty space (or of vacuum).

Some values for the dielectric constant are given in Table 9.2. The dielectric constant of empty space is set to be 1 whereas ϵ of air and many other gases is nearly 1.

The capacitance increases when a piece of a dielectric material is inserted between two conductors. Under the influence of an external electric field, the negatively charged electron cloud of an atom becomes displaced with respect to its positively charged core. As a result, a dipole is created which has an electric dipole moment $p = qx$, where x is the separation between the positive and the negative charge. (The dipole moment is generally a vector pointing from the negative to the positive charge.) The process of dipole formation (or alignment of already existing dipoles) under the influence of an external electric field that has an electric field strength E , is called polarization. Dipole formation of all involved atoms within a dielectric material causes a charge redistribution so that the surface which is nearest to the positive capacitor plate is negatively charged. As a consequence, electric field lines within a dielectric are created which are opposite in direction to the external field lines. Effectively, the electric field lines within a dielectric material are weakened due to polarization. The electric field strength $E = V/L = E_{\text{vac}}/\epsilon$ is reduced by inserting a dielectric between two capacitor plates. Within a dielectric material the electric field strength E is replaced by the dielectric displacement D (also called the surface charge density), that is, $D = \epsilon \epsilon_0 E = q/A$. The dielectric displacement is the superposition of two terms: $D = \epsilon_0 E + P$, where P is called the dielectric polarization, that is, the induced electric dipole moment per unit volume. The units for D and P are C/m^2 . The polarization is responsible for the increase in charge density (q/A) above that for vacuum.

The mechanism just described is known as electronic polarization. It occurs in all dielectric materials that are subjected to an electric field. In ionic materials, such as the alkali halides, an additional process may occur which is called ionic polarization. In short, cations and anions are somewhat displaced from their equilib-

rium positions under the influence of an external field and thus give rise to a net dipole moment. Finally, many materials already possess permanent dipoles which can be aligned in an external electric field. Among them are water, oils, organic liquids, waxes, amorphous polymers, polyvinylchloride, and certain ceramics such as barium titanate (BaTiO_3). This mechanism is termed orientation polarization or molecular polarization. All three polarization processes are additive if applicable.

Most capacitors are used in electric circuits involving alternating currents. This requires the dipoles to reorient quickly under a rapidly changing electric field. Not all polarization mechanisms respond equally quick to an alternating electric field. For example, many molecules are relatively sluggish in reorientation. Thus, molecular polarization breaks down already at relatively low frequencies. In contrast, electronic polarization responds quite rapidly to an alternating electric field even at frequencies up to 10^{16} Hz . At certain frequencies a substantial amount of the excitation energy is absorbed and transferred into heat. This process is called dielectric loss. It is imperative to know the frequency for dielectric losses for a given material so that the device is not operated in this range.

9.1.7 Ferroelectricity and Piezoelectricity

Ferroelectricity is the electric analogue to ferromagnetism (Chap. 10). Ferroelectric materials, such as barium titanate, exhibit spontaneous polarization without the presence of an external electric field. Their dielectric constants are orders of magnitude larger than those of dielectrics (Table 9.2). Thus, they are quite suitable for the manufacturing of small-sized, highly efficient capacitors. Most of all, however, ferroelectric materials retain their state of polarization even after an external electric field has been removed. Specifically, if a ferroelectric is exposed to a strong electric field E , its permanent dipoles become increasingly aligned with the external field direction until eventually all dipoles are parallel to E , and saturation of the polarization P_s has been achieved as depicted in Fig. 9.11.

Once the external field has been withdrawn a remanent polarization P_r remains which can only be removed by inverting the electric field until a coercive field E_c has been reached. By further increasing the reverse electric field, parallel orientation of the dipoles in the opposite direction is achieved. Finally, when reversing the field once more, a complete hysteresis loop is obtained as depicted in Fig. 9.11. Therefore, ferroelectrics can be utilized for memory devices in computers, etc.

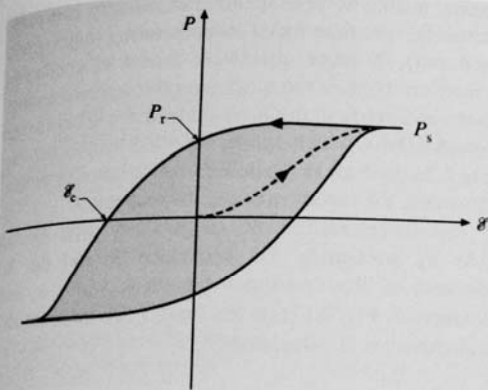


Fig. 9.11 Schematic representation of a hysteresis loop for a ferroelectric material in an electric field

The area within a hysteresis loop is proportional to the energy per unit volume that is dissipated once a full field cycle has been completed.

A critical temperature, called the Curie temperature, exists above which the ferroelectric effects are destroyed and the material becomes dielectric. Typical Curie temperatures range from -200°C for strontium titanate to at least 640°C for NaNbO_3 . By heating BaTiO_3 above its Curie temperature (120°C), the tetragonal unit cell transforms to a cubic cell whereby the ions now assume symmetric positions. Thus, no

spontaneous alignment of dipoles remains and BaTiO_3 becomes dielectric.

If pressure is applied to a ferroelectric material such as BaTiO_3 , a change in the polarization may occur which results in a small voltage across the sample. Specifically, the slight change dimensions causes a variation in bond lengths between cations and anions. This effect is called piezoelectricity. It is found in a number of materials such as quartz (however, much weaker than in BaTiO_3), in ZnO , and in complicated ceramic compounds such as PbZrTiO_6 . Piezoelectricity is utilized in devices that are designed to convert mechanical strain into electricity. Those devices are called transducers. Applications include strain gages, microphones, sonar detectors, and phonograph pickups, to mention a few.

The inverse mechanism, in which an electric field produces a change in dimensions in a ferroelectric material, is called electrostriction. An earphone utilizes such a device. Probably the most important application, however, is the quartz crystal resonator which is used in electronic devices as a frequency selective element. Specifically, a periodic strain is exerted to a quartz crystal by an alternating electric field which excites this crystal to vibrations. These vibrations are monitored in turn by piezoelectricity. If the applied frequency coincides with the natural resonance frequency of the molecules, then amplification occurs. In this way, very distinct frequencies are produced which are utilized for clocks or radio frequency signals.

9.2 Electrical Conductivity of Metallic Materials

9.2.1 Scale of Electrical Conductivity; Reference Materials

Precise measurements of the electrical conductivity date back to the end of the 19th century. With the development of the electrical industry it became important to check the quality of the copper used in electrical machines. The Physikalisch-Technische Reichsanstalt in Berlin, Germany, for instance, was strongly supported by Werner von Siemens, head of the Siemens company. Nowadays, copper is still an important part where conductivity measurements are applied. Furthermore, the aircraft manufacturing industry uses conductivity measurements for the quality assurance of aluminum alloys. Recently, it became also important for the coin manufacturing industry. With the introduction of the Euro, these coins are produced all over Europe, but have to

meet strong criteria in conductivity, on the one hand to protect the consumers from fraud, on the other hand for the acceptance of coins in vending machines.

Conductivity is usually measured in the unit MS/m , or $\mu\Omega \text{ m}$. In practice, the values are commonly given in so-called % IACS, which stands for *Percent International Annealed Copper Standard*. This standard is a hypothetical copper bar of 1 m in length and 1 mm^2 in area having a resistance of $1/58 \Omega$.

Typical values for some metals and alloys are listed in Table 9.3. Generally there are three main areas for conductivity measurements, conductors (copper) at 100% IACS, aluminum alloys at 50% IACS and alloys for coins at 10% IACS. Instruments for the measurement of conductivity operate either with direct current methods (DC) or alternating current methods (AC). The DC methods usually is a voltage-current method,

Table 9.3 Typical values for the conductivity of metals and alloys

Metal/alloy	Conductivity at 20 °C	
	(MS/m)	(% IACS)
Copper (soft)	59.9	103.3
Copper (annealed)	58	100.0
Aluminum (soft)	35.7	61.6
E-AlMgSi (Aldrey)	30.0	51.7
Brass (CuZn40)	15.0	25.9
Bronze (CuSn6)	9.1	15.7
Titanium	2.4	4.1

whereas the AC methods make use of the eddy current principle. Details are described in Sect. 9.2.2 and for the calibration of reference standards in Sects. 9.2.3 and 9.2.4.

For precise measurements of conductivity reference materials are needed. Commonly these reference materials are pure metals and alloys of known composition. Due to the size of the material samples, these materials must have a high homogeneity. Another prerequisite for precise measurement of reference standards for conductivity is the precise knowledge of the dimensions as well as the geometry of the material under test. Typical shapes for a reference material are bars or blocks and the dimensions range from 30 to 80 mm in width, 200–800 mm in length, and 3–10 mm in thickness for bars and 80 mm × 80 mm × 10 mm for blocks. Opposite sides of the blocks and bars have to be parallel and the surface should have mirror finishing. Furthermore, an important issue is the temperature. The resistivity of pure metals strongly depends on temperature. Typical temperature coefficients are of the order of $1 \times 10^{-3} \text{ K}^{-1}$.

For AC measurements of the electrical conductivity based on the eddy current method it is important that the magnetic susceptibility of the material is less than 1.001. Magnetic impurities in the metal influence the conductivity as well as the accuracy of the measurement.

The following section describes the principal methods for the determination of the electrical conductivity of metals.

9.2.2 Principal Methods

In principal, the measurement methods for electrical conductivity can be divided in to two sections, direct current (DC) and alternating current (AC) measurement methods. Applications are found in several fields of

material testing as there are air craft industry, coin manufacturing, and pure metal manufacturing (e.g. copper, aluminum). A more qualitative aspect of conductivity measurements is the nondestructive material testing. Cracks and voids in the material lead to a local change in conductivity which can be detected by conductivity probes. In contrast to the determination of conductivity, in this case the metals may also be magnetic.

The determination of conductivity with DC is made by measuring the resistance R and the dimensions of the conductor (length l , width w , and thickness d , Fig. 9.12). From these measurements, the conductivity σ is calculated (9.1)

$$\sigma = \frac{l}{Rwd} \quad (9.1)$$

The resistance R is usually determined by a voltage-current method. A current I of known value is fed into the sample and the voltage U is measured via point or blade contacts. Since the resistance of metals is typically very low, even for currents of 10 A the voltage drop is of the order of some μV up to several mV. This means high sensitive nanovoltmeters have to be used. The resistance is then calculated according to Ohm's law

$$R = U/I \quad (9.2)$$

This method can only be applied to materials of particular shape like rods or bars. For more complex

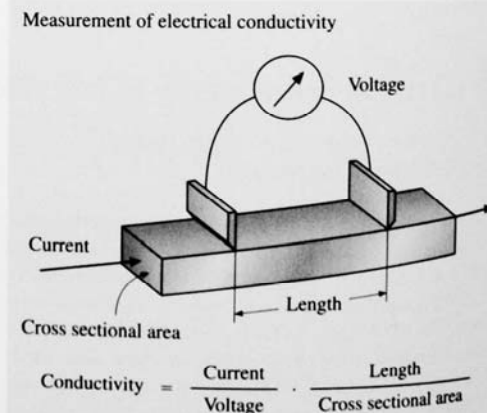


Fig. 9.12 Principle of conductivity measurements. The sample under test is of bar shape with known cross sectional area. A current is passed through the sample in the direction of its longitudinal axis. The voltage drop is measured with two contacts, either point or blade type, at a known distance

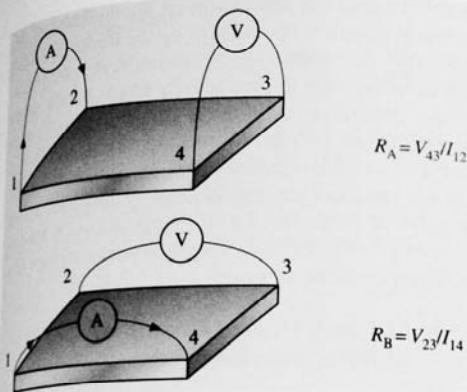


Fig. 9.13 Principle of the van der Pauw measurement. The van der Pauw method requires two measurements. First the current is passed into contacts 1 and 2 and the voltage is measured at contacts 4 and 3, then the current is passed into contacts 1 and 4 and the voltage is measured at contacts 2 and 3. These two voltage-current measurements together with the measurement of the thickness of the device under test allow for the determination of the conductivity

geometries, like, for instance, the surface of an aeroplane, other methods have been developed.

A local determination of the DC conductivity can be obtained by the so-called four-point probe. Four-point electrodes are pressed on the material and a special sequence of voltage-current measurements is made. The basic principle of this method is the van der Pauw method (Fig. 9.13) [9.3, 4]. The van der Pauw method consists of two measurements of resistance, R_A and R_B

$$R_A = V_{43}/I_{12}, \quad R_B = V_{23}/I_{14}. \quad (9.3)$$

From these two measurements and the knowledge of the thickness of the sample under test, the conductivity can be determined by the solution of the following equation

$$e^{-\pi R_A/R_S} + e^{-\pi R_B/R_S} = 1, \quad (9.4)$$

where R_S is the resistance to be determined. If R_A and R_B are similar, (9.3) can be simplified and solved for the conductivity σ as follows

$$\frac{1}{\sigma} = \frac{\pi d}{\ln 2} \frac{(R_A + R_B)}{2}, \quad (9.5)$$

where d is the thickness of the sample. The precision of such a van der Pauw measurement depends on the flatness and parallelism of the surfaces of the sample and on the fact that the contacts are point contacts. An error ε

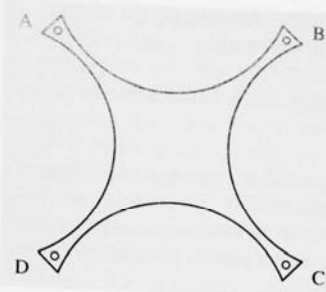


Fig. 9.14 Cross-conductivity standard (after [9.2]). Similar as in Fig. 9.13, the current is either fed into pairs of contact A-B and A-D, and the voltages are measured at contact pairs D-C and B-C

caused by nonideal point contacts can be estimated by

$$\varepsilon = 2.05\lambda^4, \quad (9.6)$$

where, for a sample with square geometry, λ is the ratio of the width of the contact and the length of one side of the square. Such small contact areas lead to the problem of local heating since the current density in these contacts becomes significantly high. On the other hand a reduction of the current will lead to loss of sensitivity. A different approach to this problem is the so-called cross-conductivity standard. If one considers a perfect square and transforms this via conform transformation into a star shaped sample (Fig. 9.14) [9.2]. The conductivity σ is also calculated by (9.4).

DC measurements require a good contact between material and electrodes. In practice, the surface of a metal is covered by a thin oxide layer. For a correct DC measurement this layer has to be penetrated. This problem can be overcome by the AC measurement method. The basic principle of AC measurement methods makes use of eddy currents. Alternating magnetic fields induce currents in conducting materials. If the alternating magnetic fields are induced by a pair of coils, the second coil in turn picks up the magnetic field produced by the eddy current. A probe of such a construction acts as a mutual inductor. The magnetic field, induced in the second coil is a function of the magnitude of the eddy current which in turn depends on the conductivity of the material.

Making conductivity measurements with this method, the skin effect has to be taken into consideration. The skin effect limits the penetration of the eddy currents into the material. The higher the conductivity of the material the smaller is the penetration depth. The penetration depth δ is approximately

$$\delta = \sqrt{\frac{2}{\omega \sigma \mu_0}}, \quad (9.7)$$

where ω is the angular frequency ($2\pi f$) and μ_0 the vacuum permeability.

9.2.3 DC Conductivity, Calibration of Reference Materials

The DC conductivity is given by a simple model

$$\sigma = ne\mu, \quad (9.8)$$

where n is the number of electrons, e is the charge of an electron and μ is its mobility. The number of electrons is nearly the same for all metals, e is constant, but the mobility depends on the lattice parameters of the material.

The basic principles and requirements for the measurement of DC conductivity have been laid out in DIN/IEC 768, *Measurement of Metallic Conductivity* [9.5]. The standard to be measured must fulfil certain criteria regarding its geometry. The length of the sample has to be at least 0.3 m. A DC current is fed in to the end sections and the voltage drop is measured with either sharp point contacts or blade contacts. The distance between these contacts and the current contacts has to be at least 1.5 times the circumference ($2(t + w)$) of the device under test to allow for uniform current distribution between the contact electrodes.

The latest practical approach of this method is shown in Fig. 9.15. The current is fed into the sample via the clamps at the ends and the potential is measured at the knife edge blade contacts. The blades are mounted on a precisely machined stainless steel bar. This method has the advantage that the distance of the blade contacts has only to be determined once and is the same for a whole set of measurements. Also the parallelism of the contacts is assured by this method.

A principal drawback of the DC method is its sensitivity to oxide layers on certain materials (e.g. aluminum). Since a precise knowledge of the thickness of the sample under test is essential, it is practically im-

possible to gain full knowledge of the thickness of an aluminum sample without knowing the thickness of the oxide layer. A consequence of this problem is the possibility of differences in conductivity values for the same material determined with the DC method compared to that determined with the AC method. This problem was subject of an intensive study [9.6, 7]. Although the relative uncertainties for conductivity calibrations are of the order of 0.5% for the AC method and of the order of 0.1% for the DC method, differences between the values could be up to 1%.

9.2.4 AC Conductivity, Calibration of Reference Materials

In principle, one could think of measuring the AC conductivity in the same way as the DC conductivity. But the problem of current displacement at AC current is much more pronounced. Depending on the conductivity and the measuring frequency, the current flows in a thin layer at the surface of the material. The thickness of this layer can be estimated by (9.5). So it is not possible to exactly determine the AC conductivity by a simple current-voltage measurement since one dimension, the thickness, is not known without knowledge of the conductivity. On the other hand, most commercial conductivity meters measure with an AC method. To meet the demand of AC conductivity calibration, a suitable method has been developed at the National Physics Laboratory Teddington, UK (NPL) [9.8].

Alternating electromagnetic fields can penetrate metallic materials and so generate an eddy current in the material. This effect is used in a way that the material under test is induced into a nearly ideal inductor. Due to the eddy currents, the inductor is no longer ideal but shows magnetic loss. This loss can be measured as the resistive part of the inductor and from that resistance the conductivity can be calculated according to (9.9). From two-dimensional theory this resistance R_m can be deduced which is not a real resistance but a process of energy loss modelled by a resistance

$$\sigma = \frac{2\omega(b+d)^2\mu_0 N^4}{R_m^2 l^2}. \quad (9.9)$$

The measurement system used is the so-called Heydweiller bridge (Fig. 9.16). The bridge consists of the mutual inductor M with N windings, two fixed resistors R_1 and R_4 , and the balancing circuit R_{21} , R_{22} , C , and R_v . The mutual inductor is of toroidal shape. It can be opened and a specimen of annular shape of width $b = 80$ mm, thickness $d = 10$ mm, and central circum-

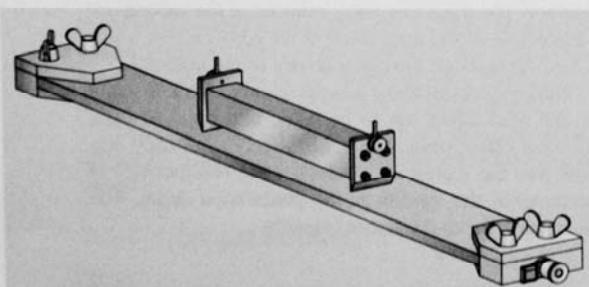


Fig. 9.15 Measurement setup for the determination of the DC conductivity of bar-shaped samples. The potential contacts are of knife edge type

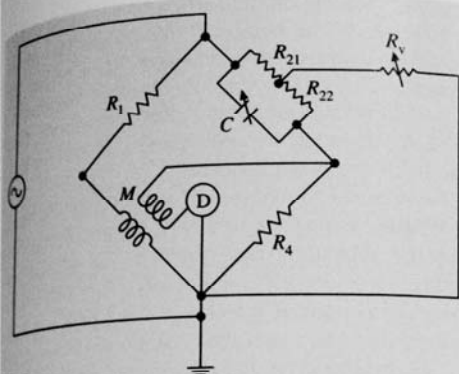


Fig. 9.16 Heydweiller bridge for measuring NPL primary conductivity standards at frequencies from 10 to 100 kHz. The standard under test is brought into the mutual inductor M . From the change in R_v , necessary to balance the bridge, the conductivity can be calculated (R_v = variable resistor, C = variable capacitor, $R_{21} = R_{22} = 10 \text{ k}\Omega$, $R_1 = 1 \text{ k}\Omega$, $C_0 = 10 \text{ nF}$, M = inductor)

reference $l = 320\pi \text{ mm}$, can be inserted. From the change in resistance R_v necessary to balance the bridge, R_m is determined and the conductivity can be calculated.

Since the annulus is of considerable size (0.4 m in diameter), the conductivity value of a selected segment that represents the average value of conductivity of the specimen is transferred to a block shaped sample of size $80 \text{ mm} \times 80 \text{ mm} \times 10 \text{ mm}$. The system used for this transfer is the same bridge system, the mutual inductor is a coil of approximately 80 mm in diameter which can be placed on the annulus as well as on the block. These blocks then can be used as reference material.

9.2.5 Superconductivity

Some metals, alloys, compounds and ceramic materials lose their resistance, if they are cooled down to very low temperatures of some K [9.9]. The physical principle is that in these materials electrons of opposite spin and of opposite momentum form pairs. As these pairs have no spin, they can occupy the same lowest energy state. This state allows dissipation free transport of electrical energy since the pairs are not scattered by the surrounding lattice that means an electrical current is carried without measurable resistivity [9.10]. The transition into this state occurs at a critical temperature T_c and varies with the type of material. For so-called low-temperature superconductors (LTS) the critical temperature is in the range up to 30 K, for high-temperature superconduc-

tors (HTS) T_c can be even higher than 100 K. LTS are typically pure metals or alloys, like e.g. lead (Pb), niobium (Nb), tin (Sn), or Nb_3Sn . The HTS are perovskite crystals of mixed copper oxides. This class of material has been discovered in the mid 1980, first by Bednorz and Müller [9.11]. From that time on, various compositions of copper oxides with rare-earth metals have been investigated [9.12]. The first reproducible composite was barium-lanthanum-copper-oxide (BaLaCuO) which showed a critical temperature of 40 K. For tellurium-barium-calcium-copper-oxide (TBCCO) a T_c of as high as 125 K was observed [9.13].

Superconductors of either type are used for several purposes, as there are

- the transport of electrical energy,
- the generation of high magnetic fields,
- sensitive measurements of small magnetic fields with superconducting quantum interference devices (SQUID) [9.14],
- recently quantum computing, based on QUBITS,
- arrays of superconducting contacts are used as voltage standards.

The first two are DC or low-frequency applications, the other applications make use of the so-called Josephson effect (at radio/microwave frequencies) which is described in detail in [9.15, 16].

Superconductors need low temperatures so applications using LTS are typically operated at the temperature of liquid helium (4.2 K), whereas HTS can be operated at the temperature of liquid nitrogen (77 K). The latter is becoming more and more of interest for industrial applications, since on the one hand it is possible to produce mechanically stable ceramic components (e.g. of YBaCuO), and on the other hand the effort for cooling and thermal isolation is less than that for LTC.

The use of superconductors for the generation of high magnetic fields requires to pay attention to their behavior in magnetic fields. This behavior can be di-

Table 9.4 Some typical values for superconductors

Metal/alloy/material	T_c (K)	B_c (T) at 4.2 K
Tin (Sn)	3.7	0.03
Lead (Pb)	7.3	0.08
Niobium (Nb)	9.2	0.2
Nb_3Sn	19	24
Nb_3Ge	23	38
YBaCuO	93	55
BSCCO	110	29

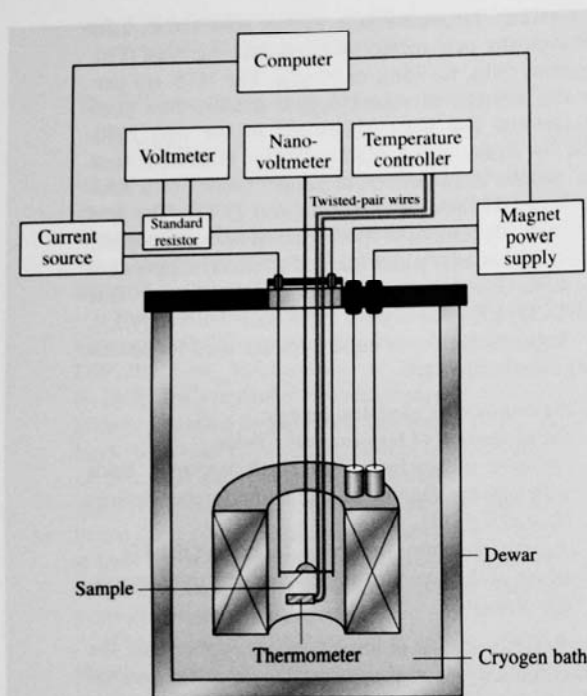


Fig. 9.17 Measurement setup for the characterization of superconductors (after [9.18]). The resistance of the superconductor is determined by a voltage-current measurement. The apparatus allows for the variation of temperature and magnetic field to determine T_c and B_c .

vided into so-called type-I and type-II superconductors. If a superconductor of type-I is kept at a temperature $T < T_c$ and the magnetic induction B is increased there is a critical magnetic induction B_c , where the superconductor becomes normal conducting. Below this B_c ,

screening currents on the surface of the superconductor compensate the magnetic field inside. This means that a type-I superconductor behaves like a perfect diamagnet, $\mu_r = 0$ [9.17]. Since this effect is also observed for a volume surrounded by a superconductor, these type-I superconductors allow perfect shields for magnetic fields at low temperatures.

Superconductors of type-II show a different behavior. With increasing magnetic induction B , the transition from the superconducting state to the normal conducting state occurs continuously with two critical inductions B_{c1} and B_{c2} . Below B_{c1} , a type-II superconductor behaves as one of type-I. At the critical induction B_{c1} , the magnetic field starts to penetrate the conductor creating flux vortices. At the critical induction B_{c2} no more vortices can be created and the magnetic field can completely penetrate the superconductor and it becomes normal conducting. The critical induction B_{c2} is typically much higher than B_{c1} or the B_c of a type-I superconductor. Some properties (T_c and B_c) of typical superconductors are listed in Table 9.4.

The measurement of these parameters are carried out in an apparatus allowing for control of both, temperature and magnetic field by measuring the voltage as a function of current through the superconductor (Fig. 9.17) [9.18].

Similar to the determination of the DC conductivity the voltage drop over a short length of a superconducting strand is measured, passing a DC current I . At constant temperature T and magnetic induction B the current I is varied to determine the critical current density of the material under test. Other possible measurements are the determination of T_c as a function of B or of B_c as a function of T with I kept constant. With these measurements it is possible to characterise a superconductor. Standardized methods for the determination of parameters are described in [9.19].

9.3 Electrolytic Conductivity

The electrolytic conductivity is a measure of the amount of charge transport of ions in solution. While in metals the current is carried by electrons in metals, in electrolyte solutions, molten salts and ionic solids the charge carriers are ions. The extent to which current flows through an electrolyte solution depends on the concentration, charge and mobility of the dissolved ions present.

The SI derived unit of conductivity is siemens per meter (S/m). The symbol for electrolytic conductivity

is κ in chemistry, σ or γ in solid-state physics. Very low conductivity values are often expressed in terms of resistivity ($\rho = 1/\kappa$) in the unit ohm meter ($\Omega \text{ m}$).

9.3.1 Scale of Conductivity

Electrolytic conductivity is a nonspecific sum parameter reflecting the concentration and mobility of all ions dissolved in a solution. Since the mobility of the ions is temperature dependent, the conductivity also depends on

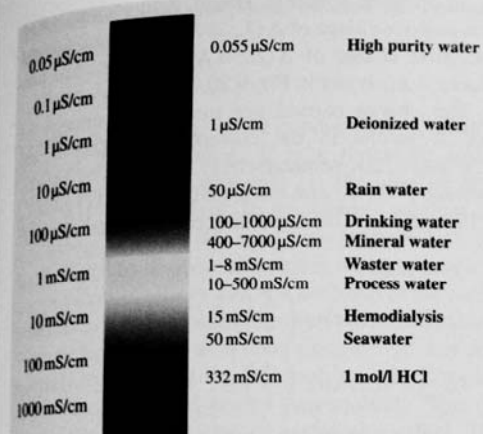


Fig. 9.18 The scale of conductivity with examples of various aqueous solutions at 25 °C

temperature. Sometimes the term *specific conductance* is used to describe conductivity. Since electrolytic conductivity is nonspecific this expression is misleading and should be avoided. Figure 9.18 shows the electrolytic conductivity of different aqueous media at 25 °C.

The measurement of conductivity ranges from quality control of high purified water to waste water treatment monitoring and process control in chemical industry. Electrolytic conductivity can also be used to determine the relative ionic strength of solutions and as a detection technique in ion chromatography.

Electrolytic conductivity is in fact the most widely used parameter to monitor the overall ionic purity of water and it is considered the major parameter defining and ranking grades of purified water, e.g., in pharmaceutical, semiconductor and power plant industries. Electrolytic conductivity measurements are used for the evaluation of water quality under regulations and standard practices, e.g., drinking water and water used in food industry. Important parameters in specific areas as, for instance, the measurement of the amount of total dissolved solids (TDS) and the salinity of sea water are also related to conductivity measurements. Furthermore, electrolytic conductivity is also measured in nonaqueous or mixed solutions like fuels and paints and varnishes, respectively for quality control purposes.

9.3.2 Basic Principles

In a volume, in which a homogeneous electric field is present, the conductivity κ is given as the ratio of the

current density j , generated by the field, and by the electric field strength E

$$\kappa E = j. \quad (9.10)$$

Figure 9.19 schematically shows such a volume with respect to an electrolyte solution. Two parallel electrodes are immersed into the solution and connected to a voltage source. The applied voltage generates a homogeneous electric field in the volume. Positive ions move constantly towards the cathode, while the negative ions move towards the anode.

Ion Mobility

For a volume of a constant cross sectional area A , electrode distance l and with a homogeneous, constant electric field of strength E , the voltage U across the sample between the electrodes is given by

$$U = lE. \quad (9.11)$$

The field exerts a force F on an ion of charge ze according to (9.12), where z is the signed charge number of the ion and e the elementary charge

$$F_z = zeE. \quad (9.12)$$

This force (9.12) accelerates the cations in the direction of the cathode and anions towards the anode. An ion moving through the solvent experiences also a frictional force F_R proportional to its velocity. Assuming Stoke's law of friction is applicable [9.20], the frictional force is given by (9.13) and where r is the radius of

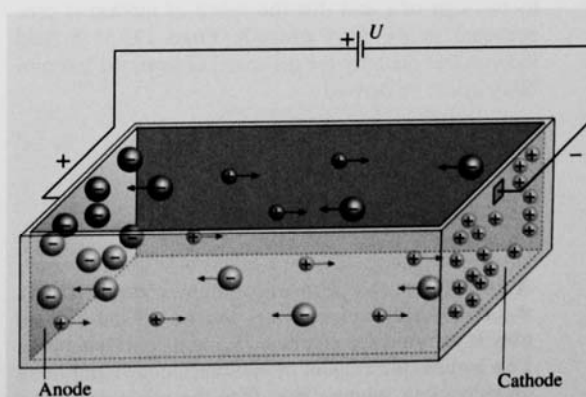


Fig. 9.19 Ions in solution conduct the electric current. The positive ions (cations) constantly move towards the negative electrode (cathode), while the negative ions (anions) move towards the positive electrode (anode)

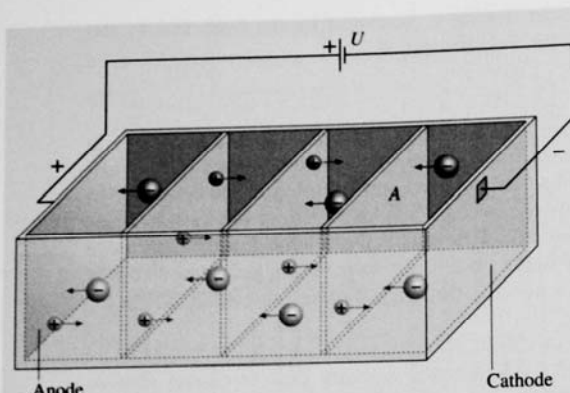


Fig. 9.20 The charge carried per time Δt period through the area A results in the current I_+ and I_- , respectively

the ion, which includes the radius of its solvate shell, η is the viscosity of the solvent and w the speed of ion motion

$$F_R = 6\pi r \eta w. \quad (9.13)$$

The two forces act in opposite direction. After a short time the speed of ion motion reaches a steady state (9.14) and (9.15)

$$F_z = -F_R, \quad (9.14)$$

$$w = E \frac{ze}{6\pi r \eta}. \quad (9.15)$$

Note that the direction of the movement is determined by the sign of z and that the speed of motion is proportional to the field strength. From (9.15) a field independent quantity for the speed of ions, the ion mobility u_i can be derived

$$u = \frac{ze}{6\pi r \eta}, \quad (9.16)$$

with

$$w = uE. \quad (9.17)$$

A strong electrolyte i.e. potassium chloride (KCl), $A_{v+}B_{v-}$ dissociates into v_+ cations A and v_- anions B carrying the charge z_+e and z_-e , respectively. Let's assume the amount of substance concentration of an electrolyte solution is c , then the concentration of cations is v_+c and of anions is v_-c . The number of cations and anions, respectively, per volume is v_+cN_A and v_-cN_A . N_A is Avogadro's constant. In the electric field, cations and anions move with speed w_+ and

w_- in opposite direction. Hence, during a time period Δt a positive charge of $\Delta Q_+ = N_A v_+ c z_+ e w_+ A \Delta t$ and a negative charge of $\Delta Q_- = N_A v_- c z_- e w_- A \Delta t$ pass an area A as shown in Fig. 9.20.

The charge carried per time period through the area A results in the current $I_+ = \Delta Q_+ / \Delta t$ and $I_- = \Delta Q_- / \Delta t$, respectively [9.21]. Inserting Faraday constant F (9.18) and using (9.15) and (9.11) gives I_+ (9.19) and I_- (9.20) depending of the applied voltage U

$$F = N_A e, \quad (9.18)$$

$$I_+ = F v_+ z_+ c u_+ \left(\frac{A}{l} \right) U, \quad (9.19)$$

$$I_- = F v_- z_- c u_- \left(\frac{A}{l} \right) U. \quad (9.20)$$

According to (9.19) and (9.20) an electrolyte solution shows the same electric behaviour as an ohmic resistor $R = \rho(A/l)$, where ρ is the resistivity of the conducting material.

Molar Ionic Conductivity

With Ohm's law (9.21), we find for the conductivity κ_+ (the reciprocal of resistivity) of the cations (9.22),

$$I = \frac{U}{R}, \quad (9.21)$$

$$\kappa_+ = \frac{l}{A} \frac{1}{R_+} = \frac{l}{A} \frac{I_+}{U}. \quad (9.22)$$

Inserting (9.19) into (9.22) yields (9.23) for the molar ionic conductivity λ_{m+} of the cations.

$$\frac{\kappa_+}{v_+ c} = z_+ u_+ F = \lambda_{m+}. \quad (9.23)$$

The molar ionic conductivity λ_{m-} of the anions is derived similarly.

Since the conductivity depends on concentration of all mobile ions, measured values for different solutions are not directly comparable. For this reason the molar conductivity Λ_m of electrolytes (9.24) as the sum of the molar ionic conductivities of anions and cations has been introduced. Equations (9.23) and (9.24) applied to the anions and cations in the solution yield (9.25). The molar conductivity is expressed in $\text{S m}^2 \text{mol}^{-1}$

$$\Lambda_m = v_+ \lambda_{m+} + v_- \lambda_{m-}, \quad (9.24)$$

$$\kappa = c \Lambda_m. \quad (9.25)$$

For strong electrolytes, Kohlrausch's law empirically relates the molar conductivity with concentration according to (9.26) meaning that the molar conductivity

decreases with increasing concentration due to ionic interaction

$$\Lambda_m = \Lambda_m^0 - K\sqrt{c}, \quad (9.26)$$

where Λ_m^0 is the limiting molar conductivity of an electrolyte at infinite dilution, K is a (typically small) constant and depends primarily on the type of electrolyte and on the solvent. In an aqueous solution the ions arrange in a way that on a time average each ion is surrounded by a sphere of counter ions. As a consequence two main effects lead to a decrease of the molar conductivity with increasing electrolytic concentration. When the ions move in an applied electric field they permanently try to rebuild the ionic sphere, which results in a restoring force and lowers their mobility. This effect is called the relaxation or asymmetry effect. The so called electrophoretic effect is a result of the ionic sphere influencing the friction force which a solvated ion experiences when moving through the solution. For a detailed description of the classical Debye-Hückel-Onsager theory and further sophisticated quantitative treatment of the concentration dependence of the conductivity see [9.22, 23]. If the sample contains only the species of interest and if the concentration dependence of this species is known, conductivity measurement can be used to estimate concentration.

Weak electrolytes dissociate only to a certain degree, which depends on the concentration of the weak electrolyte. Therefore the molar conductivity is mainly determined by the nonlinear dependence of the dissociation constant α (9.27) on the electrolyte concentration

$$\alpha = \frac{\Lambda_m}{\Lambda_m^0}. \quad (9.27)$$

The limiting molar conductivity for any electrolyte solution can be expressed in terms of the limiting molar conductivities of the anions and cations (9.28). This relation is known as Kohlrausch's law of the independent motion of ions in electrolyte solutions at infinite dilution

$$\Lambda_m^0 = \nu_+ \lambda_{m+}^0 + \nu_- \lambda_{m-}^0. \quad (9.28)$$

Limiting conductivities of cations and anions in various solvents are listed in [9.23]. The ion mobilities and therefore the limiting ionic molar conductivities of the hydronium and of the hydroxide ions are much larger than for other ions due to a different transport mechanism. Hydronium and hydroxide ions are not transported through the solution but protons are transferred by a sequential von Grotthuss type proton-hopping mechanism through water bridges [9.24].

9.3.3 The Measurement of the Electrolytic Conductivity

Basic Measurement Principle

An equipment to measure the electrolytic conductivity consists of a cell, mostly with built-in temperature probe and a measurement device to determine the resistance (and the temperature) of the cell (conductivity meter). The conductivity cannot be measured directly. According to (9.22) the conductivity $\kappa = \kappa_+ + \kappa_-$ of a solution under investigation is evaluated from the measurement of the resistance R of a sample in the cell and the geometric cell dimensions. In case of two parallel electrodes opposite to each other the geometric parameters in (9.22) are combined in terms of the cell constant K (9.29).

$$K = \frac{l}{A}. \quad (9.29)$$

K is equal to 1.0 cm^{-1} if the current flow contained within 1 cm^3 of sample solution is between the two electrodes of 1 cm^2 area and in a distance of 1 cm . The so-called standard cell is shown in Fig. 9.21.

The cells shown in Figs. 9.19 and 9.21 are idealized. In practice, side effects must be taken into account. These effects in particular include effects at the electrode-solution interface: electrode polarisation, i. e. accumulation of ions at the electrodes (so-called double layer capacitance), charge transfer across the electrodes (polarization resistance) and adsorption/desorption phenomena. Additionally, fringing electric fields at the

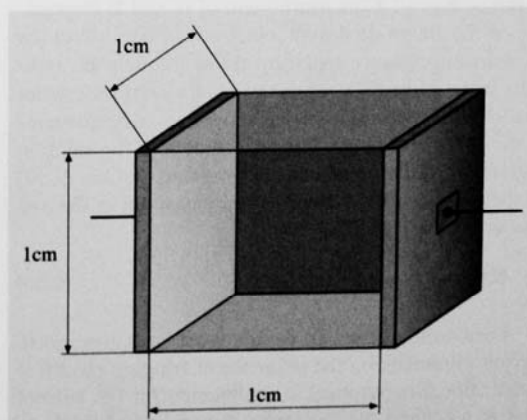


Fig. 9.21 For a standard cell, the volume of the sample solution is the area of the electrode times the distance between the electrodes

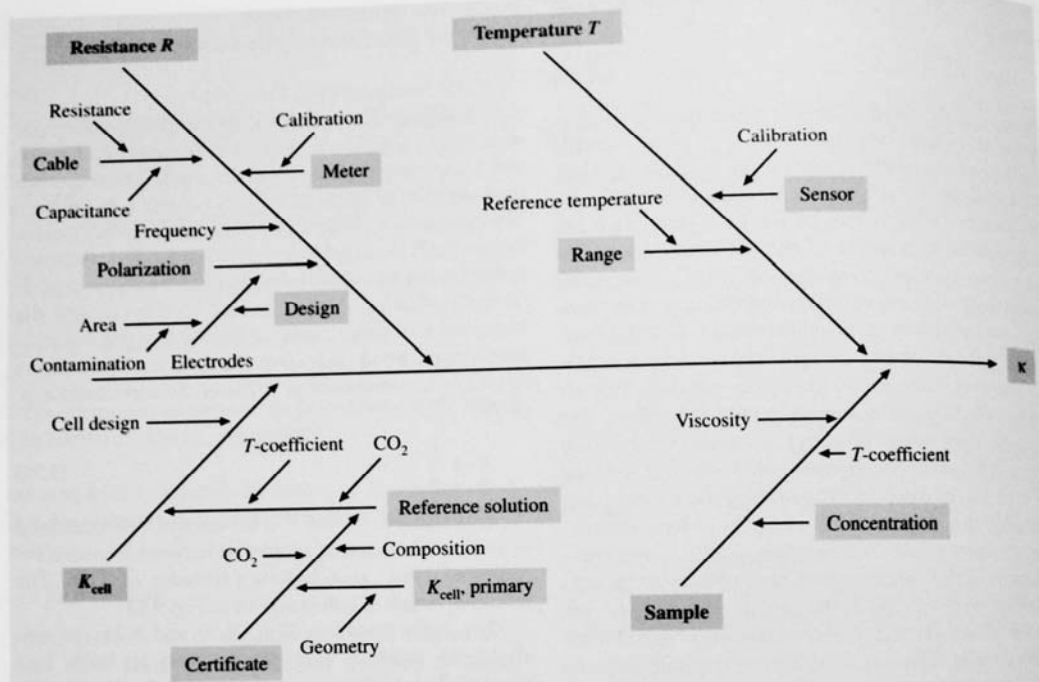


Fig. 9.22 The relevant uncertainty sources and their relationship are shown in a cause and effect diagram (fishbone)

cell margin and the geometric capacitance of the two electrodes affect the measured resistance. The solution resistance is therefore typically determined from impedance measurements $Z_i(f_i)$ at various frequencies f_i rather than a DC measurement of U and I . Depending on the electrode design, electrode effects affect the measured impedance spectrum at low frequencies, typically up to a few kHz, while the influence of the (rather small) geometric capacitance shows up at frequencies in the upper kHz range. The resistance R of the solution therefore can be derived from an extrapolation (9.30) of the real part of the impedances measured in the low frequency range [9.25]

$$R = \lim_{(1/f) \rightarrow 0} \operatorname{Re}\{Z_i(f_i)\}. \quad (9.30)$$

Furthermore, the cell design must be optimized to permit minimization the influence of fringing electrical fields. For this purposes a confinement of the current path to a defined volume having a large cross section A , and a small electrode distance is desirable. On the other hand this reduces the measured resistance. This is of disadvantage for the conductivity measurement of solu-

tions having large conductivities, since the uncertainty of resistance measurements increases for resistances in the ohm and milliohm region. Hence, geometric and electric properties of a conductivity cell are typically optimised for a conductivity range of interest.

If the cell constant K is determined from the geometric dimensions of the cell and if the resistance is measured traceable back to the SI, such as outlined above, the resulting conductivity of a solution is traceable to the SI unit S m^{-1} . Such *primary cells* are used to measure the conductivity of primary reference solutions (primary standards). Aqueous solutions of potassium chloride are usually used for this purpose. In a traceability chain, the known electrolytic conductivity of primary standard is used to calibrate conductivity cells of unknown cell constant. These cells are then used together with properly calibrated conductivity meters for routine measurements the results of which are traceable to the SI unit S m^{-1} [9.26]. Calibration and measurements of such devices are usually performed at a single frequency. On a worldwide scale the equivalence of the existing national primary measurement standards are ensured by means of international comparison measurements.

The best way to obtain all information on possible sources of uncertainty on the resulting conductivity of the sample is a cause and effect diagram shown in Fig. 9.22. This fishbone visualizes the relationship of the uncertainty sources. The main sources of uncertainty are the measurement of the resistance of the sample, the sample temperature, the cell constant and the stability of the sample.

Temperature Influence on Electrolytic Conductivity

The conductivity of a solution depends on temperature. Consequently, only conductivity values obtained at the same measurement temperature can be compared. The concept of reference temperatures (mostly 25 °C) was introduced to solve this problem. A temperature correction function allows the conductivity meter to convert the actually measured conductivity to that of the reference temperature.

There are three ways to deal with the temperature dependence of conductivity

- No correction (according to the specification of the United States Pharmacopeia (USP) [9.27]) for water used in pharmaceutical industry, like water for injection (WFI);
- Linear correction to a reference temperature, which is, depending on the target uncertainty, appropriate for small deviations of up to 1 °C;
- Nonlinear correction (e.g. for natural waters according to ISO 7888 [9.28]).

The standard uncertainty of the temperature should be $u = 0.1$ K or better. For low target uncertainty it is recommended to thermostat the sample so that the same temperature is used for calibration and measurement.

Primary Cells

The conductivity of primary reference solutions are measured by means of conductivity cells with cell constants, which are determined by geometric measurements. Various cell types have been tested in the past on their ability to avoid or minimize fringe effects and stray fields typical for two-electrode cells as seen from Fig. 9.22. Two common models are shown in Figs. 9.23 and 9.24.

The cell type schematically shown in Fig. 9.24 was developed at the National Institute of Standards and Technology (NIST, Gaithersburg) [9.29]. The so-called Jones cell [9.30] is based on the principle of a geometrically measured, removable center section. The cell constant is primarily determined by the cross sec-

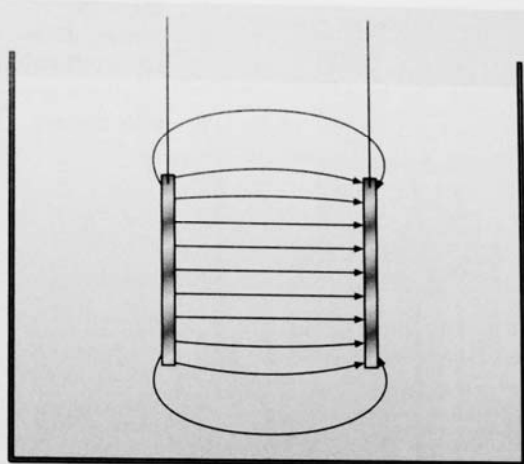


Fig. 9.23 Fringe effects occur on the edge of a two-electrode cell. If the field is not homogeneous it is not possible to determine the cell constant by a geometrical approach

tional area and length Δl of the glass tube separating the platinum electrodes rather than by the size of the electrodes themselves. In this primary cell the resistance of the solution can be reduced by removing the center section. The difference in the measured resistances is therefore correlated to the length of the removable center section. The conductivity of the sample can

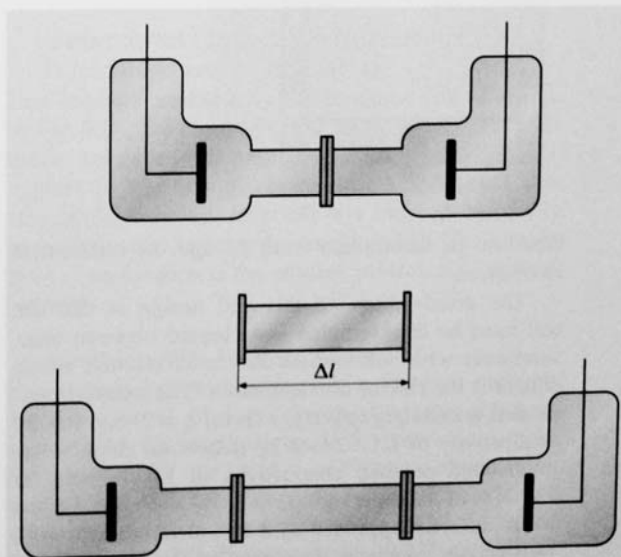


Fig. 9.24 Jones-type primary cell with removable center section

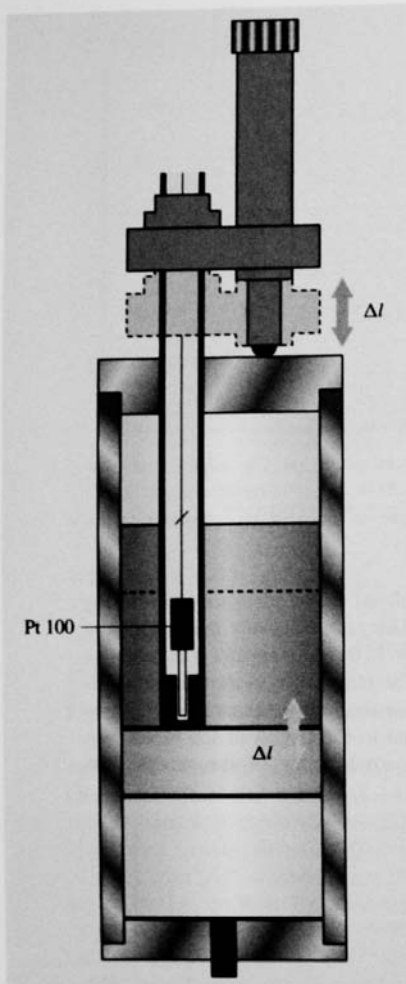


Fig. 9.25
Primary differential cell with adjustable electrode distance

therefore be determined from Δl and the differential resistance.

The disadvantage of this cell design is that the cell must be disassembled and cleaned between measurements with and without the center section which enhances the risk of contamination. The relatively expanded uncertainty (coverage factor $k = 2$) e.g. for the conductivity of a 0.01 mol/kg potassium chloride solution with nominal conductivity of 1.41 mS/cm (at 25 °C) is of the order of 0.03%.

A different approach of a two-electrode cell with well-known geometry developed at the Physikalisch-Technische Bundesanstalt (PTB, Braunschweig) [9.31]

goes back to *Saulnier* [9.32, 33]. In this design one electrode is mounted on a movable piston. The distance between the two electrodes can be adjusted very precisely without the cell being disassembled. The cell design is shown in Fig. 9.25. The cross-sectional area is constant and is determined by the internal diameter of the cylindrical tube. The two electrodes are made of Pt, directly vapour deposited onto the electrode bodies [9.34]. If the spacing between the two electrodes is large enough, the distribution of the electric field in the bulk solution is not influenced by the movement. Therefore the difference in the measured resistances then can be attributed to the change Δl of the distance between the electrodes, so that conductivity can be calculated from the differential values, quite similar to the Jones cell.

Four-Terminal DC Cell

Conductivity measurements of a primary reference solution can also be performed using a four-electrode DC cell [9.35]. This method can be applied at higher conductivities, i. e. at low resistances. It has the advantage [9.26] to avoid the reactive effects typical of AC circuits. Measurements are effected by two outer Pt current electrodes, which imprint a constant current to cell, and two inner electrodes to measure the voltage drop across a portion of the cell. The current has to be kept relatively low to avoid heating the solution and electrolysis. Reversible potential electrodes are required to eliminate any polarization effect. The traceable value of the cell constant is directly determined through the geometry of a center glass tube precisely bored at which ends the potential electrodes are located.

Commercial Conductivity Cells – Two-Electrode Cell

The two-electrode cell as shown in Fig. 9.26 is the classical conductivity cell sometimes called Kohlrausch cell.

The two-electrode cell consists of two parallel electrodes immersed in the sample solution. An AC current

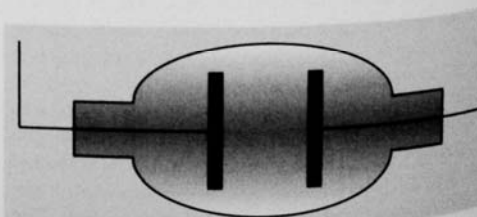


Fig. 9.26 Classical two-electrode conductivity cell

at a single frequency is typically applied and the resulting voltage is measured. Stray field and polarization effects influence the measurement. These effects must be kept under control in order to measure only the bulk resistance of the sample. Polarization is a side effect of the contact of electronically conducting electrodes with a solution showing ionic conduction. A charge buildup occurs at the electrical double layer at the electrode-solution interface and causes a voltage drop across the electrode surface. As a consequence, the measurements can, in general, not be performed with DC but have to be carried out with AC in the frequency range of typically up to 5 kHz.

The deposition of a platinum black layer on a platinum electrode (platinization) also reduces the polarization effect by increasing the electrode surface [9.36]. This increases the double layer capacitance so that the measured impedance is virtually resistive.

It is important to choose the right frequency for the respective application, which significantly depends on the cell design and the solution under investigation. In general, low frequencies in the sub-kHz region can be applied at low conductivities. In this range the polarization is negligible compared to the bulk resistance of the sample. Frequencies in the low kHz region must be applied at high conductivities in order to minimize the influence of electrode polarization.

A disadvantage of the two-electrode cells is that any changes of the electrode surface such as corrosion or coatings influence the measurement result. If the electrodes are covered by platinum black any scratch or other damage would change the surface and therefore the cell constant.

Four-Electrode Cell

The four-electrode cell reduces the problem of polarization effects. Changes of the electrode surface like blocking and coating do not influence the measurement result. A typical four-electrode cell as oversimplified shown in Fig. 9.27 consists of four concentric rings. One outer pair of current electrodes and one inner pair of voltage electrodes. A constant AC current is applied to the outer pair of rings. The voltage is measured on

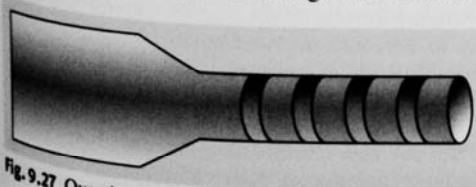


Fig. 9.27 Oversimplified four-electrode cell

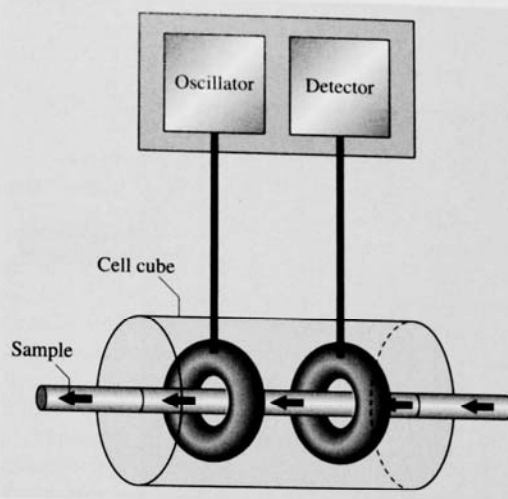


Fig. 9.28 Toroidal inductive conductivity cell

the inner rings with a large input impedance of the impedance meter to reduce polarization effects.

Three-Electrode Cells

The three-electrode cell type is nowadays almost completely replaced by the four-electrode cell. In a three-pole cell a third pole is connected to one electrode of a two electrode cell, which serves to guide the electrical field. In this way the stray-field can be reduced [9.37].

Electrodeless Conductivity Measurements – Toroidal Inductive Conductivity

In a toroidal conductivity measurement cell as shown in Fig. 9.28, the electrodes are located outside the solution being investigated. An oscillating potential is applied to the first electrode, which induces a current in the solution. Inversely the induced current is measured with the second toroidal coil [9.38]. A main field of application is the process control, e.g., in food industry.

Monitoring the Purity of Water

Since electrolytic conductivity is a sensitive measure for the amount of ions dissolved in the solution, a threshold for conductivity is a clear and simple specification for the quality and purity of water in general but also for high-purity water. The relevant measuring range is below 0.1 mS/m (0.06–1 μ S/cm at 25 °C). The US Pharmacopoeia [9.27] as well as the European one [9.39] have specified the standard

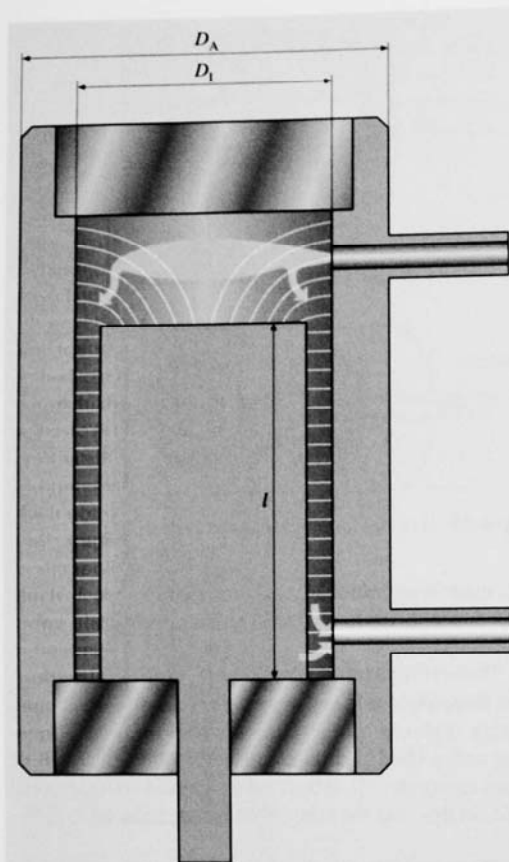


Fig. 9.29 Flow-through cell for the low conductivity range. For this closed cell type the influence of air-borne contaminations like carbon dioxide on the measurement result can be avoided

for purified water, highly purified water and water for injection for the pharmaceutical industry based on conductivity measurements. Sectors that also use conductivity thresholds for water purity are electrical power plants, food industry, electronic industry and analytical laboratories.

In the sub-mS/m region no certified aqueous reference solutions are available, because the conductivity of aqueous solutions is not stable due to the influence of atmospheric carbon dioxide (CO_2). CO_2 dissolves in water and partly forms carbonic acid. By that it contributes to the measured conductivity value in the order of 0.1 mS/m, depending on the partial CO_2 pressure present during the measurement. To compensate for the

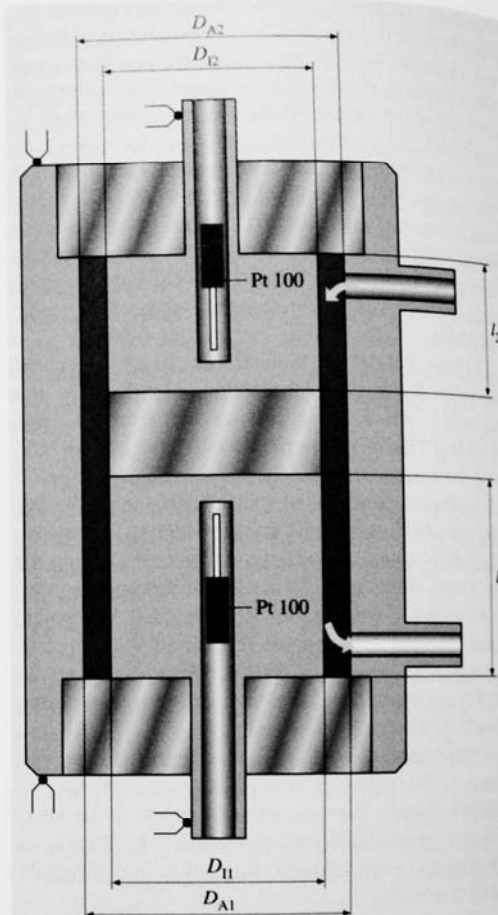


Fig. 9.30 Primary flow-through cell for in-line conductivity measurements in the high-purity water range. The concentric cell consists of two inner electrodes of different length and one outer electrode. The gap between the inner electrodes is filled with inert material

absence of certified reference solutions, a calibration method based on high-purity water as a standard has become widely accepted by the users of low conductivity measuring devices [9.40]. For this purpose it is necessary to determine the conductivity of high-purity water traceable to the SI unit S/m.

Flow-Through Cell for the Low-Conductivity Range

The most common cell design for in-line applications in the high-purity water range is shown in Fig. 9.29. The

concentric design minimizes electromagnetic interference [9.41] and is suitable for integration of the cell into a closed loop. Contamination with atmospheric carbon dioxide from surrounding air is avoided for this type of cell. For calibration it is integrated into a closed loop of purified water together with a reference cell of known cell constant, which is used to measure the conductivity of the purified water. In this way the purified water in the loop is used as a *transient* reference material to calibrate the commercial cell in-line and at the same temperature.

The principle of a primary reference flow-through cell [9.42] is shown in Fig. 9.30. It consists of two inner cylindrical electrodes of different lengths l_1 and l_2 and an concentric outer electrode, which herby form two conductivity measurement cells. The gap between the inner electrodes is filled with inert, nonconducting material. Platinum resistance temperature sensors are mounted in each inner electrode. The cell constant of each cell can be calculated from the inner and outer diameter D_i and D_o , respectively, and from the lengths of the inner electrodes according to (9.31). Fringe effects at the holes and at the end of the electrodes are considered in terms of an effective stray

length a

$$\begin{aligned} K_1 &= \frac{\ln(D_o/D_i)}{2\pi(l_1 + a)}, \\ K_2 &= \frac{\ln(D_o/D_i)}{2\pi(l_2 + a)}. \end{aligned} \quad (9.31)$$

Since the two cells just differ in length, a can be assumed equal for both cells. Using $\kappa = K_1/R_1 = K_2/R_2$ (9.22) the effective stray length can be calculated from the measured resistances R_1 and R_2 of the pure water in the two cells. The cell constants are of the order of 1 m^{-1} with a relative expanded target uncertainty ($k = 2$) smaller than 0.5%. Because cell dimensions, resistance and temperature measurements are measured traceable to the SI unit, the conductivity of the high-purity water can thus be determined in the SI unit S/m.

Another promising design of a primary flow-through cell is based on the on the so-called van der Pauw principle which is used extensively in solid-state physics to measure surface resistivity. The principle is based on a theorem similar to that of Lambert used for the determination of the capacitance unit. The theorem can be applied to a cell with constant cross section and with four electrodes at the edges [9.43].

9.4 Semiconductors

Semiconductor materials offer a wide range of conductivity according to their free carrier concentration, starting from the intrinsic conductivity (10^{-8} S/cm) up to 10^5 S/cm by controlling the doping concentration from 10^{12} up to 10^{21} cm^{-3} . Thus, the determination of the conductivity, conductivity type (n- or p-doped), and the related majority carrier mobility are the most important characterizations, especially in the case of newly developed materials.

After these majority carrier properties are known, minority carrier properties come into consideration, which are mainly related to lattice defects (vacancies and interstitials), but also to chemical impurities, which produce (deep) electron or hole states within the band gap. The most important parameter is the minority carrier lifetime which is applied to describe leakage currents of p-n junctions, charge storage times in dynamic memory cells or sensitivity of charge-coupled device light sensors.

With respect to high-speed devices, like e.g. bipolar transistors or photodiodes, saturated drift velocity values are needed to estimate the high-speed performance.

Many semiconductor devices reach their operating limits with respect to some breakdown mechanisms, like the onset of tunneling currents or impact ionization.

Table 9.5 gives a selected list on semiconductor properties and related methods to determine their values. The following paragraphs give some guidance to determine the most relevant parameters useful for device simulation, device design, and device analyses.

As all semiconductor devices need a more or less ideal contacting of their active regions via metallization of ohmic contacts, the final section collects measurements methods for specific contact resistances.

9.4.1 Conductivity Measurements

Conductivity measurements on semiconductors are predominantly related to bulk material, e.g. semiconductor wafers and epitaxial layers or layer stacks. The conductivity σ (S/cm) is related to the specific resistance ρ ($\Omega \text{ cm}$)

$$\sigma = \frac{1}{\rho}. \quad (9.32)$$

Table 9.5 Overview on selected semiconductor properties and related characterization methods

Property	Symbol	Characterization method
Specific resistance	ρ	Four-point probe, van der Pauw method
Conductivity type	(n- or p-type)	Thermoprobe, Hall effect
Carrier concentration	n, p	Hall effect, capacitance-voltage (C-V)
Carrier mobility	μ_n, μ_p	Hall effect with resistivity
Compensation ratio	$N_A/N_D, N_D/N_A$	Temperature dependence of Hall coefficient
In-depth doping profile	$N(x)$	Capacitance-voltage (C-V), Hall effect with selective layer removal, spreading resistance on beveled samples
Diffusion length	L_n, L_p	Junction photocurrent, electron beam induced currents (EBIC)
Saturated drift velocities	$v_{n,sat}, v_{p,sat}$	I-V analysis (Kelvin method)
Ionization rates by electrons or holes (impact ionization)	α_n, α_h	Temperature resolved I-V analyses
Minority carrier lifetime	τ_n, τ_p	I-V analysis, photoconductivity
Deep states (traps): density, thermal emission rates, capture cross sections, energy level	$N_t, e_n, e_p, \sigma_n, \sigma_p, E_t$	Deep level transient spectroscopy (DLTS)

The conductivity can be calculated from basic semiconductor properties in case of dominating electron conduction

$$\sigma = q\mu n, \quad (9.33)$$

with the elementary charge q (1.602×10^{-19} A s), the carrier mobility μ (unit $\text{cm}^2/(\text{V s})$), and the carrier density n (unit cm^{-3}).

If both carrier types (electrons and holes) are concerned, the conductivity is deduced from

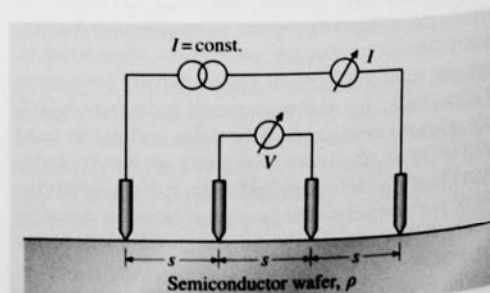
$$\sigma = q\mu_n n + q\mu_p p. \quad (9.34)$$

The standard method for measuring the specific resistance of bulk materials and thin layers is the four-point probe [9.44]. This method is well established for silicon and germanium but works as well on GaAs, InP, and other III-V compound materials. By applying the method to beveled surfaces, in-depth resistivity profiles can be deduced (spreading resistance method [9.45]).

The basic measurement setup of the four-point probe (c.f. e.g. DIN Norm 50431) is depicted in Fig. 9.31. A measurement head comprising four spring-loaded needles with equal distances s (e.g. $s = 1$ mm), is pressed onto the semiconductor sample with a pressure ensuring good near-ohmic contacts, but soft enough not

to produce visible damage. The measurement current I is fed via the outer needles through the sample. The voltage V is measured between the inner needles. Assuming a constant current source with nearly infinite source impedance and a voltage meter with nearly infinite input resistance, possible contact voltages at the needles due to the current flow can be neglected in this Kelvin-like setup. The specific resistance of the sample is

$$\rho = \frac{V}{I} c, \quad (9.35)$$

**Fig. 9.31** Four-point probe on a semiinfinite semiconductor wafer with specific resistance ρ

with c denoting a geometry dependent correction factor, depending on the sample dimensions and the needle distances. The following constraints have to be fulfilled in all sample configurations for accurate measurement within inaccuracies below 1%

- nearly ohmic contacts between the needles and the semiconductor,
- negligible heating of the sample due to the measurement current I (mA range),
- no excess injection of carriers, which would lead to excess conduction (dark measurement),
- no extreme surface potential induced surface band bendings; otherwise leading to stronger surface accumulation or surface inversion layers which would affect the bulk conduction.

In the following sections the correction factor c is given for different samples geometries.

Conductivity of Thin Layer Samples

The measurement setup of the four-point probe applied to a laterally infinitely extended thin layer of thickness d and specific resistance ρ , grown on a semiinsulating wafer is depicted in Fig. 9.32. The specific resistance (unit $\Omega \text{ cm}$) of the layer can be deduced from the measured voltage V , induced by the current I using

$$\rho = \frac{V}{I} d \frac{\pi}{\ln 2}. \quad (9.36)$$

An error in the evaluation of the specific resistance approaches 1%, if the layer thickness d would be one half of the needle distance s . This error would increase to 8%, if the layer thickness d would equal the needle distance s . Normally, needle distances of 1 mm are used, thus, for layer thickness values in the 1–10 μm range this systematic error can be neglected easily. This solution is also applicable in all cases, where the lateral dimensions of the sample are much larger than the threefold measurement-tip distance. If the latter condition cannot be met a setup as in Fig. 9.33 has to be used.

Conductivity of Semiinfinite Bulk Samples

The measurement setup of the four-point probe applied to a semiinfinite bulk sample with a specific resistance ρ , is depicted in Fig. 9.34. The specific resistance of the semiinfinite bulk sample can be deduced from the measured inner voltage V induced by the outer current I by

$$\rho = \frac{V}{I} s 2\pi. \quad (9.37)$$

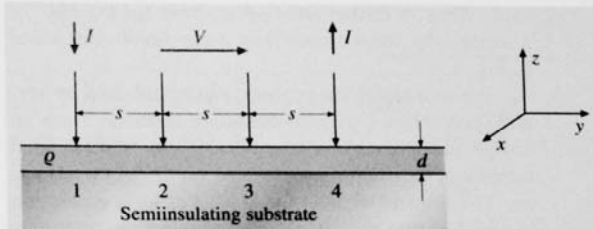


Fig. 9.32 Four-point probe applied to a thin, infinitely extended layer of thickness d and specific resistance ρ ; the measured layer is isolated by a semiinsulating substrate

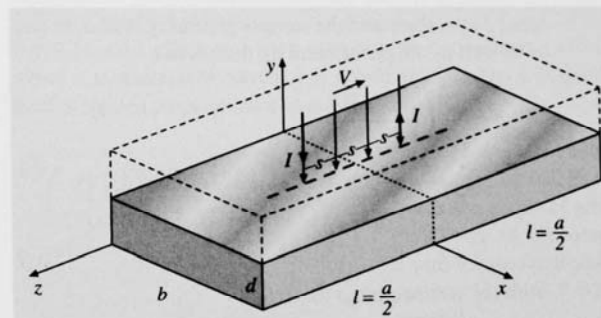


Fig. 9.33 Four-point probe on a thin, rectangular shaped layer of dimensions $a \times b \times d$ with a specific resistance ρ ; the measured layer may be isolated by an underlying semiinsulating substrate or a p-n isolation

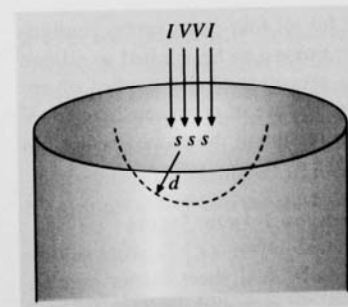


Fig. 9.34 Four-point probe on a semi-infinite bulk sample with a specific resistance ρ ; the radius of the measured volume is defined roughly by $d > 3.5 s$

This is valid under the assumption, that the radius of the measurement volume $d > 3.5 s$, with s denoting the equal spaces s of the needle setup.

Conductivity of Rectangular Shaped Small Samples

In some cases, the samples to be characterized exhibit neither the shape of a semiinfinite bulk sample nor the structure of a laterally infinitely extended thin

layer. Thus, a further solution is given for the case of a rectangular shaped sample of finite dimensions a and b (Fig. 9.33).

The solution of this problem can be obtained by several approaches, like finite difference methods. Here, an analytical approach of Hansen [9.46] may be mentioned which can be easily implemented on desktop computers. The Laplace equation is solved using a separation of variables and applying standard boundary conditions on the doubled sample (see dotted lines in Fig. 9.33) without changing the field and current line conditions in the original sample. A series expansion is developed in [9.46] to deduce the specific resistance ρ from measured I - V values and the sample geometry data a , b , and d as well as the probe head tip distances s

$$\rho = \frac{V}{I} \left(\frac{s}{bd} + \frac{8}{bd} \times \sum_{m=0}^{\infty} \sum_{n=0}^{\infty} \frac{\cosh \beta(l - 3s/2) \sinh(\beta s/2)}{(1 + \delta_{0,m})(1 + \delta_{0,n}) \beta \cosh(\beta l)} \right)^{-1} \quad (9.38)$$

with (m, n) unequal to $(0, 0)$ and

$$\beta = \frac{2\pi}{b} \left[m^2 + \left(\frac{nb}{2d} \right)^2 \right]^{1/2} \quad (9.39)$$

and $\delta_{r,s}$ = Kronecker's delta ($\delta_{0,m} = 1$ ($m = 0$) or 0 ($m > 0$)).

A general remark for all four-point probe configurations: the four-point probe can be applied to silicon and germanium using pressures of the needles of approximately up to 50 p; in case of more sensitive III-V materials like InP, the pressure of the probe needles has to be reduced to around 5 p.

Conductivity of Isotype 2-Layer Stacks

If there are two adjacent layers (1, 2) with isotype conduction type with individual sheet carrier concentrations $n_{1,2}$ (unit cm^{-2}) and mobilities $\mu_{1,2}$ (unit $\text{cm}^2/\text{V s}$), contributing to the total sheet conductance δ_s , the resulting mixed conductance in terms of the effective sheet carrier density n_s and effective mobility μ_s can be calculated from the conductances of the single layers according to [9.47]

$$n_s = \frac{(\mu_1 n_1 + \mu_2 n_2)^2}{\mu_1^2 n_1 + \mu_2^2 n_2} \quad (9.40)$$

$$\mu_s = \frac{\mu_1^2 n_1 + \mu_2^2 n_2}{\mu_1 n_1 + \mu_2 n_2} \quad (9.41)$$

It is assumed that the adjacent isotype layers are grown either on a semiinsulating buffer layer or together being isolated by a pn-junction from the substrate. Thus, the substrate or buffer conductance should be negligible in this two-layer mixed conduction model.

9.4.2 Mobility Measurements

The mobility μ of the majority carriers is extracted by a two-step procedure applying van der Pauw test structures [9.48]. Firstly, the specific resistance ρ is measured, secondly the carrier concentration n is determined. Both measurement setups use the same test structure but apply different schemes for contacting to feed the measurement current into the sample and to measure the resulting voltages. In a final step the mobility is deduced from the equation $\sigma = q\mu n$ solved for μ

$$\mu = \frac{\sigma}{qn} = \frac{1}{qn\rho} \quad (9.42)$$

The term $|1/(qn)|$ is the Hall constant, which is indicative of the carrier concentration n within the test sample. Thus, the mobility can also be written as

$$\mu = \frac{R_H}{\rho} = R_H \sigma \quad (9.43)$$

Due to the fact that the Hall effect is polarity sensitive with respect to the conduction type, the sign of the Hall constant comprises the information of the dominating carrier type: negative sign – n-type, positive sign – p-type. In the following, the Hall effect is explained in more detail and some van der Pauw test structures will be discussed.

Hall Effect, van der Pauw Structures

The Hall effect after Hall (1879) denotes the onset of a voltage V_H at a long thin sample of length a , where a current I is driven through the long axis and a magnetic field B is applied perpendicular to the sample (Fig. 9.35). Due to the balance of the Lorentz force $F = qv \times B$ and the electric field force due to E_H of the Hall voltage, the Hall voltage for an n-type sample can be deduced after integrating over the transverse field E_H

$$V_H = -\frac{1}{nq} \frac{I}{d} B \quad (9.44)$$

The term $-1/(nq)$ is known as the Hall constant R_H of the sample, the sign of which depends on the carrier type. In case of a p-type sample, the Hall constant has a positive sign.

Thus, the Hall effect can be used to determine the dominant carrier or conduction type of an unknown semiconductor sample.

The Hall voltage of either type can be written as

$$V_H = R_H \frac{1}{d} IB, \quad (9.45)$$

with voltage signs $+/- \leftrightarrow$ p/n-type conduction.

When Hall's constant R_H is determined, the carrier concentration can be deduced

$$n, p = \frac{1}{qR_H} \quad (9.46)$$

(with n, p due to a negative, positive sign, respectively)

In principle, the mobility value can now be calculated from (9.43) assuming that the conductivity of the sample was determined by the four-point probe before. This method applying two different test samples would work but it is rather impractical. A more convenient way was published in [9.48], where a disk of arbitrary shape can be used for both types of measurement. In practice, later a rectangular sample is preferred. The original van der Pauw sample type is shown in Fig. 9.36; the sample must not contain any holes. The van der Pauw sample is used in two measurement configurations

1. For the measurement of the specific resistance.

The current I is fed into contacts M, N and the voltage V is taken at contacts P, O. This I - V configuration can be cycled around 90° , and the voltage at M, P taken, too. Thus, two resistances are built: $R_{MN,OP}$ and $R_{NO,PM}$. In [9.48], it is shown by a conformal mapping method that the sample's specific resistance obeys van der Pauw's equation

$$e^{[-(\pi d/\rho)R_{MN,OP}]} + e^{[-(\pi d/\rho)R_{NO,PM}]} = 1. \quad (9.47)$$

The specific resistance can be solved from (9.47) graphically or numerically, e.g. by a Newton method. For the practically preferred rectangular sample geometry the specific resistance can be deduced from

$$\rho = \frac{\pi d}{\ln 2} R_{MN,OP}. \quad (9.48)$$

In this symmetrical case, the I - V configuration can be rotated four times by 90° and the resulting four voltage values can be averaged. Additionally, the current polarity can be reversed and the resulting voltages averaged again. Thus small asymmetries of the sample can be averaged by taking the mean value of eight measurements. More elaborate evaluation procedures in cases of asymmetric I - V measurements in the van der Pauw configuration are given in [9.44].

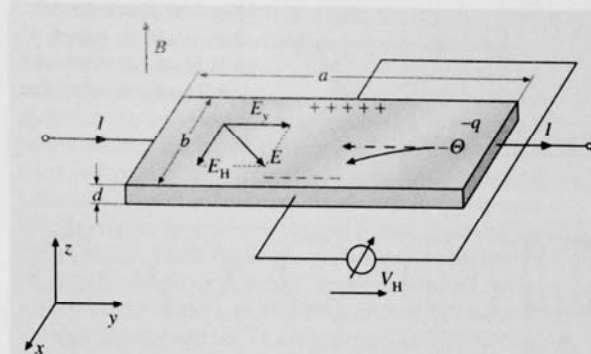


Fig. 9.35 Hall effect at a long sample with dimensions $a \times b \times d$, where a measurement current I is driven along a , and a magnetic field is applied perpendicular to a, b in z -direction

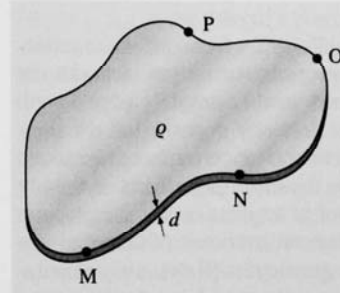


Fig. 9.36 van der Pauw test sample of specific resistance ρ , disc of arbitrary shape of thickness d with infinitesimal small contacts M, N, O, P at its periphery

2. For measurement of the carrier concentration.

For the determination of the carrier concentration from a Hall measurement at the van der Pauw sample, the I - V setup is modified in which the current and voltage contacts are now crossed. The Hall constant is determined in this case by forming the average out of two measurements

$$R_H = \frac{d}{B} \left(\frac{R_{NP,OM} + R_{OM,PN}}{2} \right). \quad (9.49)$$

This scheme can also be improved by averaging over eight Hall resistance terms, as given in [9.44]. The carrier mobility is now deduced using (9.43), (9.49) together with (9.48).

Van der Pauw Test Structures

It was mentioned before, that a rectangular test sample with quite small contacts at the corners can be used favorably for the van der Pauw measurements (Fig. 9.37). The ideal infinitesimally small contacts can be approached by soldering $500 \mu\text{m}$ Sn balls into the

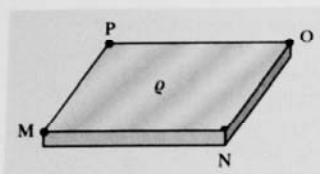


Fig. 9.37 Quadratic van der Pauw test sample with ideal infinitesimally small contacts in the four corners



Fig. 9.38a-e van der Pauw test samples with nonideal finite contact sizes (after [9.44])

corners of the sample while using sample sizes of, e.g. $> 5 \times 5 \text{ mm}^2$.

However, real samples suffer from different nonidealities of the sample preparation; the contacts are not small enough compared to the sample's edge length or the contacts are not correctly deposited at the sample's corners. Respective correction terms can be found in [9.44]. To overcome the distorting effects of finitely extended contacts, a lot of alternative test samples are in use. Figure 9.38 gives an overview of common van der Pauw test sample geometries [9.44]. Very popular is the clover-leaf structure (e), which can be fabricated by ultrasonic cutting and which does not need further electrical corrections even in the presence of finite contacts. Very precise results can also be obtained from the greek cross structure (b). Many discussions concerning ease of fabrication, fragility, heat dissipation, and needs of correction factors can be found in [9.44].

Temperature Dependent Carrier Concentration and Compensation

The carrier concentration determined by the standard Hall technique described so far is assumed to represent the value of the dopant concentration as well. This is valid when a complete dopant ionization can be assumed. In practice, at least two additional aspects have to be considered.

Temperature Dependent Carrier Concentration (Dopant Ionization $< 100\%$)

The mobile carrier concentration $n(p)$ follows the dopant concentration $N_D(N_A)$ up to concentration values of the order of the effective density of states (N_c or N_v , for n- or p-type conduction, respectively). The

effective density of states depends, besides the sample temperature ($\propto T^{3/2}$), on the effective mass of the carrier, e.g. for the conduction band E_c

$$N_c = 2 \left(\frac{2\pi m_0 m_e k_B T}{h^2} \right)^{3/2} \quad (9.50)$$

with m_0 denoting the free electron mass and m_e the effective mass of the electrons; the other constants have their usual meanings. Normally, electron effective masses m_e are smaller than hole effective masses m_h . Thus, the density of states in the conduction band is smaller than in the valance band (for a first very rough orientation take $N_c = 10^{18} \text{ cm}^{-3}$ and $N_v = 10^{19} \text{ cm}^{-3}$ for E_c and E_v , respectively). The free carrier concentration n is regulated by the position of the Fermi level E_F with respect to the band edges E_c and E_v . Although the Fermi distribution [9.49] gives the correct Fermi level and carrier concentration, often Boltzmann's approximation is used for nondegenerate semiconductors ($E_c - E_F > 3k_B T$), again denoted for the electron concentration: $n = N_c \exp[-(E_c - E_F)/(k_B T)]$ (for holes: $p = N_v \exp[(E_v - E_F)/(k_B T)]$). The Fermi level E_F adjusts itself in relation to the band edges to provide overall charge neutrality for the sum of fixed and mobile charges, i.e. for the charge sum of ionized impurities and electron and hole densities (for the n-type semiconductor: $N_D^+ = n - p$). The ionized impurity concentration N_D^+ is given by the Fermi level position with respect to the impurity level energy E_D

$$N_D^+ = N_D \frac{1}{1 + g \exp[-(E_D - E_F)/(k_B T)]} \quad (9.51)$$

with g denoting the ground-state degeneracy of the donor level ($g = 2(4)$ for electrons (holes)), E_D usually is some (ten) meV below the conduction band edge energy. This equation shows that complete ionization can be achieved at Fermi level positions well below E_D , i.e. for doping concentrations below the effective density of states N_c . The charge neutrality equation together with Boltzmann's approximations for the free carrier concentrations and the before mentioned ionization relation for the dopant N_D fixes the Fermi energy and the free carrier concentrations for a given temperature. For incompletely ionized donors, i.e. for lower temperatures (below 100 K) the carrier freeze-out range begins. This means that only a certain percentage of the donor concentration results in free electrons in the conduction band. Thus, also the Hall technique will measure a reduced carrier density towards decreasing temperatures. Fitting the free carrier concentration given by the above

equations to a temperature-resolved Hall measurement, e.g. within a range from 77 up to 400 K, allows the determination of the dopant ionization energy E_D .

Compensation Effects

In semiconductors there may also coexist a smaller amount of the adverse dopant type of opposite charge polarity besides the dominating one which determines the sign of the Hall constant and the conduction type (n- or p-type). This adverse dopant type tends to partially compensate the effectiveness of the major dopant and results in a pronounced temperature behavior of the free charge concentration in excess of that of an uncompensated semiconductor. At normal (room) temperatures, the free carrier concentration is given by $n = N_D - N_A$, while at reduced temperatures, the free carrier concentration diminishes much more pronounced due to the compensation and incomplete ionization of the majority carrier dopant type. The charge neutrality equation is now replaced by $N_D^+ - N_A^- = n - p$. Applying again Boltzmann's approximations for the free carrier concentrations and the noted ionization relation for the dopants N_D and N_A , the free electron concentration in case of a partially compensated n-type semiconductor can be deduced

$$\frac{n}{N_D} = -\frac{1}{2} \left(\frac{n_1}{gN_D} + \frac{N_A}{N_D} \right) + \sqrt{\frac{1}{4} \left(\frac{n_1}{gN_D} + \frac{N_A}{N_D} \right)^2 + \frac{1}{g} \left(1 - \frac{N_A}{N_D} \right) \frac{n_1}{N_D}}, \quad (9.52)$$

with $n_1 = N_c \exp[-(E_c - E_D)/(k_B T)]$. This equation can be related again to a temperature-resolved Hall measurement $n(T)$. The fit allows to determine, besides the donor ionization energy E_D , also the compensation ratio N_A/N_D . In dominating p-type semiconductors, the compensation ratio is defined as $N_D/N_A (< 1)$.

In all cases of compensated semiconductors, the Hall mobility is more or less lower than in the uncompensated cases because the additional ionized impurity scattering effects at the compensating centers lead to reduced mobility values. This effect can be even more pronounced at low temperatures when carrier scattering effects by lattice vibrations are negligible, i. e. when the Hall mobility is only affected by free carrier or ionized impurity scattering. Thus, the maximum mobility values of low-doped semiconductors achievable at e.g. 77 K give invaluable information on the purity of the material.

Hall Mobility and Drift Mobility

Deducing from the Hall effect, the carrier velocity was orientated solely along the y-direction of the constant current fed through the long test sample. In practice, the electrons (or holes) are moving not with a linear translation but they are moving on cycloid-type paths due to the two forces of the electric field in y-direction and to Lorentz's force in x-direction. These cycloid-type curves are interrupted by scattering events of the carriers at lattice vibrations and (ionized) impurities depending on the impurity density. A result of these combined movements of the carriers in x- and y-directions under the combined electrical (E_y) and magnetic (Hall) field (E_H) forces are trajectories, where the carriers feel the crystallographic properties of the semiconductor crystal in both directions x and y. Consequently, the Hall mobilities $\mu_{H,n,p}$ may deviate from the drift mobilities $\mu_{n,p}$. The newly introduced Hall factor $r_{H,n}$ denotes the ratio of $\mu_{H,n}/\mu_n$; in the case of a p-type semiconductor, $r_{H,p}$ denotes the ratio of $\mu_{H,p}/\mu_p$. The Hall factor modifies the formerly Hall constants for an n-type semiconductor $R_{H,n} = -r_{H,n}1/(qn)$ and for the p-type semiconductor $R_{H,p} = -r_{H,p}1/(qp)$. The Hall factors depend slightly on the magnetic field, the crystal structure, and the measurement temperature. For high magnetic fields, the Hall factor tends to unity. In practice, due to often unknown precise values of the Hall factors, a unity value is assumed for material quality comparisons of different epitaxial approaches or annealing conditions.

Field-Effect Mobility (FET Transistor)

In devices like field-effect transistors (FET), the conducting channel is controlled by gate electrode applying an electrical field perpendicular to the current path. The channel can be either located at the surface of the device, like in a MISFET (metal-insulator-semiconductor FET) or the channel may be buried, like in HFET/HEMT (hetero structure/high-electron mobility FET) transistors. For these large variety of devices, the Hall effect can be applied to measure the channel mobility which can be either enhanced by two-dimensional electron gas effects or be reduced due to surface scattering effects between the insulating gate oxide and the surface conducting channel, compared to bulk conduction in thicker epitaxial layers.

9.4.3 Dopant and Carrier Concentration Measurements

The measurement of the dopant and carrier concentration is mainly done by capacitance-voltage (C-V)

analyses because this method delivers not only averaged carrier concentrations but provides the in-depth carrier concentration profiles, too. Capacitance-voltage (C - V) analyses are predominantly executed applying LCR-meters, which can measure the sample's AC conductance besides the capacitance. C - V analyses should be evaluated under the assumption that the loss tangent ($G/\omega C$) of the sample does not exceed some percent proving that the capacitance for a given measurement frequency is dominating the conductance contribution. If sufficiently low values of the loss tangent cannot be achieved for a standard frequency of e.g. 1 MHz, then higher frequencies should be chosen in case of parallel conductance leakage, or lower frequencies should be used in cases of high series resistances of the samples under test. A rule of thumb is to choose the measurement frequency according to the minimum of the loss tangent. If stray capacitances in parallel to the sample are present, then those should be determined by applying adequate test structures and subtracting them before conducting further C - V analyses.

The C - V method can be most simply explained applying a Schottky contact, i.e., a metal contact on an n -type semiconductor. Firstly, the doping profile analysis is explained under the assumption of the depletion approximation. Secondly, some limitations of the C - V method with respect to in-depth resolution limitations due to Debye length effects are discussed. Thirdly, correction procedures are explained for the most important cases of near-surface doping profiles in metal-insulator-semiconductor (MIS) structures and in-depth implantation profiles as well as high-low doping profiles.

Capacitance-Voltage (C - V) Analyses

The basic capacitance-voltage (C - V) evaluation with respect to semiconductor in-depth doping profiling is based on the depletion approximation, i.e. on the assumption of an abrupt space charge edge in conjunction with complete dopant ionization. A suitable sample test structure is shown in Fig. 9.39. A Schottky contact metal with defined area A is evaporated on top of the semiconductor, while ohmic metallization is provided at the back side. Due to the work function difference of the metal to the electron affinity of the semiconductor, a space charge region of depth w is formed. The depth of the space charge region can be controlled by a reverse biased voltage applied to the top gate electrode. Within the depletion approximation, the capacitance of the space charge region (neglecting side wall effects and other stray capacitances) is given by the plate capacitor

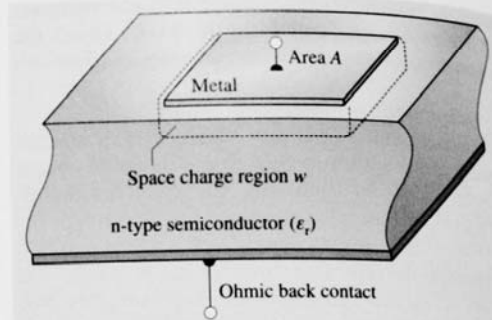


Fig. 9.39 Schottky metal contact (area A) on top of an n -type semiconductor with space charge region depth w

model

$$C_{sc} = \epsilon_0 \epsilon_r \frac{A}{w_0}, \quad (9.53)$$

with ϵ_r being the dielectric constant of the semiconductor, ϵ_0 the vacuum permittivity, and w_0 the space charge width at zero bias. Figure 9.40 shows the related band diagram at zero bias. The Schottky barrier height Φ_{Bn} induces a band bending within the semiconductor of qV_{bi} , with V_{bi} being the built-in voltage of the Schottky diode. E_c , E_v and E_F are the conduction, valence band edges, and the Fermi level, respectively. The Fermi level at equilibrium is constant throughout the whole metal-semiconductor structure indicating the absence of current flow at zero bias conditions. If an external reverse voltage is applied to the left-sided metal electrode, the band bending of the semiconductor increases and the width of the space charge region increases, too. Consequently, the resulting capacitance is reduced, according to (9.53). The depletion approximation model can be seen in Fig. 9.41, where the in-depth free electron

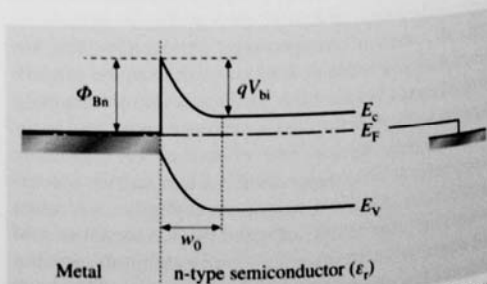


Fig. 9.40 Band diagram of a metal-semiconductor Schottky contact in thermal equilibrium at zero bias

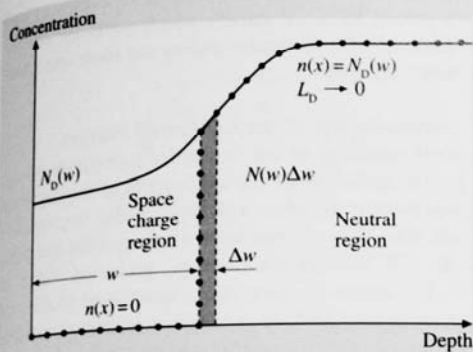


Fig. 9.41 Arbitrary in-depth doping profile $N_D(w)$ and resulting in-depth free electron concentration profile $n(x)$, described according to the depletion approximation

concentration $n(x)$ is shown in idealized form compared to an arbitrarily assumed in-depth doping concentration profile $N_D(w)$. In the neutral region, the free carriers (here electrons) compensate the ionized donor atoms [$N_D^+(w) = N_D(w) = n(x)$]. Depletion approximation means that the free carrier concentration at the edge of the space charge region makes an abrupt transition down towards zero concentration inside the space charge region. This corresponds to a zero Debye length. The Debye length $L_D = \sqrt{\epsilon_0 \epsilon_r k_B T / (q^2 n)}$ denotes a typical screening length depending on the square root of temperature T compensating space charge distortions from thermal equilibrium of the carrier concentration n .

By solving Poisson's equation $\text{div } \mathbf{D} = \rho$ and integrating twice over the space charge region, the total band bending potential V depending on the space charge region depth w , can be deduced: $V = \frac{1}{2} q N_D w^2 / (\epsilon_0 \epsilon_r)$ (so far a constant dopant profile N_D is assumed). By combining this equation with the plate capacitor equation, solving for an expression of $1/C^2(V)$ and differentiating $1/C^2(V)$ versus the external voltage, an expression for a nonconstant in-depth carrier concentration profile $n(x)$ (identified equal to $N_D(x)$) due to the depletion approximation can be found

$$N_D(x) = \frac{1}{q \epsilon_0 \epsilon_r} \frac{1}{A^2} \frac{C^3(V)}{dC(V)/dV} \quad \text{for an n-type semiconductor,} \quad (9.54)$$

$$N_A(x) = -\frac{1}{q \epsilon_0 \epsilon_r} \frac{1}{A^2} \frac{C^3(V)}{dC(V)/dV} \quad \text{for a p-type semiconductor.} \quad (9.55)$$

In both cases, the depth x is calculated from the plate capacitor model $x = \epsilon_0 \epsilon_r A / C(V)$.

The accuracy of the C - V method is mainly determined by the known accuracy of the gate electrode area, e.g. an accuracy of the area A within 1% gives an accuracy of the doping profile of 2%. Further, the spatial variation of the doping profile should be small within a Debye length to assure the validity of local charge neutrality during in-depth profiling.

Limitations on C - V Analyses,

Applying the Depletion Approximation

The in-depth resolution of doping profiles determined by the C - V profiling method is limited by the Debye length. The finite Debye length leads to a smear out of the abrupt space charge edge over roughly 2–3 Debye lengths. This phenomenon is shown in Fig. 9.42. Two effects may result: first, in the case of abrupt steps within the doping profile, the equilibrium carrier profile will not follow the doping step with the same abruptness (local neutrality is not fulfilled); second, in the case of near-surface profiling, the free carrier tail of the space charge edge will touch the interface region even if a certain space charge region is still opened. In both cases profiling errors will arise. In the first case, the abruptness of real doping profiles cannot be measured adequately; in the second case the apparent carrier profile (from which the user concludes the doping profile) will increase artificially towards the interface when the space charge region is smaller than about two Debye lengths.

The Debye length can be reduced by lowering the measurement temperature ($L_D \sim \sqrt{T}$), but for very low

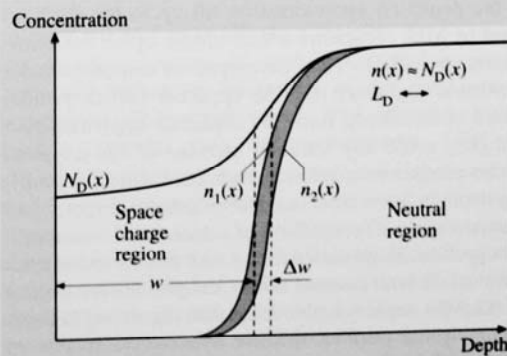


Fig. 9.42 Arbitrary in-depth doping profile $N_D(x)$ and more realistic in-depth free electron concentration profile $n(x)$ in presence of Debye length smearing of the space charge edge

temperatures, the dopant ionization is diminished, too. Thus, the measured carrier concentration would underestimate the true dopant concentration and this approach was limited to very shallow donor levels.

These further aspects of finite Debye length problems during doping profiling will be discussed in the next section.

Debye Length Corrections for Near-Surface Doping Profiles in MOS/MIS Structures and for Ion-Implanted In-Depth Profiles

In this section two correction procedures will be described which help to improve approximations of the true doping profiles while the apparent $C-V$ (carrier) profiles are affected by Debye length broadening effects.

Near-Surface Doping Profiles in MOS Structures
MOS (metal-oxide-semiconductor) or MIS (metal-insulator-semiconductor) structures play an important role in all CMOS based devices, like CMOS transistors or (B)CCD ((buried) charge-coupled device) focal plane arrays. The surface doping profile, i.e. the doping profile in the direct vicinity of the dielectric-semiconductor interface needs to be known very accurately because the value and homogeneity of the threshold voltage depends on it. MIS structures isolate quite well any current flow due to the high specific resistivity of the dielectric/oxide. This allows to solve Poisson's equation while neglecting any current flow and to consider the additional contribution of mobile carriers in the space charge region [9.50]. By applying this analytical approach Ziegler et al. [9.50] extended the range of the depletion approximation till up to the flatband point of MIS capacitors which means up to the semiconductor surface. They developed an analytic tabular correction algorithm for the apparent carrier profile, which is calculated from the depletion approximation and they avoid any artificial increase of the apparent carrier profile towards the surface, even when the profiling depth is lower than two Debye lengths. Figure 9.43 shows a typical comparison of uncorrected concentration profiles (dash-dotted lines) with the corrected ones (circles). In both cases of boron and phosphorus doping of the MIS capacitor, the correction algorithm delivers relatively flat profiles. Without this correction pile-up effects of the dopants were assumed due to annealing and segregation effects. The precise determination of the flatband point and the surface inversion point were greatly improved by applying the Ziegler-Klausmann-Kar profile correction [9.50]. The method is applicable

for quasi-static RF measured MIS $C-V$ curves as well as to pulsed RF $C-V$ curves which avoid the surface inversion of MIS structures during the short (ms) measurement windows.

Measurement of Ion Implanted Profiles

In-depth profiling of ion implanted semiconductors is a special challenge for the application of the depletion approximation because a Gaussian-like implantation profile has more or less steep edges around the maximum, i.e. around the average projected range of deposited atoms. Furthermore, implantation profiles are used, compared to diffusion doping profiles, to achieve more abrupt doping transitions when scaling devices or to achieve low-ohmic contacts. Thus, the steepness of profile edges may occur easily within a Debye length, especially for lower implantation doses.

The discussed correction algorithm of Ziegler et al. [9.50] cannot be applied for smaller depth than two Debye lengths. For larger depths this algorithm exhibits

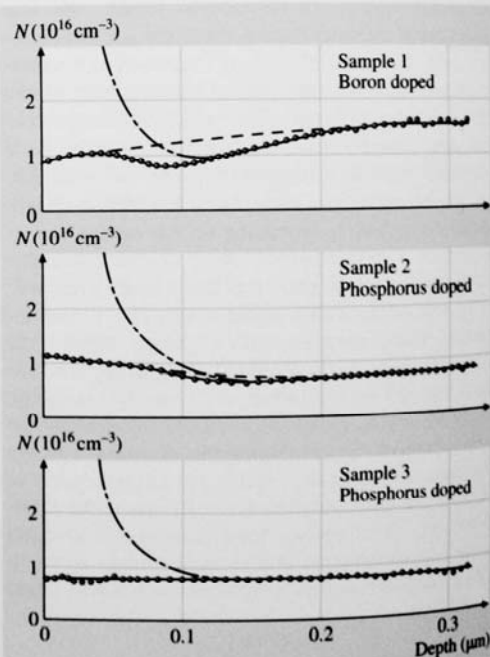


Fig. 9.43 Examples for doping profiles in silicon MIS capacitors. The steeply uprising curves show the apparent doping profiles using the uncorrected depletion approximation; the circles show the Debye-length corrected measurements (after [9.50])

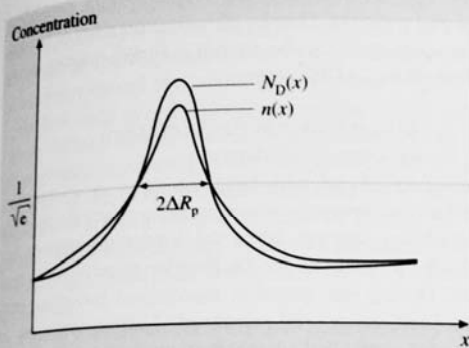


Fig. 9.44 In-depth profiles of implanted dopants $N_D(x)$ and free carrier concentration $n(x)$: near the peak is $N_D(x) > n(x)$ and far away from the peak is $n(x) > N_D(x)$

a smooth transition into the standard depletion approximation. Quite a lot of implanted profiles show their projected ranges are quite deeper than several Debye lengths.

The same problem arises during profiling of high-low or low-high doping transitions of the same doping type, e.g. in varactor diodes. In all these cases, local charge neutrality is not fulfilled, especially in the vicinity of the steepest doping gradient. This typical situation is explained in Fig. 9.44 using the example of an implantation profile $N_D(x)$ with a Gaussian-like shape of its edges. The mobile carrier concentration $n(x)$ deviates typically from the dopant distribution due to spreading diffusion effects and repelling electrical field forces, i.e. at the maximum, free carriers are missing and in the edges the mobile carriers produce longer tails of the apparent concentration. This can be proved by comparing SIMS (secondary ion mass spectroscopy) measured implantation profiles with their $C-V$ evaluated counterparts. The $C-V$ technique is based on the signal from the mobile carriers ($C = dQ/dV$), thus the apparent doping profile lacks the abruptness of the real profile. Unfortunately SIMS cannot replace the $C-V$ evaluation because SIMS cannot measure the electrically active concentration which is relevant for the device function. It determines only the atom concentration without information with respect to electrical activation. Thus, an effort is needed to improve the $C-V$ evaluation in these applications. This improvement was done by Kennedy et al. [9.51, 52]. They developed a correction of the apparent depletion approximation profiles assuming that the free carrier concentration is known. Therefore, they solved Poisson's equation considering

additionally the charge contributions of the majority carriers and neglecting current flow in the reverse direction of Schottky- or pn-junction contacts. They deduced (9.56) which extracts the dopant profile $N_D(x)$ from the mobile carrier profile $n(x)$

$$N(x) = n(x) - \frac{\epsilon_0 \epsilon_r kT}{q^2} \frac{d}{dx} \left(\frac{1}{n(x)} \frac{dn(x)}{dx} \right), \quad (9.56)$$

where $n(x)$ is obtained by evaluation of the standard depletion approximation (9.54), (9.55) evaluation from a $C-V$ measurement. This extraction is valid if the true mobile carrier profile would be known exactly. Unfortunately, the $C-V$ measurement determines only an approximation to this true mobile carrier profile because the space charge edge is smeared out over about two Debye lengths. Thus, the Kennedy correction [9.51, 52] is a useful improvement to obtain a more realistic shape of implanted profiles but it cannot, in principle, provide the true physical profile again caused by Debye length reasons. A good rule of thumb in case of implanted profiles, not to be affected too much by Debye length distortions (error $< 1\%$), is the relation $\Delta R_p \geq 10L_D$, with ΔR_p being the half width of the implanted profile and L_D the Debye length for a given doping. This means in practice that high-dose implanted profiles suffer much less from Debye length distortions applying the $C-V$ technique.

Applying (9.56) for the improvement of step-like high-low doping profiles, it is recommended (if possible) to provide the depletion from the highly doped side because the Debye length is shorter at the begin of the measurement which helps the accuracy of the profile reconstruction [9.53].

Electron and Hole Effective Masses

The effective masses of mobile carriers in semiconductors reflect the curvatures of the band structure in the $E(k)$ diagrammes. The effective mass is of a tensorial type with components: $1/m_{ij}^* \equiv 1/(h/2\pi)^2 [\partial^2 E(k)/(\partial k_i \partial k_j)]$ with E denoting the band energy and k ($= 2\pi/\lambda$) the wavevector of the carrier related to its momentum $p = (h/2\pi)k$. The band structure of semiconductors is described by Schrödinger's equation which is based on the wave nature of electron propagation in crystals. Tabulated values of effective masses of common semiconductors can be found in [9.49]. Effective masses can be measured by cyclotron resonance and by angle-resolved photoemission spectroscopy (ARPES) [9.54]. III-V semiconductors with their low effective electron masses (≈ 0.07) provide high carrier velocities within short acceleration

times and thus a very high speed potential of electronic circuits.

9.4.4 I - V Breakdown Mechanisms

Electrical breakdown in semiconductors is characterized in terms of the electrical field strength (unit kV/cm) in regions of the I - V curve, where the current increases to a much higher extent than for slightly reduced field strength below. Electrical breakdown, indicated by a steep current increase versus voltage, is mainly related to two mechanisms: impact ionization (avalanche) breakdown and tunneling (internal field emission). Both mechanisms can be distinguished by investigating the temperature behavior of the current-voltage (I - V) curves. For a certain constant voltage in the breakdown region a positive temperature coefficient of the current is indicative for tunneling breakdown, while a negative temperature coefficient indicates impact ionization breakdown. Both mechanisms are discussed in more detail in the following two subsections.

Impact Ionization Breakdown Field Strength

Impact ionization is a bulk controlled current flow mechanism induced by a carrier multiplying band-band process. Carriers are accelerated by an high electrical field, that they can induce electron-hole pair ionization due to their high energy. The resulting additional electrons and holes are accelerated in opposite directions, until they gain and overcome their specific ionizing energy ($\gg kT$); thus, the whole process produces an avalanche-like increase of the current after an only small voltage increase. Impact ionization breakdown can be concluded from a negative temperature coefficient of the current at a high fixed reverse voltage. Increasing temperature causes more lattice vibrations, which hinder carriers, to gain directed acceleration; thus higher electrical fields are needed at elevated temperatures, to produce the same current. Small effective masses ease the ionization process due to higher carrier mobility in the accelerating field. Impact ionization is a band-band pair generation process, thus the breakdown electric field strength increases with increasing bandgap of the semiconductor. The avalanche process is described by the ionization rates α_n and α_h (unit 1/cm) for electron or hole induced electron-hole pairs, respectively. The ionization rates $\alpha_{n,h}$ depend largely on the electrical field strength E

$$\alpha(E) = \alpha_{\infty} e^{[-(E_0/E)^m]} \quad (9.57)$$

with α_{∞} , E_0 , and m being a temperature dependent material constant. Graphs of ionization rates of several semiconductors can be found in [9.49] ranging up to values of $\alpha_{n,h}$ of $10^5/\text{cm}$.

Tunneling (Internal Field Emission) Breakdown Field Strength

Tunneling or internal field emission is a quantum mechanical process, where carriers penetrate through thin energy barriers when the barrier thicknesses approach the value of the de Broglie wavelength (a few nm). During the quantum mechanical tunneling process their energy is conserved. Carrier tunneling is a barrier-controlled current flow mechanism. Tunneling is observed in highly doped pn junctions, where narrow barriers are favored by the high doping and the resulting small space charge regions. The de Broglie wavelength $\lambda_{e,h}$ is given by

$$\lambda_{e,h} = \frac{h}{\sqrt{2 * m_0 m_{e,h} E}} \quad (9.58)$$

with m_0 denoting the free electron mass, $m_{e,h}$ the effective mass of electrons or holes, and E the energy of the carrier. For, e.g. InP with an electron effective mass of 0.07 and an electron energy of kT ($T = 300\text{ K}$) λ_e amounts to 29 nm, while for $E = 1\text{ eV}$, λ_e reduces to 4.64 nm.

The barrier to be penetrated by the carrier should be narrower than de Broglie's wavelength for the relevant carrier's energy. The probability for tunneling increases considerably for electrical field strength in the range of 10^6 V/cm , i. e. 1 (e)V/10 nm, where the effective barrier width for band-band tunneling is reduced to 10 nm, being in the range of the aforementioned de Broglie wavelength. For this nonthermal process, the thermal energy of the carrier (electron) is most often neglected.

Temperature Dependent Reverse Current I - V Analysis

According to the explanations given in the two subsections before, the dominating mechanism for breakdown in pn-diodes or transistors can be identified by measuring the reverse I - V characteristics for various temperatures. A recommended temperature range extends, e.g. from 0 to 80 °C in steps of 20 °C, which can be controlled by Peltier cooling or heating. Much wider temperature ranges can be achieved in cryostats, where electrical heating in conjunction with liquid nitrogen cooling can provide a temperature range between 77 and 420 K. Because generation currents in pn-junctions are increasing proportional to the intrinsic concentration

n_i , which itself increases exponentially over temperature in half of a given bandgap; an even moderate temperature spacing within a set of I - V curves results in a current spread over about two orders of magnitude in the low-field generation current regime. The current increases quite moderately with the square root of the voltage. At the onset of either tunneling or avalanche breakdown a much steeper increase of current is observed. The following two figures of pn-diodes show typical characteristics of either tunneling or avalanche breakdown.

Figure 9.45 shows for a GaInAs homojunction photodiode the typical band-band tunneling behavior for voltages above of 15 V, where the remaining temperature dependence stems from the decreasing bandgap with increasing temperature. Thus, a positive temperature coefficient of the current for fixed voltage is present in the tunneling region. Typical at the onset of tunneling is a pronounced reduction of the temperature sensitivity at the transition from the generation regime below 15 V to the tunneling regime above 15 V.

Figure 9.46 presents the typical reverse current characteristics of a silicon p^+n diode [9.56] dominated by avalanche breakdown above 27 V. Again, in the lower field regime, the I - V characteristics show typical Shockley-Read-Hall generation behavior exhibiting a pronounced temperature sensitivity according to the higher bandgap of silicon (compared to Fig. 9.45) comprising a GaInAs photodiode. The onset of impact ionization is characterized by a much steeper increase of the current versus voltage compared to the tunneling breakdown in Fig. 9.45. Furthermore, the temperature coefficient is reversed compared to the tunneling case before. In the impact ionization regime, a higher voltage is needed for constant current with higher temperature, due to increasing lattice vibrations which hinder the electrons from being accelerated due to a higher collision rate. Thus, the I - V characteristics exhibit a typical crossing behavior when the generation regime is taken over by impact ionization.

In conclusion, the temperature resolved I - V characteristics can clearly distinguish between generation, tunneling and impact ionization regimes.

9.4.5 Deep Level Characterization and Minority Carrier Lifetime

Deep levels in semiconductors heavily affect the forward and reverse current curves they increase the noise in photodiodes and transistors, reduce the minority

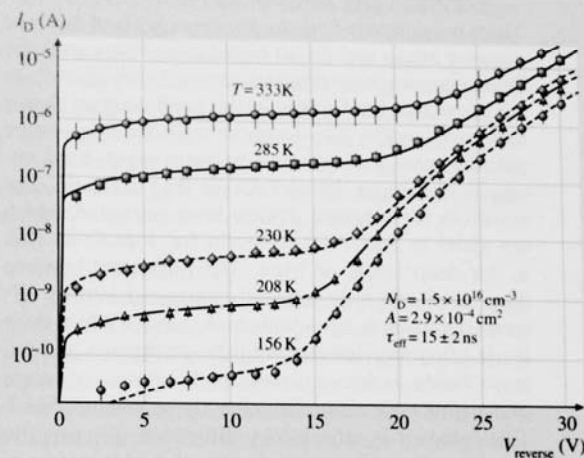


Fig. 9.45 Dark current of a GaInAs homojunction photodiode (after [9.55]) dominated by tunneling breakdown above 15 V

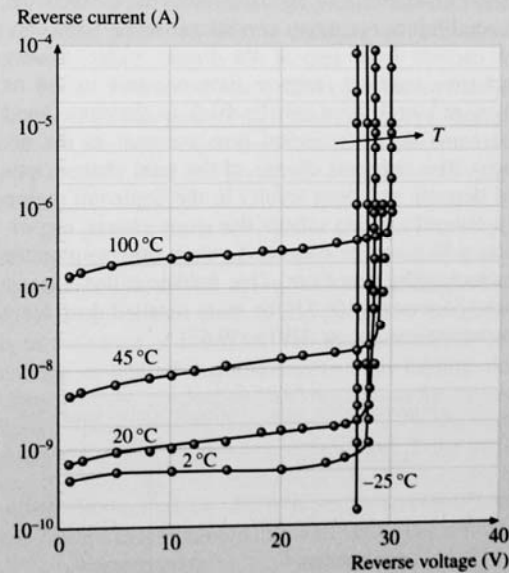


Fig. 9.46 Reverse current of a silicon p^+n diode (after [9.56]), dominated by avalanche breakdown above 27 V

carrier lifetime, or quench the storage time in charge-coupled devices or CMOS focal plane arrays. One of the most sensitive methods to determine a comprehensive set of deep level or trap parameters is the DLTS (deep level transient spectroscopy) technique.

Definition and Role of Trap Parameters

There is a common basis for the description of donor or acceptor states and the so called deep levels or traps. Donor or acceptor states are situated very closely to the respective band edges in the band diagram (some tens meV), while deep levels or traps have an energy position more or less close to the midgap band energy, i.e. they are located deeper than 200 meV. The equations for deep and shallow level ionization, which are given in Sect. 9.4.2 are valid for dopants as well as for deep levels or traps. The difference between deep levels and traps is mainly attributed to their different interaction rates with both bands. While deep levels often may interact with the conduction and valence bands with comparable probabilities, traps are exchanging their carriers dominantly on with one band. This behavior is reflected by differences in energetic positions: deep levels are close to the midgap energy while traps are located near to one of the bands, but considerably deeper than shallow donors or acceptors. Thus, deep levels often function as recombination centers to extract electrons and holes from the bands under nonequilibrium excitation conditions, while traps capture carriers from one of the bands within a very short time constant (capture time constant in the ns range) and emit these carriers back to the same band after some delay (emission time constant in the ms range). The temporal change of the total charge (ionized dopants and deep levels) in the depletion region of a Schottky diode affects the space charge capacitance, which can be measured versus time to monitor trap recharging processes. This field is called capacitance spectroscopy [9.57], or more detailed deep level transient spectroscopy (DLTS) [9.58].

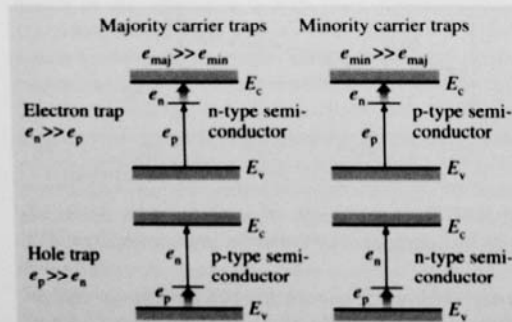


Fig. 9.47 Energetic location and main interactions of majority carrier traps and minority carrier traps in n- and p-type semiconductors

Figure 9.47 shows the principal possibilities for locating traps in the band diagrams of n- and p-type semiconductors. The thick arrows indicate the dominant interaction paths. If a trap is located much closer to the conduction band than to the valence band (see the electron traps in the upper parts of Fig. 9.47), then their electron emission rates e_n (unit s^{-1}) are considerably larger than their hole emission rates e_p (unit s^{-1}). This situation reverses for hole traps located near to the valence band. A trap interacting dominantly with the majority (minority) carrier band is called a majority (minority) carrier trap. A trap interacting dominantly with the conduction (valence) band is called an electron (hole) trap.

Traps are characterized by several parameters. The first is the concentration N_T (unit cm^{-3}), the second is the energetic distance from the corresponding energy band edge $E_c - E_T$ ($E_T - E_v$) (unit eV). The capture of carriers represented by the capture rates c_n, c_p (unit s^{-1}) into traps from the bands is normally a very fast process, the time constant of which is in the ns range

$$c_n = \sigma_n v_{th} n \quad \text{and} \quad c_p = \sigma_p v_{th} p, \quad (9.59)$$

with σ_n, σ_p denoting the capture cross sections (unit cm^2 , for orientation purposes $10^{-15} cm^2$), v_{th} denoting the carrier thermal velocity ($10^7 cm/s$) and n, p the carrier concentrations in the corresponding bands. After the capture process the subsequent emission rate e_n (unit s^{-1}) is driven exponentially by the trap activation energy $E_c - E_T$ given here for an electron trap

$$e_n = \sigma_n v_{th} N_c g \exp\left(-\frac{E_c - E_T}{k_B T}\right). \quad (9.60)$$

Equation (9.60) is the basis for the Arrhenius plot which allows the extraction of the trap activation energy by plotting $\log(e_n/T^2)$ versus $1000/T$ (Fig. 9.48). The prefactor T^2 stems from the joined temperature behavior of the effective density of states N_c in conjunction with the thermal velocity v_{th} .

The minority carrier lifetime τ_{eff} (s) can be deduced from the generation rate U ($cm^{-3}s^{-1}$) from the trap parameters according to the theory of Shockley, Read, and Hall [9.59, 60].

$$\tau_{eff} = \frac{n_i}{U} \quad (9.61)$$

with n_i denoting the intrinsic carrier concentration of the semiconductor material [9.49] and

$$U = \frac{\sigma_p \sigma_n v_{th} N_T}{\sigma_n \exp\left(\frac{E_{trap}}{k_B T}\right) + \sigma_p \exp\left(-\frac{E_{trap}}{k_B T}\right)} n_i. \quad (9.62)$$

Here, E_{trap} is the trap energy position with respect to the intrinsic energy E_i ($E_i \approx (E_c + E_v)/2$) of the semi-

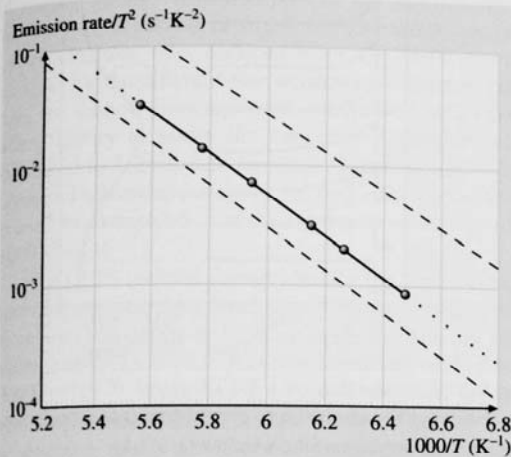


Fig. 9.48 Arrhenius plot of the DLTS spectrum in Fig. 9.49 for Au in n-type silicon; the measurement is shown as *full line*, the *dashed lines* represent comparison data from a trap library to assess the measured Arrhenius data compared to known data for easier identification. The measured activation energy is 340 meV. The *dotted line* is used for extrapolation of the capture cross section for $1000/T \rightarrow 0$

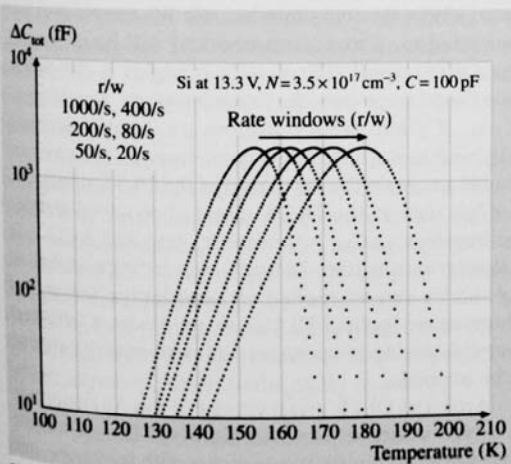


Fig. 9.49 DLTS measurement of the Au trap in n-type silicon doped with $3.5 \times 10^{17} \text{ cm}^{-3}$, reverse pulse: 13.3 V. The rate windows *rw* are from *left to right*: 20/s, 50/s, 80/s, 200/s, 400/s, and 1000/s. The depletion capacitance is 100 pF

conductor. It can be seen from this equation that deep levels near midgap are most effective for generation and recombination because they lead to the largest generation or recombination rates U and thus give the lowest minority carrier lifetime according to (9.61). Thus, it is an important task of semiconductor materials quality assessment to determine the trap parameters N_T , E_T (respectively E_{trap}), σ_n , and σ_p to deduce all further generation and recombination statistics.

The DLTS Technique

The DLTS technique is based upon repetitive pulsing the bias of a Schottky diode or pn-diode from slight forward bias conditions (short pulse, some μs) into deep depletion for a considerably longer time (ms to s) and observe the resulting capacitance transient which stems from the charging and emptying of traps. During these repetitive measurements which also allow averaging of the mostly relatively small capacitance transients, the measurement temperature of the sample is varied over a large range, e.g. from 77 to 400 K. The development of this temperature dependent capacitance transient which is directly indicative for trap charging and emission is shown in more detail in this section.

Figure 9.50 shows the typical capacitance transient for the emission phase 3 of a majority carrier trap, i.e. a donor-like trap which is neutral in the electron occupied or filled state and positively charged in the empty state.

The process starts after phase (1), the empty (positively charged) state of all traps in reverse bias of the sample (not shown in Fig. 9.50, this corresponds to $C(t) \rightarrow \infty$), with a short filling pulse at $t < 0$, which is in the range of some μs . The time period 2 is long enough so that all majority carrier traps capture electrons from the conduction band because in the forward biased filling phase all traps are pulsed below the Fermi energy E_F . The traps are now neutrally filled at the end of phase (2). The emission phase (3) is started by pulsing the sample into deep depletion and the capacitance drops to a minimum $C(t=0) = C_0$. The resulting

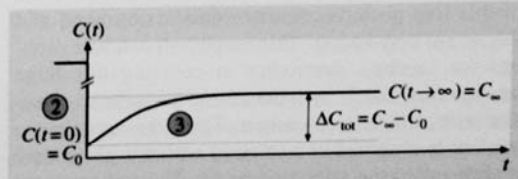


Fig. 9.50 Transient capacitance during majority carrier emission (3) after trap filling phase (2) of a donor-like trap

space charge depth is given by the bias voltage and the depleted donor charge of the shallow doping level. The traps are neutral at the beginning of the emission phase (3) and thus they do not contribute to the depleted space charge. Due to the high reverse bias V_r in phase (3) all traps are pushed above the Fermi energy and they are switched to emission. The capacitance transient $C(t)$ in the emission phase can be calculated with (9.63)

$$C(t) = A \sqrt{\frac{q\epsilon_0\epsilon_r}{2(V_{bi} + V_r)}} \left\{ N_D^+ + N_T \left[1 - \exp(-e_n t) \right] \right\} \quad (9.63)$$

with A denoting the area of the Schottky diode and V_{bi} representing the built-in voltage of the test diode. Towards the end of the emission phase (3) all traps are empty, i. e. after loosing their electrons to the conduction band, the traps now contribute to the space charge of the shallow donors $N_D^{(+)}$ with concentration $N_T^{(+)}$. The transient capacitance thus changes by an amount $\Delta C_{tot} = C_\infty - C_0$. From the amplitude ΔC_{tot} of this transient, the trap concentration N_T can be deduced. For large trap concentrations and thus large capacitance transients, it may be practical to fit (9.63) with a transient capacitance measurement to extract the trap concentration. In practice, this direct way is difficult when the trap concentration falls below the shallow doping level by orders of magnitude. The transient will be buried within the noise of the measurement. In 1974 Lang published a procedure to detect very small capacitance transients out of the noise even when the trap concentration falls by 4–5 orders of magnitude below the shallow doping level: the DLTS technique [9.58].

Two aspects are important. First, according to the DLTS technique, the biasing sequence between filling (slight forward direction) and emptying (reverse voltage V_r) of the traps is applied repeatedly to the sample, thus averaging of the transient can be reached. Second, due to (9.60), the emission rate covers a very large range of more than 10 orders of magnitude if all possible trap positions between conduction band and midgap are considered. This implies too much problems for standard electronics in covering this large emission time range to measure the capacitance transient with sufficient resolution. Thus, the capacitance transient is observed by sampling within a given time window called the rate window rw . The measurement temperature is scanned such that the maximum of the transient amplitude can be easily observed for any given

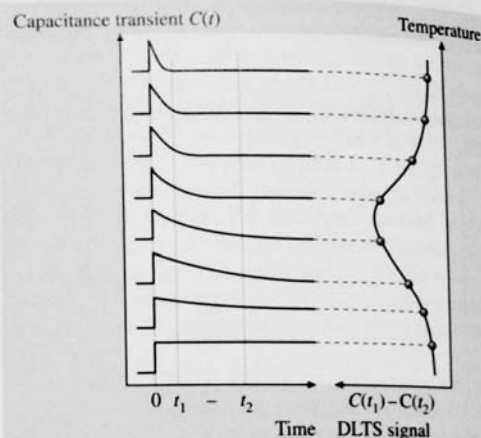


Fig. 9.51 Construction of a DLTS signal $(C(t_1) - C(t_2))$ by observing the temperature dependent transient capacitance within an observation time window $(t_2 - t_1)$

rate window rw . Figure 9.51 elucidates the principle of Lang's DLTS technique. For deep temperatures, the emission process is very slow, thus the capacitance stays practically constant over the observation time window $t_2 - t_1$. For high temperatures, the transient has occurred completely even before the first sampling time t_1 , thus the observed capacitance difference over $t_2 - t_1$ is again a constant. For a certain intermediate temperature, where the trap emission rate fits the observation time window, a maximum transient will be measured. The DLTS signal $(C(t_1) - C(t_2))$ (right) is the difference capacitance over the rate window rw , according to $t_2 - t_1$. If a trap is very shallow, i. e. located energetically near to the band edge, quite deep temperatures are needed to obtain the maximum of the DLTS signal.

The sign of the DLTS signal allows to determine the trap type, $\Delta C_{tot} > 0$: majority trap and $\Delta C_{tot} < 0$: minority carrier trap. Minority carrier traps in Schottky diodes can be excited by applying pulsed optical illumination (optical DLTS); in pn-diodes a sufficient forward biasing is necessary to inject minority carrier, to be trapped.

A typical DLTS measurement of the Au donor trap in n-type silicon is shown in Fig. 9.49. The shift of the DLTS peak to higher temperatures with increasing rate window can be observed i. e. the emission rate increases with increasing temperature. The trap concentration can be determined from the amplitude of the DLTS signal. For extracting the trap activation energy, the emission rates need to be plotted in an Arrhenius plot over the in-

verse of the temperature $1000/T$. From the same plot, the capture cross section for $T \rightarrow \infty$ can be extracted by extrapolating the emission rate for $1000/T \rightarrow 0$. A corresponding Arrhenius plot of the measurement in Fig. 9.49 is shown in Fig. 9.48. The measurement of the emission rate, deduced from the DLTS signal maxima for the different rate windows is shown in full line, the dashed lines represent comparison data from a trap library to assess the measured Arrhenius data compared to known data for easier identification. The measured activation energy is 340 meV. The dotted line is used for extrapolation of the capture cross section for $1000/T \rightarrow 0$.

The DLTS method cannot identify the physical nature of a trap or a deep level, e.g. if the level originates from a crystal defect or from an impurity. The big advantage of DLTS is its impressive sensitivity of N_T/N_D down to 10^{-6} , unsurpassed by other physical analyses. Trap concentrations as low as $< 10^{10} \text{ cm}^{-3}$ can be detected, this is 13 orders of magnitude below the crystals atomic concentration. Therefore electronic averaging of the sampled small capacitance transients applying boxcar or lock-in techniques are necessary. DLTS delivers fingerprints of deep levels, which should be compared to trap libraries of known defects, concerning activation energy and capture cross section. DLTS is spectroscopic, because traps with different activation energies appear with their maxima at different temperatures. If the spectra of two traps are overlapping, subtraction methods can be applied by simulating and approximating the DLTS maxima by Gaussian curves with different slopes and subtracting the leading peak from the rest of the spectrum until all traps have been identified.

A lot of extensions of the DLTS technique have been published. One important evaluation is the determination of the temperature dependence of the capture cross section of a deep level [9.61], having in mind that the standard DLTS technique allows only to measure the extrapolated capture cross section for $T \rightarrow \infty$. The method of Partin et al. is based on varying the width of the filling pulse to very short times until the traps cannot capture anymore carriers in the filling phase.

The Surface Recombination Velocity

Mesa diodes and also planar pn-diodes sometimes suffer from additional leakage currents across the surface or perimeter of the sample. Thus analyses of the bulk or currents are impeded by surface currents, which are induced by additional surface recombination. The surface recombination is described by the surface recombination

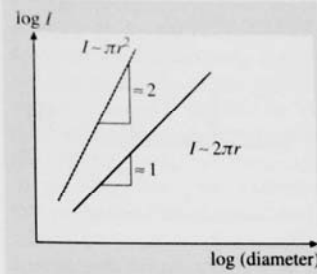


Fig. 9.52 Measured current of a test diode in double logarithmic plot versus diode diameter

velocity S_0 (cm/s). Surface recombination or generation occurs during nonequilibrium conditions, e.g. under reverse bias of a pn-junction. A surface recombination current j_s (A/cm^2) is directed perpendicular to the semiconductor surface

$$j_s = -qS_0\Delta n, \quad (9.64)$$

Δn is the deviation of the carriers from the equilibrium value. The surface recombination velocity S_0 can be expressed by surface state parameters, like the capture cross section of the surface state σ_0 (cm^2) and the concentration N_{st} (cm^{-2}).

$$S_0 = \sigma_0 v_{th} N_{st}. \quad (9.65)$$

To identify whether a measured current of a test sample is dominated by bulk or by surface conduction, a double logarithmic plot of the current versus the diameter of the samples under test is helpful (Fig. 9.52). If the current increases linearly with the diameter, then surface recombination is dominant. If the current increases quadratically with the diameter, bulk conduction is dominant.

Bulk conduction should be proved before current conduction mechanisms or parameters are extracted from I - V measurements, like Schottky barriers, ideality factors, Shockley-Read-Hall trap parameters, or reverse current analyses are done with respect to tunneling or impact ionization.

9.4.6 Contact Resistances of Metal-Semiconductor Contacts

Ohmic contacts at semiconductor devices are mandatory to connect the inner active regions to the outside circuitry or other devices. Ideal ohmic contacts may be described by several views of physicists or engineers on the idealization of the tasks of ohmic contacts, i.e. ohmic contacts should provide

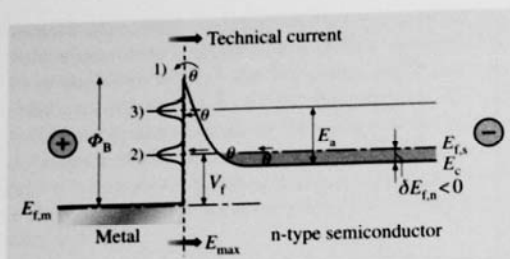


Fig. 9.53 Band diagram of a highly doped, degenerated metal–semiconductor contact under forward bias conditions (metal is positive with respect to the grounded n-type semiconductor)

- a bipolar linear I – V characteristics,
- an unlimited high recombination rate for minority carriers,
- negligible voltage decay compared to that of the active regions,
- no minority carrier injection.

Basic work on the description and technology of ohmic contacts to semiconductors can be found in [9.62, 63]. The main current conduction mechanisms in ohmic contacts are elucidated in Fig. 9.53. A metal is evaporated onto an n-type semiconductor. The work function difference to the electron affinity of the n-type semiconductor should be well chosen to induce at best either an accumulation region at the semiconductor side or at least a small barrier height Φ_B . This has to be surmounted or penetrated by electrons from the semiconductor, e.g. here under forward biasing conditions. A more or less small barrier is a usual case for a lot of metals to semiconductors. If the barrier cannot be avoided principally, it should be only a small obstacle to be surmounted or penetrated. Three current conduction mechanisms should be mentioned here which help electrons to cross the interface into the metal.

1. Thermal emission: electrons have to surmount the barrier $V_{bi} (\approx \Phi_B)$ which is only possible for a few electrons with enough energy compared to the thermal energy kT . Consequently, thermal emission results into bad ohmic contacts. Mostly, these contacts exhibit rectifying characteristics at room temperature. Thermal emission is favored exponentially at high temperatures (thermal process).
2. Field emission or tunneling: this quantum mechanical process allows electrons, due to their wave-like nature, to penetrate the barrier without energy loss if the barrier width is small compared to the de

Broglie wavelength (9.58). This process is likely at very high degenerate doping levels ($\gg 10^{18} \text{ cm}^{-3}$) which induce very narrow space charge regions ($< 10 \text{ nm}$) and consequently very narrow tunneling barrier widths. This process is nearly temperature independent and useful even at very low temperatures because no thermal activation is needed for quantum mechanical tunneling.

3. Thermal field emission or thermally activated tunneling: A certain part of the electrons are thermally activated to penetrate the barrier at an enhanced energy position by tunneling but below the peak of the barrier.

Both current conduction mechanisms 1. and 3. contribute in series to the conduction over the barrier. Compared to the aforementioned processes the electrons see a smaller and narrower barrier. This mechanism is likely for intermediate doping levels.

Figure 9.54 depicts the behavior of the contact resistance of different metals on n-type silicon versus the silicon doping level [9.63]. The contact resistance ($\Omega \text{ cm}^2$) strongly decreases with increasing doping level when thermionic conduction is taken over by tunneling or field emission.

Technically useful contact resistances should be below $10^{-5} \Omega \text{ cm}^2$. Thus, doping levels in excess of 10^{19} cm^{-3} are needed here to guarantee clear predominance of tunneling over thermionic emission. Values of contact resistances lower than $10^{-7} \Omega \text{ cm}^2$ are achievable today.

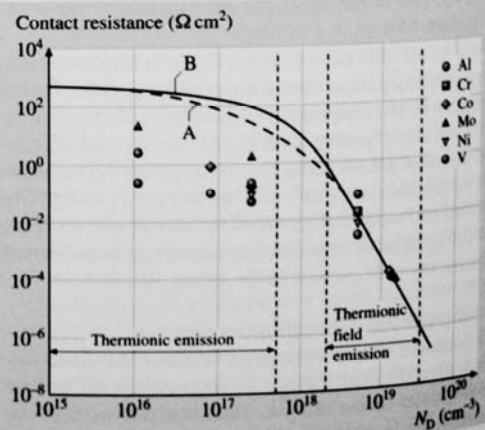


Fig. 9.54 Contact resistance of various metals on n-type silicon depending on doping N_D (after [9.18])

The more exactly termed specific contact resistance $R_{c, \text{spec.}}$ ($\Omega \text{ cm}^2$) is solely the contact resistance in the interface between metal and semiconductor, while the (total) contact resistance R_c (Ω) comprises additional contributions of the spreading resistance of the semiconductor which is depending on the current field lines and thus on the geometry of the ohmic contact: distinguish contacts with vertical current spreading (e.g. top contacts to lasers or emitter contacts to bipolar transistors) and contacts with lateral current spreading (e.g. base contacts in bipolar transistors or source/drain contacts to field-effect transistors). The latter contact type exhibits a strong inhomogeneous current density over the contact length compared to the former contact type, which has a better homogeneous current distribution over its contact area.

Measurement techniques for contact resistances may be attributed to the aforementioned contact geometry. They should allow to extract the (low) specific contact resistance from the (somewhat higher) total contact resistance to provide information for optimizing the contact resistance, e.g. by annealing procedures.

Measurements on ohmic contacts should be done applying a Kelvin contact configuration which means to feed a constant current via two terminals (needles) to the pads of the contacts to be characterized and using two different terminals (needles) to measure the resulting (small) voltage between the contact pads. In this way, distorting effects of additional contact resistances between the measurement needles and the contact pads can be eliminated.

A method for characterizing contact resistances of contacts with nearly homogeneous current flow into vertical contacts uses contact dots of different diameters on the semiconductor, to distinguish between the specific contact resistance and the spreading resistance contributions. This method by Cox and Strack is described in [9.65].

A more versatile method which is mainly applied to lateral contacts to thin semiconductor layers with strongly inhomogeneous current flow, is the transmission line method by Berger [9.64]. Figure 9.55 shows the current distribution in this lateral contact type. The semiconductor layer is assumed with a specific resistance ρ_s ($\Omega \text{ cm}$) and its sheet resistance R_s (Ω/\square): $R_s = \rho_s/h$. For technically relevant contacts, the semiconductor sheet height h is often quite less than the contact length d . For this configuration, the following equivalent circuit can be derived (Fig. 9.56). The resistance of the epitaxial layer is described by the sum of its differential elements dR_1 .

The specific contact resistance $R_{c, \text{spec.}}$ ($= \rho_c$) is represented by the distributed vertical elements dR_2 . The total contact resistance R_c is the ratio of the voltage at the left beginning of the contact region and the total constant current I fed into the structure. According to the transmission line nature of such a structure [9.64], the specific contact resistance ρ_c may be extracted from the measurement of the total contact resistance R_c . For that purpose differential equations are formulated [9.64] which can be solved giving a relation between total and specific contact resistance in an implicit equation (9.66)

$$R_c = \frac{1}{w} \sqrt{R_s (\rho_c + 0.2 R_s h^2)} \times \coth \left(\sqrt{\frac{R_s}{\rho_c + 0.2 R_s h^2}} d \right) \quad (9.66)$$

This implicit equation allows the extraction of ρ_c after R_c has been measured and the geometrical constants w , h , and d of the test structure have been determined. The sheet resistance R_s of the epitaxial layer between two contact stripes has also to be measured before.

The measurement of R_s and R_c can be done with a setup of three contact stripes in a Kelvin contact configuration with two distances l_1 and l_2 between two contacts (Fig. 9.57).

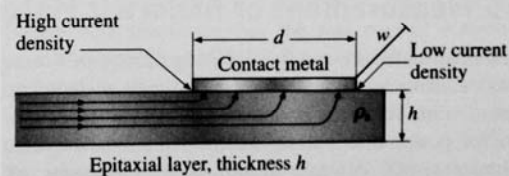


Fig. 9.55 Lateral contact of width w and of length d on a thin epitaxial layer of thickness h (after [9.64])

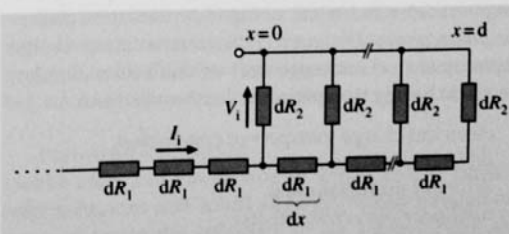


Fig. 9.56 Equivalent circuit diagram of a lateral ohmic contact according to the current distribution in Fig. 9.55 for the contact resistance of a metal on a thin semiconductor layer

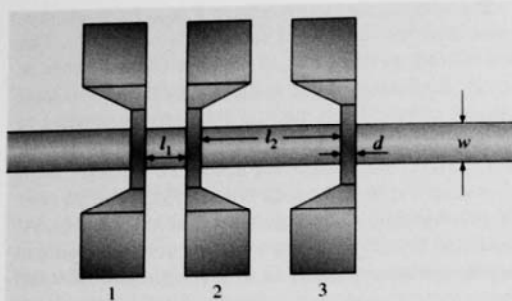


Fig. 9.57 TLM mask for the determination of the sheet resistance R_s and total contact resistance R_c from which the specific contact resistance ρ_c can be extracted (TLM: transmission line model)

Two measurements need to be taken: first, the current I (mA range) is fed through the epitaxial layer stripe of width w by using the two left-hand contacts 1, 2 with distance l_1 and measuring the voltage V_1 ; second, the two contacts 2, 3 with distance l_2 are used to measure the respective voltage V_2 by driving the same amount of current through the epitaxial layer.

From these two voltage values V_1 and V_2 together with the constant current I the sheet resistance R_s and

the total contact resistance R_c under each contact can be calculated by

$$R_s = \frac{V_1 - V_2}{I} \frac{w}{l_1 - l_2}, \quad \text{and}$$

$$R_c = \frac{1}{2} \left(\frac{V_1}{I} - l_1 \frac{R_s}{w} \right). \quad (9.67)$$

With these two terms now (9.66) can be used to extract the specific contact resistance ρ_c . The contact distances l_1 and l_2 (1–100 μm) need to be determined with high precision (submicrometer range) because otherwise larger errors would result for ρ_c , especially when ρ_c falls below $10^{-6} \Omega \text{ cm}^2$.

For electrically long contacts (e.g. $d = 40 \mu\text{m}$) the transfer length L_T is defined as $L_T = \sqrt{\rho_c / R_s}$. The transfer length illustrates the typical length for the current to pass from the epitaxial layer into the metal contact. Practical contacts do not need to be designed longer than about three transfer lengths.

The transfer resistance R_T is defined as $R_T = \sqrt{R_s \rho_c}$ ($\Omega \text{ mm}$). The transfer resistance characterizes the lowest contact resistance which can be achieved for an electrically long contact of a given width w . Transfer resistance values for e.g. FETs should be lower than $0.2 \Omega \text{ mm}$.

9.5 Measurement of Dielectric Materials Properties

Dielectric materials are the building blocks of functional electronic circuits, capacitors, gate dielectrics, transmission lines are essential as electrical insulators for power distribution. Molecular solids, organic polymer resins, ceramic glasses and composites of organic resins with ceramic fillers represent typical dielectrics. The dielectric properties of materials are used to describe electrical energy storage, dissipation and energy transfer. Electrical storage is the result of *dielectric polarization*. Dielectric polarization causes charge displacement or rearrangement of molecular dipoles. Electrical energy dissipation or *loss* results from

1. electrical charge transport or *conduction*,
2. *dielectric relaxation*,
3. *resonant transitions* and
4. *nonlinear dielectric effects*.

Energy loss is eventually related to scattering, radiation or conversion of electrical energy into thermal energy (Joule heating). Energy transfer is related to propagation of electromagnetic waves in dielectric media,

transmission lines and waveguides, where the dielectric permittivity determines the velocity of wave propagation, attenuation and ultimately the dimensions of the devices.

It is important to understand the basic characteristics of these processes because they determine the optimal approach to measurement.

Interaction of electromagnetic radiation with materials at frequencies of about 10^{12} Hz and above gives rise to quantized transitions between the electronic, vibrational and rotational molecular energy states, which can be observed by using appropriate quantum spectroscopy techniques. By contrast, the dielectric properties are governed by reorientational motions of molecular dipoles (dipolar relaxation) and motions of electrical charge carriers (electrical conduction), which leads to continuous dielectric dispersion and absorption that is observed in the frequency range of 10^{-6} – 10^{12} Hz.

The dielectric relaxation [9.66] describes the dispersion of real permittivity ϵ' and the occurrence of dielectric absorption ϵ'' . Permittivity measurements

allows for the determination of molecular dipole moments and, subsequently, can link the relaxation process with molecular dynamics and structure. The dielectric absorption (loss) spectra as a function frequency and temperature [9.67, 68], can be used to characterize molecular dynamics in dipolar liquids (polar solvents and solutes), rotator-phase crystals, nonpolar and polar polymers (polyethylene, polyacrylates, epoxy resins, polyimides). Research on dielectric relaxation in molecular liquids and solids was pioneered by Fröhlich [9.69], Hill et al. [9.70], Bottcher and Bordewijk [9.71], and for macromolecules by McCrum et al. [9.72], and Runt and Fitzgerald [9.73]. Selected developments in dielectric and related molecular processes were reviewed by Davies [9.74]. Since 1954, the most widely known and comprehensive work on dielectric materials and corresponding measurements has been that of von Hippel [9.75]. Measurement of RF properties of materials were surveyed by Bussey [9.76]. Broadband waveguiding and free-space measurement methodologies for the agriculture industry were developed by Nelson and coworkers [9.77, 78]. Extensive dielectric data were obtained recently for ferroelectric ceramics (barium titanate), inorganic and organic semiconductors and photoconductors, for ultra thin dielectrics films, which have important applications in solid-state electronic circuits and devices. Recent advances in the theory of dielectric relaxation and the corresponding experimental methodologies were reviewed by Kremer and Schönhals [9.79].

9.5.1 Dielectric Permittivity

The interaction of electromagnetic fields with matter is described by Maxwell's equations [9.80]. The polarization \mathbf{P} describes the dielectric displacement \mathbf{D} which originates from the response of the material to an external electric field \mathbf{E}

$$\mathbf{P} = \mathbf{D} - \epsilon_0 \mathbf{E} = (\epsilon_r^* \epsilon_0 - \epsilon_0) \mathbf{E}, \quad (9.68)$$

where ϵ_0 is the dielectric permittivity of free space ($\epsilon_0 = 8.854 \times 10^{-12}$ F/m), and $\epsilon^* = \epsilon_0 \epsilon_r^* = \epsilon' - i\epsilon''$ is the complex permittivity tensor, which depends on temperature, frequency, and in the case of anisotropic materials, on the direction of the electric field vector \mathbf{E} . The frequency dependence of the permittivity is illustrated in Fig. 9.58.

Relative permittivity ϵ_r^* is a dimensionless ratio of complex permittivity to the permittivity of free space $\epsilon_r^* = \epsilon^* / \epsilon_0 = \epsilon' - i\epsilon''$. The dielectric constant is the real part of the relative permittivity. The symbol used in this

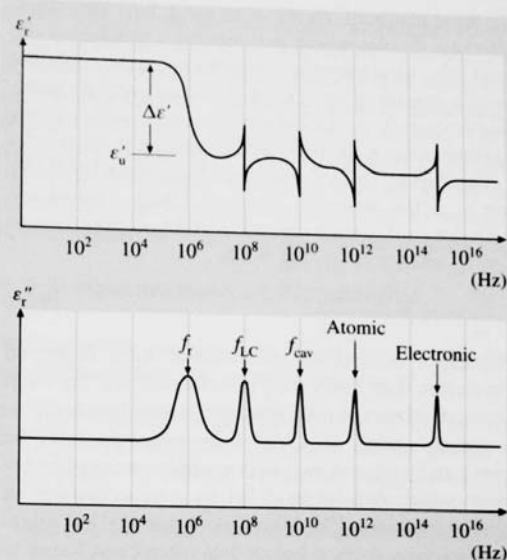


Fig. 9.58 Frequency dependence of the real ϵ'_r and imaginary ϵ''_r parts of the complex permittivity with a single relaxation process at the relaxation frequency f_r

document is ϵ'_r (other symbols such as K , k , K' , k' , ϵ_r and ϵ' are used in the technical literature). Dielectric loss tangent $\tan(\delta)$ is a dimensionless ratio of the dielectric loss ϵ''_r to the dielectric constant ϵ'_r , $\tan(\delta) = \epsilon''_r / \epsilon'_r$. Figure 9.58 illustrates that the real part of dielectric permittivity decreases by $\Delta\epsilon'_r$ at a certain frequency f_r which gives rise to a corresponding peak of the dielectric loss ϵ''_r . Such frequency dependence of the complex permittivity indicates a *dielectric relaxation*. A dielectric material may exhibit several dielectric relaxation processes, each associated with its characteristic $\Delta\epsilon'_r$, ϵ''_r and f_r depending on the molecular mechanism involved.

The dielectric relaxation should not be confused with resonant transitions between vibrational and electronic states and those that originate from a resonant behavior of the electrical measurement circuit.

Dielectric Relaxation

Unlike *electrical conduction* in which charge carriers (electrons, ions and holes) move physically through the material under the influence of an electric field, the *dielectric relaxation* originates from reorientational responses of electric dipoles to the applied electric field. Materials in which the dipoles are induced only by the application of an electric field are nonpolar mater-

ials. Polar materials, on the other hand, have permanent molecular dipoles which may exhibit a number of different relaxation processes, each having a characteristic strength measured by $\Delta\epsilon'_r$, and a characteristic relaxation frequency f_r . In the simplest case with a single relaxation time τ_r the dielectric relaxation function may be described by Debye's model [9.66], shown by (9.69). Here ϵ'_u is the dielectric constant at high frequencies, which does not contain a permanent dipole contribution ($\epsilon'_r = \epsilon'_u$ when $f \gg f_r$, Fig. 9.58)

$$\frac{\epsilon^*}{\epsilon_0} = \epsilon'_u + \frac{\Delta\epsilon_r}{1 + i\omega\tau_r} \quad (9.69)$$

Cooperative distortional polarization, local rotational polarization and interfacial polarization are the most commonly observed relaxation processes. In a composite material, many or all of these processes may be present and give rise to a very complex relaxation behavior, which can be modeled as a superposition of several relaxations. The Havriliak-Negami (HN) relaxation function, defined below, has often been found to provide a good phenomenological description of dielectric relaxation data in molecular liquids, solids and glass formers [9.81, 82]

$$\frac{\epsilon^*}{\epsilon_0} = \sum_k \left(\epsilon'_u + \frac{\Delta\epsilon_r}{[1 + (i\omega\tau_r)^\alpha]^\gamma} \right), \quad k = 1, 2, 3, \dots \quad (9.70)$$

The parameters α and γ describe the extent of symmetric (α) and asymmetric (γ) broadening of the complex dielectric function, where α and γ are ($0 < \alpha \leq 1$ and $0 < \alpha\gamma \leq 1$). Equation (9.70) reduces to the well-known Debye expression when $\alpha = \gamma = 1$. While the HN equation is often referred to as an *empirical* relaxation function, recent modeling has linked the parameters α and γ to the degree of intermittency in molecular movement and long-lived spatial fluctuations in local material properties (*dynamic heterogeneity*) [9.83], which gives some insight into the meaning of the fitted parameters. In this view, the exponent α is related to the temporal intermittency of molecular displacements while γ corresponds to long-lived *dynamic heterogeneities* (or dynamic clusters). It is beyond the scope of this chapter to explain the theory of these processes and the reader is advised to consult references [9.84–87].

Regardless of the particular molecular mechanism of the dielectric relaxation, the phenomenological dependence of ϵ'_r on frequency, as shown in Fig. 9.58, can be used as a guide to select an appropriate measurement method, and then be applied to describe and analyze the dielectric properties of most dielectric materials.

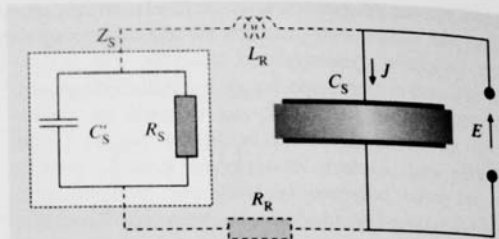


Fig. 9.59 Equivalent electrical circuit of a dielectric material

According to Fig. 9.58, the frequency spectrum can be divided into several regions, each corresponding to a characteristic dielectric response.

1. At low frequencies, well below f_r , dipoles easily respond and align with the applied alternating E -field without a time lag. The dielectric loss is negligibly small and the polarization as measured by ϵ'_r can achieve the maximum value, which depends on the statistical distribution of thermally induced molecular orientations and the amplitude of the applied field. At higher fields, polarization saturation may occur, where all the dipoles are aligned. The E -field induced polarization dominates over the thermal effects, giving rise to a *nonlinear dielectric response*.
2. At frequencies close to f_r , the molecular dipoles are too slow to reorient in phase with the alternating electric field. They lag behind and their contribution to ϵ'_r is smaller than that at low frequencies. This time lag or phase difference between E and P gives rise to the dielectric loss which peaks at f_r .
3. At frequencies above f_r the particular molecular dipoles cannot follow the electric field and do not contribute to ϵ'_r and ϵ''_r , and $\epsilon'_r = \epsilon'_u$.

It is important to note that the relaxation process always leads to a decrease of ϵ'_r with increasing frequency. Dipolar relaxation can be adequately described by an electrical equivalent circuit consisting of a capacitance C_s connected in parallel with resistance R_s which is illustrated in Fig. 9.59. Both, C_s and R_s can be experimentally measured and related to the material's dielectric properties ϵ'_r and ϵ''_r .

Resonant Transitions

The rapid oscillations of ϵ'_r shown in Fig. 9.58 at frequencies above f_r indicate a resonance. Similarly to relaxation, the resonance transitions are associated with the dielectric loss peak. However, the distinguished fea-

ture of a resonance transition is a singular behavior of ϵ_r' at the resonant frequency. From the dielectric metrology viewpoint, the most important resonances are the series resonance and the cavity resonance. These transitions are typically observed in the radio-frequency range and at microwave frequencies, respectively.

Series Inductance–Capacitance Circuit Resonance

Every electrical circuit consists of interconnecting leads that introduce finite residual inductance L_R . Therefore, when measuring a capacitance C_s there will be a certain frequency $f_{LC} = 1/(2\pi\sqrt{L_R C_s})$ at which a series resonance occurs. The equivalent electrical circuit for the series resonance consists of C_s in series with L_R . The residual resistance R_R is due to finite conductivity of the interconnects (Fig. 9.59). Since at f_{LC} the energy is concentrated in the magnetic field (or current) of the inductive component L_R rather than in the electric field in C_s , these resonance conditions generally are not useful in measurement of the dielectric permittivity. The phenomenon is a common source of systematic errors in dielectric metrology unless the inductance is known or introduced purposely [9.88] to determine the capacitance from the resonant frequency. The characteristic feature of the series resonance is a rapid decrease in the measured complex impedance which reaches the value of R_R when the frequency approaches f_{LC} . The drop in the impedance is associated with an abrupt change of phase angle from $-\phi$ to ϕ . The C_s value appears very large near f_{LC} when L_R is neglected in the equivalent circuit (Fig. 9.59), and consequently, it can be incorrectly interpreted as an apparent increase in the dielectric constant (Fig. 9.58).

Dielectric Resonance

When the dimensions (l) of the dielectric specimen are comparable with the guided wavelength $\lambda_g = \lambda_0/\sqrt{\epsilon_r'}$, a superposition of the transmitted and reflected waves leads to a standing wave called cavity or dielectric resonance. At the resonant frequency, the electromagnetic energy is concentrated in the electric field inside the dielectric. Therefore the measurement techniques that are based on the dielectric resonators are the most accurate methods for determining the dielectric permittivity of low loss materials.

Infrared and Optical Transitions

Interaction of electromagnetic radiation with materials at frequencies of about 10^{12} Hz and above gives rise to quantized resonant transitions between the elec-

tronic, vibrational and rotational molecular energy states. These transitions are responsible for a singular behavior of the dielectric permittivity and the corresponding absorption, which can be observed by using appropriate quantum spectroscopy techniques. These quantum spectroscopies form a large part of modern chemistry and physics. At optical frequencies the materials dielectric properties are described by complex optical indices, $n^* = \sqrt{\epsilon^*}$, rather than permittivity.

9.5.2 Measurement of Permittivity

Techniques for complex permittivity measurement may be subdivided into two general categories [9.75].

1. The frequency range, typically below 1 GHz, over which the dielectric specimen may be treated as a circuit of lumped parameter components. Because the mathematical manipulations are relatively simple, the lumped parameter circuit approximate equations can always be used when they yield the required accuracy over sufficiently broad frequency range.
2. The high frequency range where the wavelength of the electric field is comparable to the physical dimensions of the dielectric specimen and, as a consequence, it is often referred as a distributed parameter system. Distributed parameter analysis based on the exact relations obtained from Maxwell's equations, is necessary when the effective values of circuit elements change rapidly with frequency, or when the highest accuracy is needed.

In the low frequency range, where the wave propagation effects can be neglected, the equivalent complex impedance Z_s of the relaxation circuit shown in Fig. 9.59 can be measured to determine the complex capacitance C_s and then the material's relative complex permittivity ϵ_r^* . In the following discussion complex impedance $Z_s = Z_s' - iZ_s''$ is considered to be a constant proportionality of sinusoidal voltage and current. Parameters shown in bold face indicate complex (vector) quantities.

When a capacitor is filled with a dielectric material (Sect. 9.1.6) the resulting capacitance is C_s and the dielectric permittivity is defined by (9.71)

$$\epsilon_r^*(\omega) = \epsilon_r'(\omega) - i\epsilon_r''(\omega) = \frac{C_s(\omega)}{C_0}, \quad (9.71)$$

where C_0 is the capacitance of the empty cell and ω is the angular frequency ($\omega = 2\pi f$).

If the sinusoidal electric field $E(\omega) = E_0 \exp(i\omega t)$ is applied to C_s then the dielectric permittivity can be de-

terminated by measuring the complex impedance Z_s of the circuit.

$$\frac{1}{Z_s(\omega)} = i\omega C_s, \quad (9.72)$$

$$\epsilon_r^*(\omega) = \frac{1}{i\omega Z_s C_0}, \quad (9.73)$$

Consistent with the electrical equivalent circuit of the real capacitance C_s in parallel with a resistance R_s the impedance is given by

$$\frac{1}{Z_s(\omega)} = \frac{1}{R_s} + i\omega C_s \quad (9.74)$$

and the direct expressions for ϵ_r' and ϵ_r'' are

$$\epsilon_r' = \frac{C_s}{C_0}, \quad (9.75)$$

$$\epsilon_r'' = \frac{1}{\omega R_s C_0}. \quad (9.76)$$

The capacitance of the empty cell C_0 (cell constant) is typically determined from the specimen geometry or measurements of standard materials with known dielectric permittivity. Commercially available dielectric test fixtures have the cell constant and error correction formulas provided by their manufacturers [9.89, 90].

Impedance Measurement

Using a Four-Terminal Method

In the frequency range of up to about 10^8 Hz, a four terminal (4T) impedance analyzer can be employed to measure complex impedance of the capacitance C_s and then the permittivity can be calculated from (9.74–9.76). The 4T methodology refers to the direct phase sensitive measurement of the sample's current and voltage. Systems combining Fourier correlation analysis with dielectric converters and impedance analysis have recently become commercially available [9.79]. The

recently developed dielectric instrumentation incorporates into one device a digital synthesizer-generator, sine wave correlators and phase sensitive detectors, capable of automatic impedance measurements from 10^{-2} to $10^{13} \Omega$. The broad impedance range also allows a wide capacitance measurement range with resolution approaching 10^{-15} F. The instrumentation should be calibrated against appropriate impedance standards using methods and procedures recommended by their manufacturers.

The dielectric samples typically utilize a parallel-plate or cylindrical capacitor geometry [9.75, 91] having capacitances of about 10 pF to several hundred pF. The standard measurement procedures [9.91] recommend a three-terminal (3T) cell configuration with a guard electrode (G), which minimizes the effect of the fringing and stray electric fields on the measurements. The optimal method for connecting a 3T circular cell to a 4T impedance analyzer is shown in Fig. 9.60.

The *high* current on voltage terminals should be connected via coaxial cables directly to the unguarded electrode *H*, while the *low* current and voltage should be connected to the electrode that is surrounded by the guard electrode. Note that the return current loop of coaxial shields connections *S* should be short and connected to *G* at a single common point. The return current loop *S* is absolutely necessary for accurate impedance measurements, especially above 1 MHz. In a two terminal configuration (2T) without the guard electrode, the connections *S* should be simply grounded together.

The dielectric constant, dielectric loss and the relaxation frequency are temperature dependent. Therefore, it is essential to measure the specimen temperature and to keep it constant (isothermal conditions) during the measurements.

Impedance Measurements

Using Coaxial Line Reflectometry

In the 4T configuration the residual inductance L_R of interconnecting cables contributes to the circuit impedance creating conditions for the series resonance at $f_{LC} \approx 1/(2\pi\sqrt{L_R C_s})$, which limits the usable frequency range. Typically, the series resonance occurs above about 30 MHz. Impedance at higher frequencies may be determined from the reflection coefficient using microwave techniques with precision transmission lines. In these techniques the reference plane can be set up right at the specimen section which largely eliminates propagation delay due to L_R . When a dielectric specimen of impedance Z_s terminates a transmission line that has a known characteristic impedance Z_0 and known wave

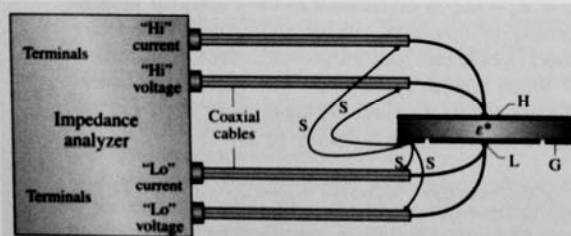


Fig. 9.60 A 3T cell to an 4T impedance analyzer. H and L are the high and low potential electrodes respectively; G is the guard electrode; S are the return current loops of coaxial shield connections

propagation characteristic, the impedance mismatch between the line and the specimen results in reflection of the incoming wave. The relation between Z_s and complex reflection coefficient Γ is given by (9.77) [9.92, 93]

$$\Gamma = \frac{Z_s - Z_0}{Z_s + Z_0} \quad (9.77)$$

It follows from (9.77) that when the line is terminated with a *short* ($Z_{\text{short}} = 0$) then $\Gamma = -1$. For an *open* termination ($Z_{\text{open}} = \infty$) $\Gamma = 1$, while in the case of a matched load, when $Z_s = Z_0$, $\Gamma = 0$, which results in no reflection. These three terminations, i.e. *short*, *load* and *open*, are used as calibration standards for setting-up the reference plane and proper measurement conditions of the reflection coefficient $|\Gamma|$ and the phase angle ϕ .

Many coaxial line configurations are available in the RF and microwave ranges, each designed for a specific purpose and application. The frequency range is limited by the excitation of the first circular waveguide propagation mode in the coaxial structure [9.92]. Decreasing the diameter of the outer and inner conductors increases the highest usable frequency. The following is a brief review of coaxial line configurations, having Z_0 of 50 Ω , most commonly used for microwave testing and measurements [9.94].

Precision APC-7 mm Configuration

The APC-7 (Amphenol Precision Connector-7 mm) utilizes air as a dielectric medium between the inner and outer conductors. It offers the lowest reflection coefficient and most repeatable measurement from DC to 18 GHz, and is the preferred configuration for the most demanding applications, notably metrology and calibration. The diameter of the inner conductor $d = 3.02$ mm and the diameter of the outer conductor $D = 7.00$ mm (Fig. 9.61) determines the characteristic impedance value of 50 Ω [9.92].

Precision APC-3.5 mm Configuration

The 3.5 mm configuration also utilizes air as a dielectric medium between the inner and outer conductors. It is mode free up to 34 GHz.

Precision-2.4 mm Configuration

The 2.4 mm coaxial configuration was developed by Hewlett Packard and Amphenol for use up to 50 GHz. It can mate with the APC 3.5 mm connector through appropriate adapters. The 2.4 mm coaxial line is offered in three quality grades: general purpose, instrument, and metrology. The general purpose grade is intended for economy use on components and cables. Instrument

grade is best suited for measurement applications where repeatability and long life are primary considerations. Metrology grade is best suited for calibration applications where the highest performance and repeatability are required.

1.85 mm Coaxial Configuration

The 1.85 mm configuration was developed in the mid-1980s by Hewlett Packard, now Agilent Technologies, for mode-free performance to about 65 GHz. HP offered their design to the public domain in 1988 to encourage standardization of this connector types. Nevertheless, few devices and instrumentation are available today from various manufacturers, mostly for research work. The 1.85 mm connector mates with the 2.4 mm connector.

1.0 mm Coaxial Configuration

Designed to support transmission all the way up to 110 GHz, approaching optical frequencies. This 1.0 mm coaxial configuration, including the matching adapters and connectors, is a significant achievement in precision microwave component manufacturing.

Coaxial Test Fixtures

There is a large family of coaxial test fixtures designed for dielectric measurements.

Open-ended coaxial test fixtures (Fig. 9.61a) are widely used for characterizing thick solid materials and liquids [9.95], and are commercially available (Agilent, Novocontrol Dielectric Probes) [9.96]. The measurements are conveniently performed by contacting one flat surface of the specimen or by immersing the probe in the liquid sample.

Short-terminated probes (Fig. 9.61b) are better suited for thin film specimens. Dielectric materials of

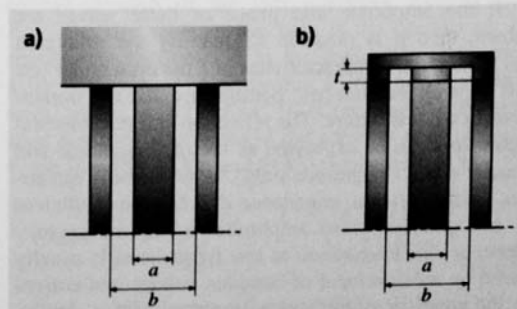


Fig. 9.61 (a) Open-ended, and (b) short terminated coaxial test fixture with a film specimen of thickness t

precisely known permittivity (air, water) are often used as a reference for correcting systematic errors in measuring $|\Gamma|$ and the phase angle ϕ , that are due to differences between the measurement and the calibration configurations. If the relaxation circuit satisfies the lumped parameters, then ϵ'_r and ϵ''_r can be obtained by combining (9.73) and (9.77) [9.97, 98]

$$\epsilon'_r = \frac{-2|\Gamma| \sin \phi}{\omega Z_0 C_0 (1 + 2\Gamma \cos \phi + |\Gamma|^2)}, \quad (9.78)$$

$$\tan \delta = \frac{\epsilon''_r}{\epsilon'_r} = \frac{1 - |\Gamma|^2}{-2|\Gamma| \sin \phi}. \quad (9.79)$$

In practice, the conventional lumped parameter formulas (9.78, 9.79) and the corresponding test procedures are accurate up to a frequency at which the impedance of the specimen decreases to about one tenth (0.1) of the characteristic impedance of the coaxial line. Since the standard characteristic impedance of coaxial configuration listed above is 50 Ω , the lowest usable impedance value of lumped-parameter circuits is about 5 Ω , hence, $f_{\max} \approx 1/(10\pi C'_s)$ [9.99]. Depending on the specimen permittivity and thickness, this upper frequency limit in the APC-7 configuration is typically below 5 GHz. At frequencies $f > f_{\max}$, wave propagation causes a spatial distribution of the electric field inside the specimen section which can no longer be treated as a lumped capacitance and has to be analyzed as a microwave network.

9.5.3 Measurement of Permittivity Using Microwave Network Analysis

Microwave network analyzer terminology describes measurements of the incident, reflected, and transmitted electromagnetic waves [9.100]. The reflected wave can be, for example, measured at the Port 1, and the transmitted wave is measured at Port 2 (Fig. 9.62).

If the amplitude and phase of these waves are known, then it is possible to quantify the reflection and transmission characteristics of a material under test (MUT) with its dielectric permittivity and the dimensions of the test fixture. The reflection and transmission parameters can be expressed as vector (magnitude and phase), scalar (magnitude only), or phase-only quantities. In this notation, impedance Z , reflection coefficient Γ and complex wave amplitudes a_i , b_i are vectors. Network characterization at low frequencies is usually based on measurement of complex voltage and current at the input or output ports (terminals) of a device. Since it is difficult to measure total current or voltage at high frequencies, complex scattering parameters, S_{11} ,

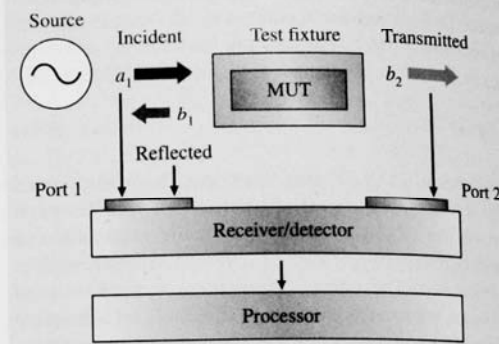


Fig. 9.62 Block diagram of a network analyzer

S_{12} , S_{21} and S_{22} are generally measured instead [9.101, 102]. Measurements relative to the incident wave allow normalization and quantification the reflection and transmission measurements to obtain values that are independent of both, absolute power and variations in source power versus frequency. The scattering parameters (S -parameters) are defined by (9.80) [9.101]

$$\begin{aligned} b_1 &= S_{11}a_1 + S_{12}a_2, \\ b_2 &= S_{21}a_1 + S_{22}a_2. \end{aligned} \quad (9.80)$$

A general signal flow graph of a two-port network with the corresponding scattering parameters is shown in Fig. 9.63a. Here a_1 and a_2 are the complex amplitudes of the waves entering the network, while b_1 and b_2 are complex amplitudes of the outgoing waves.

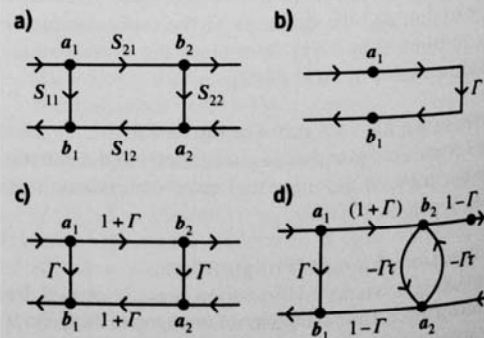


Fig. 9.63a-d Scattering parameters signal flow diagrams: (a) two-port network, (b) load termination, (c) shunt admittance, (d) transmission line partially filled with a dielectric specimen of a transmission coefficient τ

The number of S -parameters for a given device is equal to the square of the number of ports. For example, a two-Port device has four S -parameters. The numbering convention for S -parameters is that the first number following the S is the Port at which energy emerges, and the second number is the port at which energy enters. S_{21} is a measure of power emerging from Port 2 as a result of applying an RF stimulus to Port 1. Same numbers (e.g. S_{11} , S_{22}) indicate a reflection measurement. The measured S -parameters of multiple devices can be cascaded to predict the performance of more complex networks. Figure 9.63b shows a termination or load with a reflection coefficient Γ . Since there is no transmitted wave to Port 2, $b_2 = 0$, $\Gamma = b_1/a_1 = S_{11}$. Figure 9.63c is a shunt discontinuity, such as the junction of two lines or impedance mismatch, for which $S_{11} = S_{22} = \Gamma$, while $S_{12} = S_{21} = 1 + \Gamma$ [9.101]. Figure 9.63d shows the flow diagram for a transmission line, which is partially filled with a dielectric material of finite length l [9.103]. This network has a practical application in the dielectric measurements.

Network Calculations by Using Scattering Parameters and Signal-Flow Graphs

Scattering parameters are convenient in many calculations of microwave networks and they form a natural set for use with signal-flow graphs. In S -parameter signal-flow graphs, each port is represented by two nodes a_k and b_k (Fig. 9.63). Node a_k represents a complex wave entering the network at port k , while node b_k represents a complex wave leaving the network at port k . The complex scattering parameters are represented by multipliers on directed branches connecting the nodes within the network. The transfer function between any two nodes in the network can be determined by using topological flow graph rules [9.101, 104]. The Mason's nontouching-loop rule provides a method for solving a flow-graph by inspection [9.104]. The flow graph consists of branches, paths and loops. A path is a continuous succession of branches. A forward path connects an input node and an output node, where no node is encountered more than once. A first-order loop is a path that originates and terminates on the same node, and no node is encountered more than once. A second order loop is the product of three nontouching first-order loops that have no branches or nodes in common. A third order loop is the product of three nontouching first-order loops, etc. The loop value is the product of the branch multipliers around the loop. The path value is the product of all the branch multipliers along the path. The solution T of the flow-graph is the ratio of

the output variable to the input variable, and is given by

$$T = \frac{\sum_k T_k \Delta_k}{\Delta}, \quad (9.81)$$

where T_k is the path gain of k -th forward path, $\Delta = 1 - (\text{sum of all first-order loop gains}) + (\text{sum of all second-order loop gains}) - (\text{sum of all third-order loop gains})$, and $\Delta_k = 1 - (\text{sum of all first-order loop gains not touching the } k\text{-th forward path}) + (\text{sum of all second-order loop gains not touching the } k\text{-th forward path}) - \dots$

In Fig. 9.63d, the transmission line outside the specimen section has a real characteristic impedance Z_0 , while within the specimen section the network assumes a new (complex) impedance Z_s to be determined from the solution of the flow graph. The complex amplitude of the waves entering the network are a_1 and a_2 , while b_1 and b_2 are the complex amplitudes of the outgoing waves.

If the length l of the specimen were infinite then the reflection of a wave incident on the interface from the reference line, would be given simply by $S_{11} = b_1/a_1$.

In the case of a finite propagation length the amplitude of the wave transmitted depends on the complex transmission coefficient $\tau = e^{-\gamma l}$ where γ is the complex propagation constant. The signal flow in Fig. 9.63d can be solved for the scattering parameters S_{11} and S_{21} of the network by executing the rules of algebra of the flow graphs [9.101, 104]. Accordingly, from nodes a_1 to b_2 there are two first order paths with the following coefficients: $a_1 \rightarrow b_1 = \{\Gamma\}$, $\{(1 + \Gamma)e^{-\gamma l}, -\Gamma e^{-\gamma l}, (1 - \Gamma)\}$. Similarly, the path $a_1 \rightarrow b_2 = \{(1 + \Gamma)e^{-\gamma l}, (1 - \Gamma)\}$. The flow graph contains one loop: $\{-\Gamma e^{-\gamma l}, -\Gamma e^{-\gamma l}\}$ that represents the wave multiple reflection and phase change at each of the two interfaces $Z_0 - Z_s$ and $Z_s - Z_0$. The value of the path is the product of all coefficients encountered in the route. Thus, the network determinant Δ according to the graph algebra rules, equals $\Delta = 1 - \Gamma^2 e^{-2\gamma l}$. Consequently, the relative complex amplitudes of the waves at nodes b_1 and b_2 are given by (9.82) and (9.83) respectively

$$S_{11} \equiv \frac{b_1}{a_1} = \frac{a_1 \rightarrow b_1}{\Delta} = \frac{\Gamma(1 - e^{-\gamma l})(1 + e^{-\gamma l})}{1 - \Gamma^2 e^{-2\gamma l}}, \quad (9.82)$$

$$S_{21} \equiv \frac{b_2}{a_1} = \frac{a_1 \rightarrow b_2}{\Delta} = \frac{e^{-\gamma l}(1 - \Gamma)(1 + \Gamma)}{1 - \Gamma^2 e^{-2\gamma l}}, \quad (9.83)$$

where, S_{11} and S_{21} are the measured complex scattering parameters, γ is the complex propagation constant ($\gamma = \alpha + j\beta$), l is the propagation length, and Γ is the complex reflection coefficient [9.92, 93]. From (9.83) one can find

$$e^{-\gamma l} = \left[\frac{1 - (S_{11}/\Gamma)}{1 - S_{11}\Gamma} \right]^{1/2} \quad (9.84a)$$

and then substituting (9.84a) to (9.82) yields $1/2\Gamma - 1/2\Gamma b + 1/2 = 0$, from which

$$\Gamma = b \pm \sqrt{b^2 - 1}, \quad b = \frac{S_{11}^2 - S_{21}^2 + 1}{2S_{11}} \quad (9.84b)$$

and

$$Z_s = Z_0 \frac{1 + \Gamma}{1 - \Gamma} \quad (9.84c)$$

In order to determine the values of the complex γ , and Z_s , from (9.84), the measured complex S_{11} and S_{21} parameters should be returned by the network analyzer in complex coordinates form i.e. $S_{ij} = (\text{Re}S_{ij}, \text{Im}S_{ij})$. If polar notation is used then the phase angle needs to be converted to the true value of the measured phase (β) in radians rather than the cyclically mapped phase angle $\pm 180^\circ$. Results that indicate no physical meaning such as negative attenuation constant (α) need to be corrected by selecting an appropriate solution of (9.84a) and (9.84b). Equation (9.84) are general and applicable to network configurations consisting of a transmission line with impedance discontinuity Z_0 - Z_s - Z_0 , which is inserted between two reference transmission lines of the characteristic impedance Z_0 . Once γ and Z_s are obtained then the circuit distributed parameters, the corresponding materials electrical characteristics can be determined by using the conventional transmission line relations. The following sections describe application of (9.84) to measurements of the broadband dielectric permittivity of bulk materials and thin films.

Two-Port Transmission-Reflection Method

Figure 9.64 shows a testing configuration where the dielectric specimen of length l partially fills a precision coaxial air-line of characteristic impedance Z_0 .

The impedance in the specimen section changes from Z_0 to Z_s , and thus, this network can be represented by the flow-graph shown in Fig. 9.64. The scattering parameters S_{11} and S_{21} are measured at the reference planes A and B, and then the complex reflection coefficient Γ and the propagation constant γ are determined from (9.84). In the case of nonmagnetic media the dielectric permittivity ϵ_r^* can be obtained by simultaneously

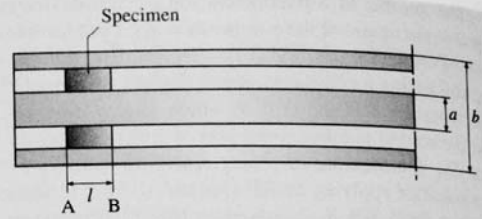


Fig. 9.64 Coaxial air-line partially filled with a dielectric slab of length l . The scattering parameters S_{11} and S_{21} are measured at the reference planes A and B, where the line assumes impedance Z_s

solving (9.85a) and (9.85b)

$$\Gamma = \frac{Z_s - Z_0}{Z_s + Z_0} = \frac{1 - \sqrt{\epsilon_r^*}}{1 + \sqrt{\epsilon_r^*}} \quad (9.85a)$$

$$\gamma = \frac{j\omega}{c\sqrt{\epsilon_r^*}} \quad (9.85b)$$

Using an APC-7 precision bead-less coaxial air line as a sample holder with $a = 3.02$ mm and $b = 7.0$ mm, the dielectric permittivity can be measured at frequencies of up to 18 GHz [9.105–107]. However, multiple wave reflections at the Z_0 - Z_s - Z_0 interfaces cause interference that may result in a singular behavior of Z_s at certain frequencies.

The dielectric specimen for the transmission-reflection method described above must be machined precisely to fit dimensions of the inner (a) and outer conductors (b) of the coaxial line (Fig. 9.64). A more detailed description of the measurement and analysis of this testing procedure can be found in [9.107, 108].

One-Port Reflection Method

An important application of network analysis to the high frequency dielectric metrology is the measurement of dielectric permittivity of thin films in a short-terminated coaxial test fixture (Fig. 9.61b).

In order to extend the measurements to the microwave range, a thin-film capacitance terminating a coaxial line is treated as a distributed network [9.109]. The wave enters the specimen from the coaxial-air line of characteristic impedance Z_0 , propagates along the diameter (a) of the specimen, and returns back to the coaxial line. The specimen represents a transmission line of impedance Z_s and propagation length l , which corresponds to the diameter of the specimen rather than to its thickness [9.109]. The wave propagation and reflection at the Z_0 - Z_s - Z_0 interfaces can be rep-

represented by the flow-graph shown in Fig. 9.63d. Here, the measured scattering parameter S_{11} is a sum of normalized incoming and outgoing waves $S_{11} = b_1/a_1 + b_2/a_1$, which are given by (9.82) and (9.83) respectively

$$S_{11} = \frac{b_1}{a_1} + \frac{b_2}{a_1} = \frac{\Gamma(1 - e^{-\gamma l})(1 + e^{-\gamma l})}{1 - \Gamma^2 e^{-2\gamma l}} + \frac{e^{-\gamma l}(1 - \Gamma)(1 + \Gamma)}{1 - \Gamma^2 e^{-2\gamma l}}, \quad (9.86)$$

which simplifies to (9.87)

$$S_{11} = \frac{\Gamma + e^{-\gamma l}}{1 + \Gamma e^{-\gamma l}}. \quad (9.87)$$

The corresponding expression for the impedance is given by (9.88) [9.110]

$$Z_s = \frac{x \cot(x)}{i\omega C_s} + i\omega L_s, \quad (9.88)$$

where, x is the wave propagation parameter $x = \omega \sqrt{\epsilon_r^*} / 2c$, C_s is the capacitance of the specimen $C_s = C_0 \epsilon_r^*$, ω is the angular frequency, l is the propagation length ($l = 2.47$ mm in the APC-7 configuration), and L_s is the residual inductance of the specimen of thickness t [9.110]

$$L_s = 1.27 \times 10^7 [\text{H/m}] \cdot t [\text{m}]. \quad (9.89)$$

The resulting expression for the relative complex permittivity ϵ_r^* is given by (9.90)

$$\epsilon_r^* = \frac{x \cot(x)}{i\omega C_0(Z_0 l + S_{11}/1 - S_{11} - i\omega L_s)}. \quad (9.90)$$

Equation (9.90) eliminates the systematic uncertainties of the lumped element approximations [9.97] and is suitable for high-frequency characterization of dielectric films of low and high permittivity values. Equations (9.88)–(9.90) have been validated numerically and experimentally up to the first cavity resonance

$$f_{\text{cav}} = \frac{c}{l \text{Re}(\sqrt{\epsilon_r^*})}, \quad (9.91)$$

where Re indicates the real part of complex square root of permittivity and $l = 2.47$ mm, which is the propagation length for the APC-7 test fixture presented in Fig. 9.61b [9.110]. For example, in the case of a specimen with a dielectric constant of 100, f_{cav} is about 12 GHz. Since the propagation term x depends on permittivity, (9.90) needs to be solved iteratively. At low frequencies, where the electrical length of the specimen

is small in comparison to the wavelength, $x \cot(x) \approx 1$, L_s can be neglected and (9.90) simplifies to the conventional (9.78) and (9.79) for a transmission line terminated with a lumped shunt capacitance. A detailed description of the measurement procedure and the calculation algorithm can be found in the reference [9.111].

Resonant Cavity Methods

Resonant measurement methods are the most accurate in determining the dielectric permittivity. In order to excite a resonance the materials must have a low dielectric loss ($\epsilon_r'' < 10^{-3}$). The measurements are usually limited to the microwave frequency range. A fairly simple and commonly used resonant method for measurement of microwave permittivity is the resonant cavity perturbation method [9.112]. Figure 9.65 illustrates a cavity test fixture which is a short section of rectangular waveguide. Conducting plates bolted or soldered to the end flanges convert the waveguide into a resonant box. A small iris hole in each end plate feeds microwave energy into and out of the cavity. Clearance holes centered in opposite walls are provided for a dielectric specimen, which is placed into region of maximum electric field. The measurement frequency is limited to few values corresponding to the fundamental mode and few higher order modes. Typically standard rectangular waveguide for the X-band [9.106] is used as a test fixture that covers the frequency range from 8 to 12 GHz. The test specimen may have the shape of a cylindrical rod, sphere or a rectangular bar [9.112].

The test fixture is connected to a network analyzer (Fig. 9.62) by using appropriate adapters and wave-

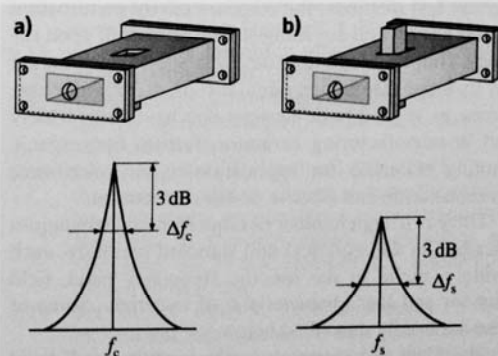


Fig. 9.65a,b Scattering parameter $|S_{21}|$ measured for (a) an empty test fixture and (b) for test fixture with a specimen inserted

uities. The resonance is indicated by a sharp increase in the magnitude of the $|S_{21}|$ parameter, with a peak value at the resonant frequency. When the dielectric specimen is inserted to the empty (air filled) cavity the resonant frequency decreases from f_c to f_s while the bandwidth Δf at half power, i.e. 3 dB below the $|S_{21}|$ peak, increases from Δf_c to Δf_s (see illustration in Fig. 9.65). A shift in resonant frequency is related to the specimen dielectric constant, while the larger bandwidth corresponds to a smaller quality factor Q , due to dielectric loss. The cavity perturbation method involves measurement of f_c , Δf_c , f_s , Δf_s , and volume of the empty cavity V_c and the specimen volume V_s .

The quality factor for the empty cavity and for the cavity filled with the specimen is given by (9.92)

$$Q_c = \frac{f_c}{\Delta f_c}, \quad Q_s = \frac{f_s}{\Delta f_s}. \quad (9.92)$$

The real and imaginary parts of the dielectric constant are given by (9.93) and (9.94), respectively

$$\epsilon'_r = \frac{V_c(f_c - f_s)}{2V_s f_s}, \quad (9.93)$$

$$\epsilon''_r = \frac{V_c}{4V_s} \left(\frac{1}{Q_s} - \frac{1}{Q_c} \right). \quad (9.94)$$

The resonant cavity perturbation method described above requires that the specimen volume be small compared to the volume of the whole cavity ($V_s < 0.1V_c$), which can lead to decreasing accuracy. Also, the specimen must be positioned symmetrically in the region of maximum electric field. However, compared to other resonant test methods, the resonant cavity perturbation method has several advantages such as overall good accuracy, simple calculations and test specimens that are easy to shape. Moreover, circular rods, rectangular bars or spheres are the basic designs that have been widely used in manufacturing ceramics, ferrites and organic insulating materials for application in the microwave communication and electric power distribution.

There is a large number of other resonant techniques described in the technical and standard literature, each having a niche in the specific frequency band, field behavior and loss characteristic of materials. Some of these are briefly described below.

Sheet low loss materials can be measured at X-band frequencies by using a split cavity resonator [9.113]. The material is placed between the two sections of the splitable resonator. When the resonant mode is ex-

cited the electric field is oriented parallel to the sample plane.

The split-post dielectric resonator technique [9.114] is also suitable for sheet materials. The system is excited in the transfer electromagnetic azimuthal mode. A useful feature of this type of resonant cavity is the ability to operate at lower frequencies without the necessity of using large specimens.

Parallel-plate resonators [9.115] with conducting surfaces allow measurements at lower frequencies since the guided wavelength λ_g inside the dielectric is smaller than in the air-filled cavities by a factor of approximately $\sqrt{\epsilon'_r}$. The full-sheet resonance technique [9.116] is commonly used to determine the permittivity of copper clad laminates for printed circuit boards.

9.5.4 Uncertainty Considerations

With increasing frequency, the complexity of the dielectric measurement increases considerably. Several uncertainty factors such as instrumentation, dimensional uncertainty of the test specimen geometry, roughness and conductivity of the conduction surfaces contribute to the combined uncertainty of the measurements. The complexity of modeling these factors is considerably higher within the frequency range of the LC resonance. Adequate analysis can be performed, however, by using the partial derivative technique [9.97, 107] and considering the instrumentation and the dimensional errors. Typically, the standard uncertainty of S_{11} can be assumed to be within the manufacturer's specification for the network analyzer, about ± 0.005 dB for the magnitude and $\pm 0.5^\circ$ for the phase. The combined relative standard uncertainty in geometrical capacitance measurements is typically smaller than 5%, where the largest contributing factor is the uncertainty in the film thickness measurements. Equation (9.90), for example, allows evaluation of systematic uncertainty due to residual inductance. It has been validated empirically for specimens 8–300 μm thick for measurements in the frequency range of 100 MHz to 12 GHz. These are reproducible with relative combined uncertainty in ϵ'_r and ϵ''_r of better than 8% for specimens having $\epsilon'_r < 80$ and thickness $t < 300 \mu\text{m}$. The resolution in the dielectric loss tangent measurements is < 0.005 . Additional limitations may arise from the systematic uncertainty of the particular instrumentation, calibration standards and the dimensional imperfections of the implemented test fixture [9.106]. Furthermore, the results of impedance measurements may not be reliable at frequencies, where $|Z|$ decreases below 0.05Ω .

9.5.5 Conclusion

In summary, one technique alone is typically not sufficient to characterize dielectric materials over the entire frequency range of interest. The lumped parameter approximate equations (9.72)–(9.76) can be utilized when they yield the required accuracy. The upper frequency limit for lumped parameter techniques is typically in the range of 100–300 MHz. Precision coaxial test fixtures can extend the applicability of the lumped parameter measurement techniques into the microwave range (9.78)–(9.79). When the effective values of circuit elements change with frequency due to wave propagation effects, it is necessary to use the distributed circuit analysis (9.84) along with the corresponding microwave network measurement methodology. The microwave broad-band one-port reflection method

(9.88)–(9.90) is most suitable for thin high dielectric constant films that are of interest to electronics, bio- and nano-technologies. For bulk anisotropic dielectrics, the microwave two-port transmission reflection method (9.85) is probably the most accurate broad-band measurement technique. The resonant cavity method (9.92)–(9.94) is best for evaluating low-loss solid dielectric materials that have the standard shapes used in manufacturing ceramics, ferrites, and organic insulating materials for application in microwave communication and electric power distribution.

In order to avoid systematic errors and obtain the most accurate results, it is important that the proper method is used for the situation at hand. Therefore measurements of dielectric substrates, films, circuit board materials, ceramics or ferrites always present a metrological challenge.

References

- 9.1 R.E. Hummel: Electrical properties of materials. In: *Understanding Materials Science*, ed. by R.E. Hummel (Springer, New York, Berlin 2004) pp.185–222, Chap. 11
- 9.2 C.H. He, Z. Lu, S. Liu, R. Liu: Cross-conductivity standard for nonferrous metals, *IEEE Trans. Instrum. Meas.* **44**, 181–183 (1995)
- 9.3 G. Rietveld, C.V. Kojmans, L.C.A. Henderson, M.J. Hall, S. Harmon, P. Warnecke, B. Schumacher: DC conductivity measurements in the van der Pauw geometry, *IEEE Trans. Instrum. Meas.* **52**, 449–453 (2003)
- 9.4 L.J. van der Pauw: A method of measuring specific resistivity and Hall effect of discs of arbitrary shape, *Philips Res. Rep.* **13**, 1–9 (1958)
- 9.5 DIN IEC 468: *Method of Measurement of Resistivity of Metallic Materials* (Beuth, Berlin 1981)
- 9.6 NPL Report DEM-ES 001: Techniques and materials for the measurement of DC and AC conductivity of non-ferrous metals and alloys, *Conductivity*, May 2004, the *Conductivity* project is (has been) financially supported by an EU grant (contract No. G6RD-CT-2000-00210) under the EU Growth programme, part of the 5th Framework programme
- 9.7 M.J. Hall, L.C.A. Henderson, G. Ashcroft, S. Harmon, P. Warnecke, B. Schumacher, G. Rietveld: Discrepancies between the DC and AC measurement of low frequency electrical conductivity, *Dig. Conf. Proc. Electrom. Meas. CPEM 2004*, London (2004) pp.34–35
- 9.8 A.C. Lynch, A.E. Drake, C.H. Dix: Measurement of eddy-current conductivity, *IEE Proc. Sci. Meas. Technol.* **130**, 254–260 (1983)
- 9.9 H. Kamerlingh Onnes: The superconductivity of mercury, *Commun. Phys. Lab. Univ. Leiden* **122b**, 13–15 (1911)
- 9.10 J. Bardeen, L.N. Cooper, J.R. Schrieffer: Theory of superconductivity, *Phys. Rev.* **108**, 1175–1204 (1957)
- 9.11 J.G. Bednorz, K.A. Müller: Possible high- T_c superconductivity in the Ba-La-Cu-O system, *Z. Phys. B* **64**, 189–193 (1986)
- 9.12 M.K. Wu, J.R. Ashburn, C.J. Torng, P.H. Hor, L.R. Meng, L. Gao, Z.J. Huang, Y.Q. Wang, C.W. Chu: Superconductivity in a new mixed phase Y-Ba-Cu-O system at ambient pressure, *Phys. Rev. Lett.* **58**, 908–910 (1987)
- 9.13 C.N.R. Rao, R. Nagarajan, R. Vijayaraghavan: Synthesis of cuprate superconductors, *Supercond. Sci. Technol.* **6**, 1–22 (1993)
- 9.14 J. Clarke, A.I. Braginski: *The SQUID Handbook, Fundamentals and Technology of SQUIDs and SQUID Systems*, Vol.1 (Wiley, New York 2004)
- 9.15 B.D. Josephson: Possible new effects in superconductive tunneling, *Phys. Lett.* **1**, 251–253 (1962)
- 9.16 R. Pöpel: The Josephson effect and voltage standards, *Metrologia* **29**, 153–174 (1992)
- 9.17 W. Meissner, R. Ochsenfeld: Ein neuer Effekt bei Eintritt der Supraleitfähigkeit, *Naturwissenschaften* **21**, 787 (1933), (in German)
- 9.18 S.A. Keys, D.P. Hampshire: Characterization of the transport critical current density for conductor applications. In: *Handbook of Superconducting Materials. II: Characterization, Applications and Cryogenics*, ed. by D.A. Cardwell, D.S. Ginley (IOPP, London 2003) p.1297
- 9.19 DIN EN IEC 61788-1: *Superconductivity – Critical, Current Measurement – DC Critical Current of Cu/Nb-Ti Composite Superconductors* (Beuth, Berlin 1999)
- 9.20 P.W. Atkins: *Physikalische Chemie*, 3rd edn. (VCH, Weinheim 1990) pp. 3834–3846, (German transl.)

- 9.21 C.H. Hamann, W. Vielsich: *Elektrochemie*, 3rd edn. (VCH, Weinheim 1998), (in German)
- 9.22 J.M.G. Barthel, H. Krienke, W. Kunz: *Physical Chemistry of Electrolyte Solutions – Modern Aspects*, Top. Phys. Chem., Vol. 5 (Springer, Berlin, Heidelberg 1998)
- 9.23 J.O.M. Bockris, A.K.N. Reddy, K.N. Amiya: *Modern Electrochemistry 1, Ionics*, 2nd edn. (Springer, Berlin, Heidelberg 1989) p. 379
- 9.24 O.F. Mohammed, D. Pines, J. Dreyer, E. Pines, E.T.J. Nibbering: Sequential proton transfer through water bridges in acid–base reactions, *Science* **310**, 83–86 (2005)
- 9.25 S. Seitz, A. Manzin, H.D. Jensen, P.T. Jakobsen, P. Spitzer: Traceability of electrolytic conductivity measurements to the International System of Units in the sub mS m⁻¹ region and review of models of electrolytic conductivity cells, *Electrochim. Acta* **55**, 6323–6331 (2010)
- 9.26 F. Brinkmann, N.E. Dam, E. Deák, F. Durbiano, E. Ferrara, J. Fükö, H.D. Jensen, M. Máriássy, R.H. Shreiner, P. Spitzer, U. Sudmeier, M. Surdu: Primary methods for the measurement of electrolytic conductivity, *Accredit. Qual. Assur.* **8**, 346–353 (2003)
- 9.27 United States Pharmacopeia: USP 27–NF 22 (US Pharmacopeia, Rockville 2004)
- 9.28 ISO 7888: 1985 Water Quality: Determination of electrical conductivity (ISO, Geneva 1985)
- 9.29 Y.C. Wu, K.W. Pratt, W.F. Koch: Determination of the absolute specific conductance of primary standard KCl solutions, *J. Solut. Chem.* **18**, 515–528 (1989)
- 9.30 G. Jones, S.M. Christian: The measurement of the conductance of electrolytes. VI. Galvanic polarization by alternating current, *J. Am. Chem. Soc.* **57**, 272–284 (1935)
- 9.31 P. Spitzer, U. Sudmeier: Electrolytic conductivity – A new subject field at PTB, Report on the 146 PTB Semin. Electrolytic Conduct., PTB–ThEx–15, ed. by P. Spitzer, U. Sudmeier (Physikalisch–Technische Bundesanstalt, Braunschweig 2000) pp. 39–47
- 9.32 P. Saulnier: Absolute determination of the conductivity of electrolytes. Double differential cell with adjustable constant, *J. Solut. Chem.* **8**, 835–845 (1979)
- 9.33 P. Saulnier, J. Barthel: Determination of electrolytic conductivity of a 0.01 M aqueous potassium chloride solution at various temperatures by an absolute method, *J. Solut. Chem.* **8**, 847–851 (1979)
- 9.34 F. Löffler: Design and production of the electric conductivity cell, Report on the 146 PTB Semin. Electrolytic Conduct., PTB–ThEx–15, ed. by P. Spitzer, U. Sudmeier (Physikalisch–Technische Bundesanstalt, Braunschweig 2000) pp. 49–64
- 9.35 Y.C. Wu, W.F. Koch, D. Feng, L.A. Holland, A.E. Juhász, A. Tomek: A DC method for the absolute determination of conductivities of the primary standard KCl solutions from 0 °C to 50 °C, *J. Res. Natl. Inst. Stand. Technol.* **99**, 241–246 (1994)
- 9.36 D.F. Evans, M.A. Matesich: The measurement and interpretation of electrolytic conductance. In: *Techniques of Electrochemistry*, Vol. 2, ed. by E. Yeager, A.J. Salkind (Wiley, New York 1973)
- 9.37 T.S. Light: Temperature dependence and measurement of resistivity of pure water, *Anal. Chem.* **56**, 1138–1142 (1994)
- 9.38 F. Oehme: *Chemische Sensoren. Funktion, Bauformen, Anwendungen* (Vieweg, Braunschweig 1991), p. 39
- 9.39 European Pharmacopeia: *Conductivity* (European Pharmacopeia, Strasbourg 2004), EP 4, 2.2.38, <http://www.pheur.org/>
- 9.40 W.L. Marshall: Electrical conductance of liquid and supercritical water evaluated from 0 °C and 0.1 MPa to high temperatures and pressures. Reduced-state relationships, *J. Chem. Eng. Data* **32**, 221–226 (1987)
- 9.41 R.D. Thornton, T.S. Light: A new approach to accurate resistivity measurement of high purity water, *Ultrapure Water* **7**, 14–21 (1989)
- 9.42 P. Spitzer, B. Rossi, Y. Gignet, S. Mabic, U. Sudmeier: New approach to calibrating conductivity meters in the low conductivity range, *Accredit. Qual. Assur.* **10**, 78–81 (2005)
- 9.43 H.D. Jensen, J. Sørensen: Electrolytic conductivity at DFM – results and experiences, Report on the 146 PTB Semin. Electrolytic Conduct., PTB–ThEx–15, ed. by P. Spitzer, U. Sudmeier (Physikalisch–Technische Bundesanstalt, Braunschweig 2000) pp. 153–213
- 9.44 D.C. Look: *Electrical Characterization of GaAs Materials and Devices* (Wiley, Chichester 1989)
- 9.45 P. Blood, J.W. Orton: *The Electrical Characterization of Semiconductors: Majority Carriers and Electron States* (Academic, New York 1992)
- 9.46 E.B. Hansen: On the influence of shape and variations in conductivity of the sample on four-point measurements, *Appl. Sci. Res. B* **8**, 93–104 (1960)
- 9.47 R.L. Petritz: Theory of an experiment for measuring the mobility and density of carriers in the space-charge region of a semiconductor surface, *Phys. Rev.* **110**, 1254–1262 (1958)
- 9.48 L.J. van der Pauw: A method of measuring specific resistivity and Hall effect of discs of arbitrary shape, *Philips Res. Rep.* **13**, 1–9 (1958)
- 9.49 S.M. Sze: *Physics of Semiconductor Devices* (Wiley, Chichester 1981)
- 9.50 K. Ziegler, E. Klausmann, S. Kar: Determination of the semiconductor doping profile right up to its surface using the MIS capacitor, *Solid-State Electron.* **18**, 189–198 (1975)
- 9.51 D.P. Kennedy, P.C. Murley, W. Kleinfelder: On the measurement of impurity distributions in silicon by the differential capacitance technique, *IBM J. Res. Dev. Sept.*, 399–409 (1968)

- 9.52 D.P. Kennedy, R.P. O'Brian: On the measurement of impurity atom distributions by the differential capacitance technique, IBM J. Res. Dev. **March**, 212–214 (1969)
- 9.53 W.C. Johnson, P.T. Panousis: The influence of Debye length on the C–V-measurement of doping profiles, IEEE Trans. Electron Devices **18**, 956–973 (1971)
- 9.54 W.A. Harrison: *Electronic Structure and the Properties of Solids: The Physics of the Chemical Bond* (Dover, New York 1989)
- 9.55 S.R. Forest, R.F. Leheny, R.E. Nahory, M.A. Pollack: $\text{In}_{0.53}\text{Ga}_{0.47}\text{As}$ photodiodes with dark current limited by generation-recombination and tunneling, Appl. Phys. Lett. **37**(3), 322–325 (1980)
- 9.56 A. Goetzberger, B. McDonald, R.H. Haitz, R.M. Scarlett: Avalanche effects in silicon p–n junction. II. Structurally perfect junctions, J. Appl. Phys. **34**, 1591–1601 (1963)
- 9.57 G.L. Miller, D.V. Lang, L.C. Kimerling: Capacitance transient spectroscopy, Annu. Rev. Mater. Sci. **7**, 377–448 (1977)
- 9.58 D.V. Lang: Deep-level transient spectroscopy, J. Appl. Phys. **45**(7), 3023–3032 (1974)
- 9.59 R.N. Hall: Electron-hole recombination in germanium, Phys. Rev. **87**, 387 (1952)
- 9.60 W. Shockley, W.T. Read: Statistics of the recombinations of holes and electrons, Phys. Rev. **87**, 835–842 (1952)
- 9.61 D.L. Partin, J.W. Chen, A.G. Milnes, L.F. Vassamillet: J. Appl. Phys. **50**(11), 6845 (1979)
- 9.62 E.H. Rhoderick: *Metal-Semiconductor Contacts* (Clarendon, Oxford 1980)
- 9.63 A. Piotrowska, A. Guivarc'h, G. Pelous: Ohmic contacts to III–V compound semiconductors: A review of fabrication techniques, Solid-State Electron. **26**(3), 179–197 (1983)
- 9.64 H.H. Berger: Models for contacts to planar devices, Solid-State Electron. **15**, 145–158 (1972)
- 9.65 R.H. Cox, H. Strack: Ohmic contacts for GaAs devices, Solid-State Electron. **10**, 1213–1218 (1967)
- 9.66 P.W. Debye: *Polar Molecules* (Chemical Catalog, New York 1927)
- 9.67 C.P. Smyth: *Dielectric Behavior and Structure* (McGraw Hill, New York 1955)
- 9.68 K.S. Cole, R.H. Cole: Absorption in dielectrics dispersion, J. Chem. Phys. **9**, 341 (1941)
- 9.69 H. Fröhlich: *Theory of Dielectrics* (Oxford Univ. Press, Oxford 1949)
- 9.70 N. Hill, W.E. Vaughan, A.H. Price, M.M. Davies: *Dielectric Properties and Molecular Behavior* (Van Nostrand Reinhold, New York 1969)
- 9.71 C.J.F. Bottcher, P. Bordewijk: *Theory of Electric Polarization* (Elsevier, New York 1996)
- 9.72 N.G. McCrum, B.E. Read, G. Williams: *Anelastic and Dielectric Effects in Polymeric Solids* (Wiley, New York 1967)
- 9.73 J.P. Runt, J.J. Fitzgerald: *Dielectric Spectroscopy of Polymeric Materials* (Am. Chem. Soc., Washington 1997)
- 9.74 D.W. Davies: *The Theory of the Electric and Magnetic Properties of Molecules* (Wiley, New York 1969)
- 9.75 A.R. von Hippel (Ed.): *Dielectric Materials Applications* (Wiley, New York 1954)
- 9.76 H.E. Bussey: Measurement of RF properties of materials, A survey, Proc. IEEE **55**(5), 1046–1053 (1967)
- 9.77 S.O. Nelson: Dielectric properties of agricultural products, IEEE Trans. Electr. Insul. **26**, 845–869 (1991)
- 9.78 A.W. Kraszewski, S. Trabelsi, S.O. Nelson: Broadband microwave wheat permittivity measurements in free space, J. Microw. Power Electromag. Energy **37**, 41–54 (2002)
- 9.79 F. Kremer, A. Schönhals: *Broadband Dielectric Spectroscopy* (Springer, Berlin, Heidelberg 2003)
- 9.80 J.C. Maxwell: *An Elementary Treatise on Electricity*, 2nd edn. (Clarendon, Oxford 1888)
- 9.81 S. Havriliak, S.J. Negami: A complex plane analysis of α -dispersions in some polymer systems, J. Polym. Sci. C Polym. Symp. **14**, 99 (1966)
- 9.82 D.W. Davidson, R.H. Cole: Dielectric relaxation in glycerine, J. Chem. Phys. **18**, 1417–1418 (1950)
- 9.83 V.V. Novikov, V.P. Privalko: Temporal fractal model for the anomalous dielectric relaxation of inhomogeneous media with chaotic structure, Phys. Rev. E **64**, 031504 (2001)
- 9.84 V.V. Daniel: *Dielectric Relaxation* (Academic, London 1967)
- 9.85 A.K. Jonsher: *Dielectric Relaxation in Solids* (Chelsea Dielectrics, London 1983)
- 9.86 F. Alvarez, A. Alegria, J. Colmenero: A new method for obtaining distribution of relaxation times from frequency relaxation spectra, J. Chem. Phys. **103**, 798–806 (1995)
- 9.87 H. Schäfer, E. Sternin, R. Stannarius, M. Arndt, F. Kremer: Novel approach to the analysis of broadband dielectric spectra, Phys. Rev. Lett. **76**, 2177–2180 (1996)
- 9.88 L. Hartshorn, W.H. Ward: The measurement of the permittivity and power factor of dielectrics from 10^4 to 10^8 cycles per second, J. Inst. Electr. Eng. **79**, 567–609 (1936)
- 9.89 Agilent Technologies: *Accessories Selection Guide For Impedance Measurements, Dielectric Test Fixtures* (Agilent Technologies, Palo Alto 2001) p. 38, <http://www.agilent.com/>
- 9.90 Application Note 1369-1: *Agilent Solutions for Measuring Permittivity and Permeability with LCR Meters and Impedance Analyzers* (Agilent Technologies, Palo Alto 2001), <http://www.agilent.com/>
- 9.91 ASTM D 150-98: *Standard Test Method for AC Loss Characteristics and Permittivity of Solid Electrical Insulating Materials* (ASTM, West Conshohocken 1998), <http://www.astm.org/>

- 9.92 D.A. Gray: *Handbook of Coaxial Microwave Measurements* (General Radio, West Concord 1968)
- 9.93 S. Ramo, J.R. Whinnery, T. Van Duzer: *Fields and Waves in Communication Electronics* (Wiley, New York 1994)
- 9.94 Agilent Technologies: *RF and Microwave Test Accessories* (Agilent Technologies, Palo Alto 2006), <http://www.agilent.com/>
- 9.95 J.P. Grant, R.N. Clarke, G.T. Symm, N. Spyrou: A critical study of the open-ended coaxial line sensor technique for RF and microwave complex permittivity measurements, *J. Phys. E Sci. Instrum.* **22**, 757–770 (1989)
- 9.96 Agilent Technologies: *85070C Dielectric Probe Kit* (Agilent Technologies, Palo Alto 2005), <http://www.agilent.com/>
- 9.97 S.S. Stuchly, M.A. Rzepecka, M.F. Iskander: Permittivity measurements at microwave frequencies using lumped elements, *IEEE Trans. Instrum. Meas.* **23**, 5662 (1974)
- 9.98 M.A. Stuchly, S.S. Stuchly: Coaxial line reflection methods for measuring dielectric properties of bio-logical substances at radio and microwave frequencies: A review, *IEEE Trans. Instrum. Meas.* **29**, 176183 (1980)
- 9.99 M.F. Iskander, S.S. Stuchly: Fringing field effect in the lumped-capacitance method for permittivity measurements, *IEEE Trans. Instrum. Meas.* **27**, 107109 (1978)
- 9.100 R.J. Collier, A.D. Skinner (Eds.): *Microwave Measurements* (The Institution of Engineering Technology, Stevenage 2007)
- 9.101 J.K. Hutton: Analysis of microwave techniques by means of signal flow graphs, *IRE Trans. Microw. Theory Tech.* **8**, 206212 (1960)
- 9.102 K. Kurokawa: Power waves and the scattering matrix, *IEEE Trans. Microw. Theory Tech.* **13**, 194202 (1965)
- 9.103 A.M. Nicolson: Broad-band microwave transmission characteristics from a single measurement of the transient response, *IEEE Trans. Instrum. Meas.* **19**, 337382 (1970)
- 9.104 J. Mason: Feedback theory, *Proc. IRE* **44**, 920–926 (1956)
- 9.105 S.S. Stuchly, M. Matuszewski: A combined total reflection-transmission method in application to dielectric spectroscopy, *IEEE Trans. Instrum. Meas.* **27**, 285288 (1978)
- 9.106 Product Note 8510-3: *Measuring the Dielectric Constant of Solids with the HP Network Analyzer* (Hewlett Packard, Palo Alto 1985)
- 9.107 J. Baker-Jarvis, E.J. Vanzura, W.A. Kissick: Improved technique for determining complex permittivity with the transmission/reflection method, *IEEE Trans. Instrum. Meas.* **38**, 10961103 (1990)
- 9.108 J. Baker-Jarvis, R.G. Geyer, P.D. Domich: A nonlinear least-squares with causality constraints applied to transmission line permittivity, *IEEE Trans. Instrum. Meas.* **41**, 646652 (1992)
- 9.109 J. Obrzut, N. Noda, R. Nozaki: Broadband characterization of high dielectric constant films for power – Ground decoupling, *IEEE Trans. Instrum. Meas.* **51**, 829–832 (2002)
- 9.110 J. Obrzut, A. Anopchenko: Input impedance of a coaxial line terminated with a complex gap capacitance numerical experimental analysis, *IEEE Trans. Instrum. Meas.* **53**, 11971202 (2004)
- 9.111 IPC: Standard test methods, IPC TM-650, Method 2.5.5.10: High frequency testing to determine permittivity and loss tangent of embedded passive materials (IPC, Bannockburn 2005) http://www.ipc.org/4.0_Knowledge/4.1_Standards/test/2-5-5-10.pdf
- 9.112 ASTM D2520-01: *Standard Test Methods for Complex Permittivity (Dielectric Constant) of Solid Electrical Insulating Materials at Microwave Frequencies and Temperatures to 1650 °C, Test Method B – Resonant Cavity Perturbation Method* (ASTM, West Conshohocken 1998), <http://www.astm.org/>
- 9.113 G. Kent: Nondestructive permittivity measurements of substrates, *IEEE Trans. Instrum. Meas.* **45**, 102106 (1996)
- 9.114 S. Maj, M. Pospieszalski: A composite multilayered cylindrical dielectric resonator, *Microwave Symposium Digest, 1984 IEEE MTT-S Int.* (IEEE, San Francisco 1984) pp. 190–191
- 9.115 J. Krupka, K. Derzakowski, A. Abramowicz, M.E. Tobar, R.G. Geyer: Use of whispering-gallery modes for complex permittivity determinations of ultra-low-loss dielectric materials, *IEEE Trans. Microw. Theory Tech.* **47**, 752759 (1999)
- 9.116 G.I. Woolaver: Accurately measure dielectric constant of soft substrates, *Microwave RF* **24**, 153158 (1990)